



Asymmetric Quantum Devices and Heat Transport

Miguel Ángel Simón Martínez

Supervisors:

Prof. Juan Gonzalo Muga Francisco

Prof. María Luisa Pons Barba

Departamento de Química-Física
Facultad de Ciencia y Tecnología
Universidad del País Vasco/Euskal Herriko Unibertsitatea
(UPV/EHU)

Leioa, Marzo 2021

Agradecimientos

Esta Tesis ha sido financiada a través de una beca predoctoral concedida por el Gobierno Vasco/Eusko Jaurlaritza

Contents

List of Figures	ix
List of publications	xvii
Introduction	3
I Non-Hermitian systems and asymmetric scattering	9
1 Asymmetric scattering by non-Hermitian potentials	11
1.1 Non-Hermitian scattering in 1 dimension	13
1.1.1 Why is non-Hermiticity needed for asymmetric scattering?	17
1.2 Right and left eigenvectors of non-Hermitian Hamiltonians	18
1.3 Generalized symmetries	19
1.3.1 Equivalences between symmetries	24
1.4 Asymmetric devices	25
1.5 Designing potentials for asymmetric devices	28
1.6 Extending the scattering asymmetry to a broad incident-momentum domain	31
1.7 Discussion	32
2 S-matrix pole symmetries for non-Hermitian scattering Hamiltonians	35
2.1 Superoperator formalism	38
2.2 S-matrix pole structure	39
2.3 Separable Potentials	42
2.3.1 Time-reversal symmetric potential	43
2.3.2 Parity pseudohermitian potential	46
2.4 Discussion	49
3 Quantum-Optical implementation of non-Hermitian potentials for asymmetric scattering	51
3.1 Effective non-local potential for the ground state of a two-level atom	52
3.1.1 Possible symmetries of the non-local potential	53
3.2 Design of asymmetric devices	54

3.3	Classical approximation for \mathcal{T}/\mathcal{A} device	57
3.4	Discussion	60
II	Heat rectification in mesoscopic systems	63
4	Local Rectification of Heat Flux	65
4.1	Homogeneous one-dimensional chain	65
4.2	Impurity-based thermal rectifier	70
4.3	Discussion	72
5	Asymmetric heat transport in ion crystals	75
5.1	Physical System	76
5.2	Calculation of the stationary heat currents	78
5.2.1	Algebraic, small-oscillations approach to calculate the steady state	81
5.3	Numerical Results	84
5.3.1	Evolution to steady state	84
5.3.2	Rectification in frequency graded chains	86
5.3.3	Same bath temperatures, different bath couplings	88
5.3.4	Dependence with number of ions	89
5.3.5	Graded versus segmented	89
5.4	Discussion	89
6	Thermal rectification with a minimal model of two harmonic oscillators	93
6.1	Physical Model	94
6.2	Covariance matrix in the steady state	97
6.3	Solutions	98
6.4	Relation of the Model to a trapped ion setup	100
6.4.1	Collective trap	100
6.4.2	Individual on-site traps	101
6.4.3	Optical molasses and Langevin baths	102
6.5	Looking for rectification	103
6.5.1	Parametric exploration	104
6.5.2	Spectral match/mismatch approach to rectification	108
6.6	Discussion	111
Conclusions		115
Appendices		121
A	Properties of separable potentials	121
A.1	Transition operator	121

A.2	<i>S</i> -matrix eigenvalues	121
B	Numerical calculation of transmission and reflection coefficients	123
B.1	Free motion, $\mathcal{V} = 0$	124
B.2	General case	125
B.3	Asymptotic form of the solutions	126
B.4	Differential equations for R and T matrices	127
B.5	Improving numerical efficiency	128
B.6	Bounds from unitarity	129
C	Full set of steady-state equations for the components of $\mathbb{C}^{s.s}$	131
D	Complete expressions for the Spectral Density Matrix	133
	Bibliography	137

List of Figures

1.1	Devices with asymmetric scattering (limited to scattering coefficients being 0 or 1). The dashed and continuous lines represent respectively zero or one for the moduli of the scattering amplitudes; the bended lines are for reflection amplitudes, and the straight lines for transmission: (a) One-way mirror ($\mathcal{T}\mathcal{R}/\mathcal{A}$); (b) One-way barrier (\mathcal{T}/\mathcal{R}); (c) One-Way T-filter (\mathcal{T}/\mathcal{A}); (d) Mirror & 1-way transmitter ($\mathcal{T}\mathcal{R}/\mathcal{R}$); (e) One-way R-filter (\mathcal{R}/\mathcal{A}); (f) Transparent, one-way reflector ($\mathcal{T}\mathcal{R}/\mathcal{T}$). The nomenclature for the devices is explained in the main text of section 1.4.	12
1.2	(Color online) One-way T-filter (\mathcal{T}/\mathcal{A} , $ T^l = 1, T^r = R^l = R^r = 0$) with potential $V(x, y) = V(x, y) e^{i\phi(x, y)}$ set for $k_0 = 1/d$. (a) Absolute value $ V(x, y) $; (b) Argument $\phi(x, y)$; (c) Transmission and reflection coefficients: $ R^l ^2$ (black, solid line), $ T^l ^2$ (green, solid line), $ R^r ^2$ (blue, tick, dashed line), $ T^r ^2$ (red, dotted line). $V_0 = \hbar^2/(2md^3)$	29
1.3	(Color online) Transparent 1-way reflector with a local PT potential: (a) Approximation of the potential (1.37), real part (green solid line), imaginary part (blue dashed line). (b,c) Transmission and reflection coefficients versus momentum kd ; left incidence: $ R^l ^2$ (black, solid line), $ T^l ^2$ (green, solid line); right incidence: $ R^r ^2$ (blue, tick, dashed line), $ T^r ^2$ (red, dotted line, coincides with green, solid line). $\epsilon/d = 10^{-4}$. (b) $\alpha = 1.0\hbar^2/(4\pi m)$ (c) $\alpha = 1.225\hbar^2/(4\pi m)$ (the black, solid line coincides here mostly with the red, dotted and green, solid lines).	30

2.1 Example of configuration of poles (filled circles) and zeros (empty circles) of the S -matrix eigenvalues in the complex momentum plane for Hermitian Hamiltonians. Poles in the upper half plane ($\text{Im}(p) > 0$) correspond to bound eigenstates of the Hamiltonian, i.e. localized states with negative energy. Poles in the lower half plane correspond to virtual states ($\text{Re}(p) = 0$), resonances ($\text{Re}(p) > 0$) and antiresonances ($\text{Re}(p) < 0$). The singularities with negative imaginary part correspond to states that do not belong to the Hilbert space since they are not normalizable. However, they can produce observable effects in the scattering amplitudes, in particular when they approach the real axis. The pole structure of symmetries IV, V, and VII, see Table 2.1, is similar, but pole pairs are also possible in the upper half-plane.	42
2.2 Poles and pole trajectories of time-reversal symmetric potential (2.21) for (a) varying V_0 with $a = 2b$; (b) varying a with $b = 0.5 p_0$, $V_0 > 0$; and (c) varying b with $a = p_0$, $V_0 > 0$. At pole collisions we connect each of the incoming trajectories with a different emerging trajectory but the choice of outgoing branch is arbitrary since the two colliding poles lose their identity.	44
2.3 Transmission and reflection coefficients of the time-reversal symmetric potential (symmetry V) (2.21) with $a = p_0$, $b = 0.5 p_0$ and $V_0 > 0$	46
2.4 Poles and pole trajectories for the parity pseudohermitian potential (2.25) (a) varying V_0 with $a = b$; (b) varying a with $b = p_0$, $V_0 > 0$; (c) varying b with $a = 0.5 p_0$, $V_0 > 0$	48
2.5 Transmission and reflection coefficients for $a = b = 0.5 p_0$ and $V_0 > 0$	49
3.1 Left column: \mathcal{T}/\mathcal{A} device with symmetry VIII. Top: $\Omega_{\text{VIII}}(x)$; Bottom: transmission and reflection coefficients. $v_0/v_d = 400$, $a\tau = 2618.19$, $x_0/d = 0.1532$, $\tau\Delta = 1413.01$. Middle column: \mathcal{R}/\mathcal{A} device with symmetry VI. Top: $\Omega_{\text{VI}}(x)$ (it is real); Bottom: transmission and reflection coefficients. $v_0/v_d = 400$, $b\tau = -244516.1$, $c\tau = 167853.9$, $x_0/d = 0.1679$, $\tau\Delta = 193.508$. Right column: “Partial”- \mathcal{TR}/\mathcal{A} device with symmetry I. Top: $\Omega_{\text{I}}(x)$, real (blue, solid line) and imaginary parts (orange, dashed line); Bottom: transmission and reflection coefficients. $v_0/v_d = 8$, $b\tau = 102.6520$, $c\tau = 165.8355$, $x_0/d = 0.1648$, $\tau\Delta = 90.5337$. In all cases $\tau = md^2/\hbar$ and $v_d = \hbar/(md)$	56
3.2 Non-local potentials $V(x, y)$: absolute value (top), argument (bottom). Left column: Potential for \mathcal{T}/\mathcal{A} device with symmetry VIII. Middle column: Potential for \mathcal{R}/\mathcal{A} device with symmetry VI. Right column: “Partial”- \mathcal{TR}/\mathcal{A} device with symmetry I. $V_0 = \hbar^2/(md^3)$	57
3.3 Simplified model of the asymmetric \mathcal{T}/\mathcal{A} device with symmetry VIII: (a) $\chi_+(t)$, (b) $\chi_-(t)$; ground-state population $ \chi_{\pm(t),1} ^2$ (blue, solid line), excited- $ \chi_{\pm(t),2} ^2$ (orange, dashed line). $v/v_d = 400$, $a\tau = 2618.19$, $x_0/d = 0.1532$, $\tau\Delta = 1413.01$	59

3.4	Simplified time-dependent model of the asymmetric \mathcal{T}/\mathcal{A} device with symmetry VIII: Bloch sphere explaining non time-reversal invariance, see text for details. The state trajectories are depicted in two-steps on the sphere. The rotation axes are also depicted. (a) The process simulates incidence from the left. The state starts and ends in $ 1\rangle$. (b) The process simulates incidence from the right. The state starts at $ 1\rangle$ and ends at $ 2\rangle$	60
3.5	Asymmetric \mathcal{T}/\mathcal{A} device with symmetry VIII: comparison between numerically achieved parameters (red dots) and approximated parameters (blue, solid lines) versus velocity v_0 . (a) Height of Rabi frequency a , (b) detuning Δ	61
4.1	(a) On-site potentials: harmonic potential centered at the equilibrium position of each atom (dashed blue line) as a function of the displacement from this position $x_i = y_i - y_{i0}$ in a -units, and the on-site potential for the impurity, $i = N/2 + 1$ (N even, red solid line). (b) Interaction potentials as a function of the distance between nearest neighbors: Morse potential (blue dashed line) valid for all atoms except for $i = N/2 + 1$, N even, where the modified potential (red solid line) is used. The harmonic approximation of the Morse potential is also depicted (eq. (4.5), black dots, only used for fig. 4.5, below). Parameters: $D = 0.5$, $g = 1$, $\gamma = 45$, $d = 100$ and $b = 105$, used throughout the chapter.	66
4.2	Symmetric temperature profiles for a homogeneous chain, without impurity. For $T_h = T_L$, $T_c = T_R$ (red solid dots) the (absolute value of) the heat flux is $J_{L \rightarrow R}$, equal to $J_{R \rightarrow L}$ for the reverse configuration of the bath temperatures, $T_h = T_R$, $T_c = T_L$ (black empty squares). Parameters as in fig. 4.1.	67
4.3	Temperature profile along the homogeneous chain for different number of atoms: 100 (dotted black line), 125 (dashed blue line) and 150 (solid red line). The atom sites have been rescaled with the total number of atoms. The time averages have been carried over a time interval of $\approx 2 \times 10^6$ after a transient of $\approx 1 \times 10^5$. In the inset (a), the product JN vs. N demonstrates that for long chains JN is independent of N . In (b) the linear dependence of J with ΔT for a fixed number of atoms, $N = 100$, is shown. Parameters as in fig. 4.1.	69
4.4	Temperature profile for the chain of $N = 20$ atoms, with an impurity in the $N/2+1$ position, with $T_L = T_h$ and $T_R = T_c$ (circles) and with the thermostat baths switched (squares). Parameters as in fig. 4.1. (a) $T_c = 0.15$, $T_h = 0.2$. $J_{L \rightarrow R} = 0.00769$ vs $J_{R \rightarrow L} = 0.00581$, with gives a rectification $R = 31\%$; (b) $T_c = 0.025$, $T_h = 0.325$. $J_{L \rightarrow R} = 0.0499$ vs $J_{R \rightarrow L} = 0.0140$, with $R = 256\%$	70

4.5	Rectification factor R as a function of the temperature difference between ends of the chain of atoms, ΔT . I have changed both T_h and T_c according to $T_c = 0.15 - (\Delta T - 0.05)/2$ and $T_h = 0.2 + (\Delta T - 0.05)/2$, with $N = 20$, keeping the rest of parameters as in fig. 4.1. Interatomic potentials: Morse potential, eq. (4.4) (black line with circles, see the temperature profiles of extreme points in fig. 4.4); harmonic potential, eq. (4.5) (red line with squares).	71
4.6	Temperature profile for a harmonic interacting chain of $N = 20$ atoms, with an impurity in the $N/2 + 1$ position, with $T_L = T_h$ and $T_R = T_c$ (circles) and with the thermostat baths switched (squares), for (a) $\Delta T = 0.05$ and (b) $\Delta T = 0.3$. The corresponding rectification factors are (a) $R = 18\%$ and (b) $R = 85\%$. Parameters regarding the impurity are the same as in fig. 4.1.	72
5.1	Schematic representation of the frequency-graded chain of trapped ions proposed as a thermal rectifier. The left and right ends of the chain are in contact with optical molasses at temperatures T_L and T_R (green and grey boxes respectively). Each ion is in an individual trap. The (angular) frequencies of the traps increase homogeneously from left to right, starting from ω_1 and ending at $\omega_1 + \Delta\omega$. The ions interact through the Coulomb force, which is long range, and therefore all the ions interact among them, even distant neighbors. By default I use 15 ions.	77
5.2	(a) Temperatures of the ions in the stationary state for a graded chain with the parameters described in section 5.3.1. The temperature profiles found with the algebraic method (eq. (5.19)) are indistinguishable from the ones found solving the Langevin equation (eq. (5.3)). Empty triangles (squares) correspond to $T_L = T_H$ ($T_L = T_C$) and $T_R = T_C$ ($T_R = T_H$). (b) Heat currents as a function of time for $T_L = T_H$ and $T_R = T_C$, see eq. (5.9): $J_L(t)$ (solid green line) from the left reservoir into the chain; $J_R(t)$ (dotted grey line) from the right reservoir into the chain (negative except at very short times); $J_L(t) + J_R(t)$ (dotted-dashed black line), which must go to zero in the steady state. The three lines tend to stationary values marked by horizontal lines. Parameters: $\omega_1 = 2\pi \times 50$ kHz, $a = 50 \mu\text{m}$, $\delta_H = -0.02 \Gamma$, and $\delta_C = -0.1 \Gamma$, which gives temperatures $T_H \approx 12$ mK and $T_C \approx 3$ mK. $\Delta\omega = 0.5 \omega_1$. In all figures $\Gamma = 2\pi \times 41.3$ MHz.	82
5.3	Graded chain of $N = 15$ $^{24}\text{Mg}^+$ ions. (a) Stationary fluxes for different frequency increments: J_\rightarrow (for $T_L = T_H$ and $T_R = T_C$, dashed line); J_\leftarrow (for $T_L = T_C$ and $T_R = T_H$, solid line) (b) Rectification factor. Parameters: $\omega_1 = 2\pi \times 1$ MHz, $l = 5.25 \mu\text{m}$, $a = 4.76 l$ ($25 \mu\text{m}$), $\delta_H = -0.02 \Gamma$, and $\delta_C = -0.1 \Gamma$	85

5.4	Rectification factor in a graded chain of $N = 15$ $^{24}\text{Mg}^+$ ions for different trap distances and frequency increment. The dashed lines are for $R = 0$ and delimit the regions $J_{\rightarrow} > J_{\leftarrow}$ and $J_{\rightarrow} < J_{\leftarrow}$. The parameters are $\omega_1 = 2\pi \times 1$ MHz, $l = 5.25 \mu\text{m}$, $\delta_H = -0.02 \Gamma$, and $\delta_C = -0.1 \Gamma$	86
5.5	(a) Friction coefficient defined in eq. (5.4). (b) Bath temperature defined in eq. (5.5). (c) Rectification as a function of the temperature difference between the hot and cold baths $T_H - T_C$ for δ_H below (dashed black line) and above (solid blue line) the Doppler limit, and $\delta_C = \delta_D$ (Doppler limit). Parameters: $\omega_1 = 2\pi \times 1$ MHz, $\Delta\omega = 0.15 \omega_1$, $l = 5.25 \mu\text{m}$, $a = 4.76 l$	87
5.6	Rectification factor for different bath temperature differences ΔT as the number of ions is increased. The detuning of the cold bath laser is set to the Doppler limit $\delta_C = -\Gamma/2$. $\omega_1 = 2\pi \times 1$ MHz, $\Delta\omega = 0.15 \omega_1$, $l = 5.25 \mu\text{m}$, $a = 4.76 l$	88
5.7	Comparison of graded and segmented chains with $N = 15$ $^{24}\text{Mg}^+$ ions. (a) Maximum of J_{\rightarrow} and J_{\leftarrow} for the graded and segmented chain for different frequency increments. (b) Rectification factor: graded chain (dashed lines); segmented chain (solid lines). Parameters: $\omega_1 = 2\pi \times 1$ MHz, $l = 5.25 \mu\text{m}$, $a = 4.76 l$, $\delta_H = -0.02 \Gamma$, and $\delta_C = -0.1 \Gamma$	90
6.1	Diagram of the model described in section 6.1. Two masses are coupled to each other through a spring constant k . Each mass is harmonically trapped and connected to a bath characterized by its temperature T_i and its friction coefficient γ_i	95
6.2	Rectification, R , in the $k_L k_R$ plane for $k = 1.17$ fN/m, $\gamma_L = 6.75 \times 10^{-22}$ kg/s, and $\gamma_R = 4.64 \gamma_L$, $m_1 = 24.305$ a.u., $m_2 = 40.078$ a.u. The dashed line represents eq. (6.32).	104
6.3	(a) Rectification factor, R , given by eq. (6.35) as a function of the mass and friction ratios a and g . (b) Rectification factor along the diagonal dotted line $a = g$ in (a).	107
6.4	Spectral densities of the velocities of the ions (r_3 and r_4) corresponding to $T_L = \tilde{T}_R = 2$ mK, $T_R = \tilde{T}_L = 1$ mK, and two values of c in fig. 6.3(b): (a), (b) for $c = 1$ and (c), (d) for $c = 10$. Solid, black lines are for the left ion spectral density $\mathcal{S}_1(\omega)$ and dashed, blue lines for the right ion spectral density $\mathcal{S}_2(\omega)$. Dot-dashed, vertical lines mark the frequencies of the normal modes of the system. The spectra are multiplied by their corresponding masses so that the areas are proportional to the steady-state temperatures, see eq. (6.39). (a) and (b) correspond to $R = 0$: the overlap between the phonon bands is the same in forward and reversed configurations. (c) and (d) correspond to $R \approx 0.8$: in the forward configuration (c) the phonons match better than in the reversed configuration (d).	109

6.5 The evolution of the dissipative normal modes of the system as the asymmetry parameter c increases is shown in this plot. λ_r, λ_i stand for the real and imaginary parts of the eigenvalues of the dynamical matrix \mathbb{A} .	111
---	-----

dedicatory here

List of publications

I) The results of this Thesis are based on the following articles

Published Articles

1. M. Pons, Y. Y. Cui, A. Ruschhaupt, **M. A. Simón** and J. G. Muga
Local rectification of heat flux
[EPL 119, 64001 \(2017\).](#)
2. A. Ruschhaupt, T. Dowdall, **M. A. Simón** and J. G. Muga
Asymmetric scattering by non-Hermitian potentials
[EPL 120, 20001 \(2017\).](#)
3. **M. A. Simón**, A. Buendía and J. G. Muga
Symmetries and Invariants for Non-Hermitian Hamiltonians
[Mathematics 6, 111 \(2018\).](#)
4. **M. A. Simón**, A. Buendía, A. Kiely, A. Mostafazadeh and J. G. Muga
S-matrix pole symmetries for non-Hermitian scattering Hamiltonians
[Phys. Rev. A 99, 052110 \(2019\).](#)
5. **M. A. Simón**, S. Martínez-Garaot, M. Pons and J. G. Muga
Asymmetric heat transport in ion crystals
[Phys. Rev. E 100, 032109 \(2019\).](#)
6. A. Alaña, S. Martínez-Garaot, **M. A. Simón** and J. G. Muga
Symmetries of ($N \times N$) non-Hermitian Hamiltonian matrices
[J. Phys. A: Math. Theor. 53, 135304 \(2020\).](#)

7. A. Ruschhaupt, A. Kiely, **M. A. Simón** and J. G. Muga
Quantum-optical implementation of non-Hermitian potentials for asymmetric scattering
Phys. Rev. A **102**, 053705 (2020).

8. **M. A. Simón**, A. Alaña, M. Pons, A. Ruiz-García and J. G. Muga
Heat rectification with a minimal model of two harmonic oscillators
Phys. Rev. E **103**, 012134 (2021).

II) Other articles produced during the Thesis period

Published Articles not included in this Thesis

1. M. Palmero, **M. A. Simón** and D. Poletti
Towards Generation of Cat States in Trapped Ions Set-Ups via FAQUAD Protocols and Dynamical Decoupling
Entropy **21**, 1207 (2019)

2. **M. A. Simón**, M. Palmero, S. Martínez-Garaot and J. G. Muga
Trapped-ion Fock-state preparation by potential deformation
Phys. Rev. Research **2**, 023372 (2020)

Introduction

Devices that control the flow of energy or matter play a prominent role in technology. A key device is the rectifier, which allows currents only one way. A rectifier behaves like a corridor with a trap door that can be opened from left to right but is closed otherwise. The most notable of such devices is the electric diode, which is a vital part of computers, digital devices, and AC/DC current conversion systems. Without the diode most of the technology that we have today would not exist.

The electric diode is an electrical component that allows electrical current to flow asymmetrically with respect to the sign of the potential difference that is applied to it. Typically, a diode is composed by the union of a *p*-semiconductor with an *n*-semiconductor. When a forward-bias potential ΔV is applied to the *p-n* junction (by connecting the positive pole of a battery to the *p*-semiconductor), electrical current will flow through the diode. However, the *p-n* junction acts as an electrical insulator if a reversed-bias potential $-\Delta V$ is applied.

Motivated by the technological impact of the diode, analogous devices have been developed in other physical scenarios, like optics. An optical equivalent to the diode is the optical isolator, which is used to allow one-way light propagation [1]. This device is based on the non-reciprocal rotation of the polarization direction of polarized light in materials that are in a magnetic field, known as Faraday Rotation (see ref. [2]). The optical isolator is a critical component in optical devices to protect delicate light sources from back-propagating light.

At this point we can see that a common ingredient between devices which show a diode-like behaviour is some kind of internal structural asymmetry. In the electric diode this asymmetry comes from the asymmetric distribution of charge carriers: electrons in the *n*-side, and holes in the *p*-side. In the optical isolator the orientation of the magnetic field breaks the symmetry of the system.

This Thesis is devoted to explore the physics and possible designs of devices that implement a *diodic* or rectifying mechanism for an asymmetric transport of matter or energy. The Thesis is divided into two parts: In part I, I look for asymmetric particle scattering of 1-dimensional quantum potentials and in part II, I will study thermal rectification in chains of oscillators. There follows an introduction to these two parts.

Introduction to part I: non-Hermitian systems and asymmetric scattering

The current interest to develop new quantum technologies is boosting applied and fundamental research on quantum phenomena and systems with potential applications in logic circuits, metrology, communications or sensors. Robust basic devices performing elementary operations are needed to perform complex tasks when combined in a circuit. With the development of new quantum technologies in mind, the objective of this part is to design 1-dimensional scattering potentials for a quantum, spinless particle of mass m that lead to transmission and reflection coefficients (squared modulus of the amplitudes) which differ for wave packets coming from the left or the right.

To find an asymmetric scattering behavior, I will use non-Hermitian and non-local potentials [3, 4]. Although non-local and non-Hermitian potentials might seem uncommon and extraordinary in quantum physics to some, they appear naturally when applying partitioning techniques to describe the effective interactions in a subspace of a larger system with a Hermitian Hamiltonian by projection [3, 5, 6]. Non-Hermitian Hamiltonians representing effective interactions have a long history in nuclear, atomic, and molecular physics, and have become common in optics, where wave equations in waveguides could simulate the Schrödinger equation [7–9]. Non-Hermitian Hamiltonians can also be set phenomenologically, e.g. to describe dissipation [7]. Recently there has been a lot of interest in non-Hermitian Hamiltonians [10–18], in particular, the ones having parity-time (PT) symmetry [19, 20] because of their spectral properties and useful applications, mostly in optics [8, 9, 21]. However, I shall emphasize that symmetries different from PT exist and are necessary to produce certain forms of asymmetric scattering.

The contents of this part of the Thesis will be organized as follows. In chapter 1, I will use non-Hermitian and non-local potentials to design potentials with asymmetric scattering coefficients for left/right incidence. Symmetries for non-Hermitian Hamiltonians will be generalized using the concept of pseudohermiticity [22] and used to derive useful selection rules for the transmission and reflection coefficients. In chapter 2, I will derive a set of properties of the eigenvalues of scattering potentials that extend previous results for discrete non-Hermitian Hamiltonians by using the generalized symmetries. In chapter 3, I will present a

possible physical realization for asymmetric scattering Hamiltonians in a quantum optics setup.

Introduction to part II: Heat rectification in mesoscopic systems

Radiation, heat and electricity are prominent mechanisms of energy transport. In particular, the two last mechanisms play a dominant role in technology. Modern information processing rests on electronic devices like the diode and the transistor. However, there is not an analogous technology to control heat currents driven by phonons. An explanation could be that phonons are more difficult to control than electrons since (contrary to them) they do not have mass or electrical charge [23]. However, it would be interesting to explore the design of *phononic* devices due to the richness of different physical mechanisms that mediate heat transport. The thermal rectifier, or thermal diode, would be a primary building block to develop *phononics* [23]. In this part I study thermal rectification in chains of oscillators with the design of a thermal diode in mind.

Thermal rectification is the physical phenomenon, analogous to electrical current rectification in diodes, in which heat current through a device or medium (the thermal diode or rectifier) is not symmetric with respect to the exchange of the bath temperatures at the boundaries. It was first observed in 1936 by Starr in a junction between copper and cuprous oxide [24]. The theoretical work started much later using as rectifiers simple anharmonic chain models with different segments [25, 26]. These papers sparked much research that continues to this day. Research on thermal rectification has gained a lot of attention in recent years as a key ingredient to build prospective devices to control heat flows similarly to electrical currents [23, 27]. There are proposals to engineer thermal logic circuits [28] in which information, stored in thermal memories [29], would be processed in thermal gates [30]. Such thermal gates, as their electronic counterparts, would require thermal diodes and thermal transistors to operate [31, 32]. Heat rectifying devices would also be quite useful in nanoelectronic circuits, letting delicate components dissipate heat while being protected from external heat sources [27].

Most work on thermal diodes has been theoretical with only a few experiments (see refs. [33–36]). A relevant attempt to build a thermal rectifier was based on a

graded structure made of carbon and boron nitride nanotubes that transports heat between a pair of heating/sensing circuits [33]. One of the ends of the nanotube is covered with a deposition of another material, which makes the heat flow better from the covered end to the uncovered end. However, rectifications were small, with rectification factors around 7%.

Much of the theoretical effort in thermal rectification research has been aimed at improving the rectification factors and the features of the rectifiers. The first approach to designing thermal diodes consisted in using chains of oscillators segmented into two or more regions with different properties [25, 26, 37, 38], which is reminiscent of the idea of the *p-n* junction in electric diodes. However, it was soon noticed that the performance of segmented rectifiers was very sensitive to the size of the device, *i.e.*, rectification decreases when increasing the length of the rectifier [38]. To overcome this limitation two ideas were proposed. The first one consisted in using graded rather than segmented chains, *i.e.*, chains where some physical property varies continuously along the site position such as the mass of particles in the chain [39–47]. The second one consisted in using chains with long-range interactions (LRI), such that all the elements in the chain interact with all the rest [40, 48, 49]. The rationale behind these proposals was that in a graded system, new asymmetric rectifying channels are created, while the long-range interactions create also new transport channels, avoiding the usual decay of heat flow with size [40]. Besides a stronger rectification power, LRI graded chains are expected to have better heat conductivity than segmented ones. This is an important point for technological applications, because devices with high rectification factors are not useful if the currents that flow through them are very small.

Another main focus of the theoretical research in thermal rectification is the search for the fundamental factors that contribute to the emergence of rectification. Historically, the crucial elements for having rectification have been the presence of some structural asymmetry in the system and of non-linear (anharmonic) forces [23, 37, 38, 50–54], which lead to a temperature dependence of the phonon bands or power spectral densities. A match or mismatch of the phonon bands of neighboring parts of the chain implies corresponding good or bad conduction so the sign of the temperature bias may affect the conduction and lead to rectification when the spectra of the parts are affected differently by the bias reversal. However, more recent research pointed out that anharmonicity is not a

necessary condition for an asymmetric match/mismatch and therefore for rectification [55]. Rectification also occurs in simple (minimalistic) harmonic models that incorporate some structural asymmetry and temperature-dependence of the model parameters [55]. This dependence may indeed result from an underlying, more intricate anharmonic system by linearization of the stochastic dynamics [55, 56], or it may have a different origin [57].

The contents of this part of the Thesis will be organized as follows. In chapter 4, I present a model of a thermal rectifier that relies on a localized impurity in the middle of a chain of atoms. In chapter 5, a proposal for a thermal rectifier in a chain of trapped ions with a graded frequency distribution is presented. Finally, in chapter 6, I study heat transport in a solvable model of two connected oscillators to explore the origin an optimization of thermal rectification.

Part I

Non-Hermitian systems and asymmetric scattering

Chapter 1

Asymmetric scattering by non-Hermitian potentials

“You must unlearn what you have learned.”

Master Yoda

The Empire Strikes Back

In this chapter I study the properties of potentials with asymmetric transmission or reflection for a quantum, spinless particle of mass m satisfying the one-dimensional (1D) Schrödinger equation. I propose six types of asymmetric devices according to the asymmetries of the transmission/reflection coefficients, see fig. 1.1. Non-Hermitian and non-local potentials will be necessary to construct this kind of devices, therefore an important part of this chapter will consist in studying their properties. In particular we will study their symmetries. Symmetries can be used, analogously to their standard application in atomic physics, to determine selection rules for allowed/forbidden transitions and to predict whether a certain potential may or may not lead to asymmetric scattering. Importantly, the concept of symmetry must be generalized when dealing with non-Hermitian potentials.

The theory in this chapter is worked out for particles and the Schrödinger equation but it is clearly of relevance for optical devices due to the much exploited

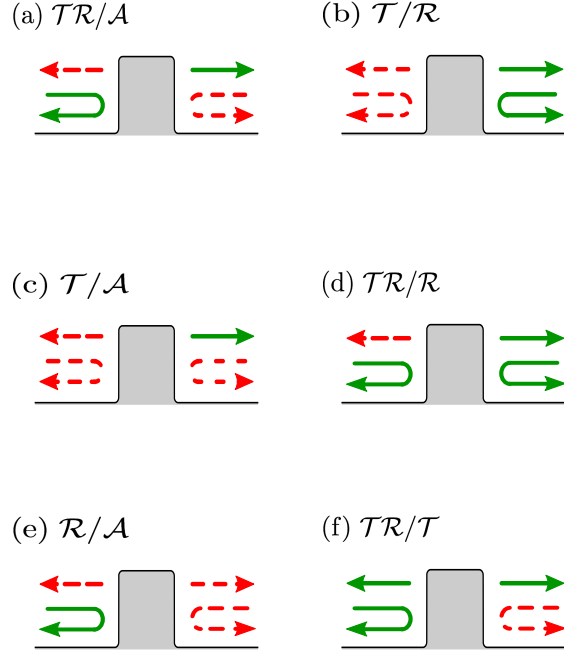


FIGURE 1.1: Devices with asymmetric scattering (limited to scattering coefficients being 0 or 1). The dashed and continuous lines represent respectively zero or one for the moduli of the scattering amplitudes; the bended lines are for reflection amplitudes, and the straight lines for transmission: (a) One-way mirror ($\mathcal{T}\mathcal{R}/\mathcal{A}$); (b) One-way barrier (\mathcal{T}/\mathcal{R}); (c) One-Way T-filter (\mathcal{T}/\mathcal{A}); (d) Mirror & 1-way transmitter ($\mathcal{T}\mathcal{R}/\mathcal{R}$); (e) One-way R-filter (\mathcal{R}/\mathcal{A}); (f) Transparent, one-way reflector ($\mathcal{T}\mathcal{R}/\mathcal{T}$). The nomenclature for the devices is explained in the main text of section 1.4.

analogies and connections between Maxwell's equations and the Schrödinger equation, which were used, e.g., to propose the realization of PT-symmetric potentials in optics [7].

The rest of the chapter goes as follows. In sections 1.1 and 1.2 I introduce the basics of scattering formalism and the concept of left/right eigenvectors, which will be fundamental to understand the rest of the chapter. In section 1.3 the concept of symmetry will be generalized for non-Hermitian Hamiltonians. A set of selection rules will be derived for the scattering coefficients. In section 1.4 I will describe the 6 types of asymmetric devices and how the different selection rules from the generalized symmetries of the Klein 4-group (composed by the identity, parity, time reversal and PT-symmetry) affect them. In section 1.5 some examples of non-local potentials leading to asymmetric scattering are given. In section 1.6 I give an example of a local PT potential that has completely asymmetric reflection in a broad range of incident momenta. Finally, in section 1.7 I summarize the main results of this chapter.

1.1 Non-Hermitian scattering in 1 dimension

In this section I will put together a minimum set of concepts and tools needed to describe scattering in 1 dimension. The ideas in this section can be found with more detail in [3], which generalizes the results in the celebrated book by Taylor [58] to non-Hermitian Hamiltonians. In scattering theory one deals with the Hamiltonian for a particle of mass m subjected to the action of a potential V

$$H = H_0 + V, \quad (1.1)$$

where $H_0 = P^2/(2m)$ is the kinetic energy operator, with P the momentum operator. The potential V is not assumed to be either Hermitian or local. Before continuing, I shall clarify these two statements. A linear operator \mathcal{O} is Hermitian if it is equal to its adjoint operator \mathcal{O}^\dagger , with the definition of the adjoint given by

$$\langle \phi | \mathcal{O} \psi \rangle = \langle \mathcal{O}^\dagger \phi | \psi \rangle \quad \forall |\psi\rangle, |\phi\rangle \in \mathcal{H}, \quad (1.2)$$

where \mathcal{H} is the Hilbert space of the particle. A potential V with a diagonal representation in the position basis $\{|x\rangle\}$ of the particle's Hilbert space is said to be local,

$$\langle x | V_{local} | x' \rangle = \delta(x - x')V(x'), \quad (1.3)$$

whereas a non-local potential has off-diagonal elements

$$\langle x | V_{nonlocal} | x' \rangle = V(x, x'). \quad (1.4)$$

The potentials that we study are in general non-diagonal and satisfy $V \neq V^\dagger$, therefore, the Hamiltonians will also be non-Hermitian, $H \neq H^\dagger$.

Scattering theory addresses the following question: given an input (incident) wave packet $|\psi_{in}\rangle$, what is the output (outgoing) wave packet $|\psi_{out}\rangle$ after interacting with the potential? Since the wave packet is a superposition of plane waves we may reformulate it in terms of its components, namely, given an incoming state with a momentum p , what are the probability amplitudes of the state being reflected and transmitted elastically (with the same energy)? To answer these questions the scattering theory brings in the scattering states, eigenstates of the Hamiltonian which belong to the continuum part of the spectrum, *i.e.*, eigenstates of the Hamiltonian which are not bounded to a finite portion of space and

behave asymptotically as plane waves far from the range of action of the potential. The scattering states represent incoming waves with momentum p and energy $E_p = p^2/(2m) > 0$ that are partially reflected and transmitted by the potential. For a plane wave with momentum $p > 0$ incoming from the left which is transmitted to the right and reflected back, the scattering state $|p^+\rangle$ is, asymptotically,

$$\langle x|p^+\rangle = \begin{cases} \langle x|p\rangle + R^l(p)\langle x|-p\rangle & \text{if } x \rightarrow -\infty \\ T^l(p)\langle x|p\rangle & \text{if } x \rightarrow \infty \end{cases}, \quad (1.5)$$

where $T^l(p)$ and $R^l(p)$ are the transmission and reflection amplitudes for left incidence. $\langle x|p\rangle = (2\pi\hbar)^{-1/2}e^{-ipx/\hbar}$ is the delta-normalized momentum eigenstate. Similarly, for a plane wave incoming from the right with momentum $-p$ ($p > 0$) which is transmitted to the left and reflected back, the scattering state $| -p^+\rangle$ is, asymptotically

$$\langle x| -p^+\rangle = \begin{cases} T^r(p)\langle x|-p\rangle & \text{if } x \rightarrow -\infty \\ \langle x|-p\rangle + R^r(p)\langle x|p\rangle & \text{if } x \rightarrow \infty \end{cases}, \quad (1.6)$$

where $T^r(p)$ and $R^r(p)$ are the transmission and reflection coefficients for right incidence. We shall see that in general $T^l \neq T^r$, $R^l \neq R^r$ for Hamiltonians that are non-Hermitian and non-local. For the adjoint of the Hamiltonian $H^\dagger = P^2/(2m) + V^\dagger$, we can also find the scattering states and amplitudes for left and right incidence: $\widehat{T}^l(p)$, $\widehat{R}^l(p)$, $\widehat{T}^r(p)$ and $\widehat{R}^r(p)$. In the rest of this Thesis I will use the convention that hatted variables $\widehat{\dots}$ will refer to the adjoint Hamiltonian H^\dagger . In the following, all the results I present for H can be found also for H^\dagger by making the change $H \rightarrow H^\dagger$.

Scattering theory provides the method to calculate the scattering amplitudes through the transition operator $T_{op}(z)$, which is defined as

$$T_{op}(z) = V + VG(z)V, \quad (1.7)$$

with $G(z) = (z - H)^{-1}$ being the Green's operator. In [3] the transition operator is used to write the scattering eigenstates as

$$|\pm p^+\rangle = |\pm p\rangle + \lim_{\varepsilon \rightarrow 0^+} G^0(E_p + i\varepsilon)T_{op}(E_p + i\varepsilon)|\pm p\rangle \quad (p > 0), \quad (1.8)$$

where $G^0(z) = (z - H_0)^{-1}$ is the Green's operator for free propagation. Now, to

find the scattering amplitudes of reflection and transmission, one has to take the limits of $\langle x|\pm p^+\rangle$, where $|\pm p^+\rangle$ is given by eq. (1.8), when $|x|$ goes to infinity and compare with eqs. (1.5), (1.6) to get

$$\begin{aligned} R^l &= -i \frac{2\pi m}{p} \langle -p | T_{op}(+) | p \rangle, \\ T^l &= 1 - i \frac{2\pi m}{p} \langle p | T_{op}(+) | p \rangle, \\ R^r &= -i \frac{2\pi m}{p} \langle p | T_{op}(+) | -p \rangle, \\ T^r &= 1 - i \frac{2\pi m}{p} \langle -p | T_{op}(+) | -p \rangle, \end{aligned} \quad (1.9)$$

where $T_{op}(+)$ is a shorthand notation for $\lim_{\varepsilon \rightarrow 0^+} T_{op}(E_p + i\varepsilon)$. The same procedure can be followed using the transition operator \hat{T}_{op} for H^\dagger to obtain $\hat{T}^l(p)$, $\hat{R}^l(p)$, $\hat{T}^r(p)$ and $\hat{R}^r(p)$. It is convenient to introduce the on-shell scattering matrix, defined as

$$S(p) = \begin{pmatrix} T^l(p) & R^r(p) \\ R^l(p) & T^r(p) \end{pmatrix}, \quad (1.10)$$

which gives the reflected and transmitted components for an incident plane wave. Waves propagating from left to right are represented as $(1, 0)^\top$ and waves propagating from right to left as $(0, 1)^\top$. Therefore, a left incident wave will be scattered to $(T^l(p), R^l(p))^\top$ and a right incident wave to $(R^r(p), T^r(p))^\top$.

As I mentioned before, one of the goals of scattering theory is connecting an input state $|\psi_{in}\rangle$ to an output state $|\psi_{out}\rangle$. The way of doing this is through the collision or scattering operator S

$$|\psi_{out}\rangle = S |\psi_{in}\rangle. \quad (1.11)$$

S is the product of the Möller operators $S = \Omega_-^\dagger \Omega_+$, which are defined as

$$\begin{aligned} \Omega_+ &= \lim_{t \rightarrow -\infty} e^{iHt/\hbar} e^{-iH_0 t/\hbar}, \\ \Omega_- &= \lim_{t \rightarrow +\infty} e^{iH^\dagger t/\hbar} e^{-iH_0 t/\hbar}. \end{aligned} \quad (1.12)$$

The Möller $\hat{\Omega}_\pm$ and scattering \hat{S} operators for the adjoint Hamiltonian can be found by substituting H for H^\dagger in eq. (1.12). The Möller operator with the $+(-)$ symbol connects the input (output) state with the scattering states of the

Hamiltonian. The Möller operators satisfy the isometry relation

$$\Omega_{\pm}^{\dagger} \Omega_{\pm} = 1, \quad (1.13)$$

and the following intertwining equations with the complete and free Hamiltonians H , H_0

$$\begin{aligned} H\Omega_{+} &= \Omega_{+}H_0, \\ H^{\dagger}\Omega_{-} &= \Omega_{-}H_0. \end{aligned} \quad (1.14)$$

The hatted quantities for the adjoint Hamiltonian have expressions similar to those in eqs. (1.13) and (1.14) with the substitution $H \leftrightarrow H^{\dagger}$. Because of eq. (1.14) and because the momentum eigenstates $|p\rangle$ are eigenstates of H_0 with energy E_p , the scattering states in eqs. (1.5) and (1.6) are also given by

$$|\pm p^{+}\rangle = \Omega_{+} |\pm p\rangle \quad (p > 0). \quad (1.15)$$

If the Hamiltonian is not Hermitian, the scattering operator will not be unitary in general. Because of this non-unitarity, input states may, for example, be absorbed by the potential. However, the scattering operator S and the scattering operator \widehat{S} of the adjoint Hamiltonian H^{\dagger} satisfy the generalized unitarity relation

$$\widehat{S}^{\dagger} S = S \widehat{S}^{\dagger} = 1. \quad (1.16)$$

The generalized unitary relation (1.16) implies a set of relations for the scattering amplitudes of non-Hermitian Hamiltonians. To find these relations one needs to find the matrix elements of S and \widehat{S} in the momentum basis. According to [3] the matrix elements of the scattering operator are related to the transition operator by

$$\langle p | S | p' \rangle = \delta(p - p') - 2i\pi\delta(E_p - E_{p'}) \langle p | T_{op}(+) | p' \rangle. \quad (1.17)$$

Factorizing out the Dirac delta in momentum using that $\delta(p - p') = \frac{|p|}{m}\delta(E_p - E_{p'})$ and considering positive momenta p and p' we get

$$\begin{pmatrix} \langle p | S | p' \rangle & \langle p | S | -p' \rangle \\ \langle -p | S | p' \rangle & \langle -p | S | -p' \rangle \end{pmatrix} = \frac{|p|}{m}\delta(E_p - E_{p'})\mathbf{S}(p). \quad (1.18)$$

Because of (1.18), the on-shell scattering matrices S and \widehat{S} (of the adjoint Hamiltonian) inherit the generalized unitarity relation of the scattering operators (1.16), yielding the following useful relations for the scattering amplitudes

$$\widehat{S}^\dagger S = 1 \implies \begin{cases} \widehat{T}^l(p)T^{l*}(p) + \widehat{R}^l(p)R^{l*}(p) &= 1, \\ \widehat{T}^r(p)T^{r*}(p) + \widehat{R}^r(p)R^{r*}(p) &= 1, \\ \widehat{T}^{l*}(p)R^r(p) + T^r(p)\widehat{R}^{l*}(p) &= 0, \\ T^l(p)\widehat{R}^{r*}(p) + \widehat{T}^{r*}(p)R^l(p) &= 0. \end{cases} \quad (1.19)$$

The relations in (1.19) will be extremely relevant in the following, as they set extra conditions for the scattering amplitudes of asymmetric devices.

1.1.1 Why is non-Hermiticity needed for asymmetric scattering?

Asymmetric scattering is achieved when $|T^l| \neq |T^r|$ or $|R^l| \neq |R^r|$. When the Hamiltonian is Hermitian, the hatted quantities in eq. (1.19) are equal to the unhatted ones and, therefore, eq. (1.19) becomes

$$\begin{aligned} |T^l(p)|^2 + |R^l(p)|^2 &= 1, \\ |T^r(p)|^2 + |R^r(p)|^2 &= 1, \\ T^{l*}(p)R^r(p) + T^r(p)R^{l*}(p) &= 0. \end{aligned} \quad (1.20)$$

Taking absolute values in the last equation in (1.20) and solving for $T^r(p)$ gives

$$|T^r(p)| = \left| T^l(p) \frac{R^r(p)}{R^l(p)} \right|. \quad (1.21)$$

Now, because of the first equation in (1.20) we get $|R^r(p)| = |R^l(p)|$. Finally, subtracting the two first equations in (1.20) one arrives at $|T^r(p)| = |T^l(p)|$ (in fact, the stronger relation $T^l(p) = T^r(p)$ holds [3]). Therefore, it is impossible to build asymmetric devices with Hermitian Hamiltonians.

1.2 Right and left eigenvectors of non-Hermitian Hamiltonians

Eigenstates in the discrete part of the spectrum (bound-in-space eigenstates) of a Hermitian Hamiltonian corresponding to different eigenvalues are orthogonal, *i.e.* $\langle E_i | E_j \rangle = 0$ if $E_i \neq E_j$. One can choose the normalization $\langle E_i | E_j \rangle = \delta_{ij}$, which makes the eigenstates an orthonormal set. Similarly, the scattering states $|p^+\rangle$ satisfy (in the Hermitian case) $\langle p^+ | p'^+ \rangle = \delta(p - p')$. The discrete and scattering eigenstates span orthonormal bases in their corresponding subspaces and can be used to form a basis of the complete Hilbert space in the following way,

$$1 = \sum_i |E_i\rangle\langle E_i| + \int dp |p^+\rangle\langle p^+|. \quad (1.22)$$

It is possible to generalize (1.22) for a non-Hermitian hamiltonian using a biorthogonal basis. We say that the vectors $|\lambda\rangle$ and $|\widehat{\lambda}\rangle$ are a right and a left pair of eigenvectors if there exists a λ eigenvalue such that

$$\begin{aligned} H |\lambda\rangle &= \lambda |\lambda\rangle, \\ \langle \widehat{\lambda} | H &= \langle \widehat{\lambda} | \lambda. \end{aligned} \quad (1.23)$$

For two different eigenvalues λ_1 and λ_2 , it is easy to show that $\langle \widehat{\lambda}_1 | \lambda_2 \rangle = \langle \widehat{\lambda}_2 | \lambda_1 \rangle = 0$, and for this reason, the pairs $|\lambda\rangle$, $|\widehat{\lambda}\rangle$ are called biorthogonal partners. This result is applied to scattering Hamiltonians in the following way. In the discrete spectrum of H , we can choose the normalization $\langle \widehat{E}_i | E_j \rangle = \delta_{ij}$ for the point spectrum eigenvectors. The right scattering states are given by eq. (1.15). Using the intertwining relations (1.14) for the hatted Moller operators (after the $H \leftrightarrow H^\dagger$ substitution) one can prove that the states $|\widehat{p}^+\rangle = \widehat{\Omega}_+ |p\rangle$ are left eigenvectors of H with eigenvalue E_p . The isometry relation (1.13) implies $\langle \widehat{p}^+ | p'^+ \rangle = \delta(p - p')$, therefore the pairs $|\widehat{p}^+\rangle$, $|p^+\rangle$ are biorthogonal partners. Finally, the completeness formula of the Hilbert space (1.22) is generalized to the non-Hermitian case as

$$1 = \sum_i |E_i\rangle\langle \widehat{E}_i| + \int dp |p^+\rangle\langle \widehat{p}^+|. \quad (1.24)$$

1.3 Generalized symmetries

For Hermitian Hamiltonians, symmetries are represented by the commutation of some symmetry operator A with the Hamiltonian. According to Wigner's theorem [59], a symmetry operator A has to be either unitary or antiunitary. Unitary and antiunitary operators are defined by the relation $A^\dagger A = AA^\dagger = 1$. Unitary operators are linear, and therefore the adjoint is defined by eq. (1.2), whereas antiunitary operators are antilinear, so the adjoint is defined by

$$\langle \phi | \mathcal{O} \psi \rangle = \langle \mathcal{O}^\dagger \phi | \psi \rangle^* \quad \forall |\psi\rangle, |\phi\rangle \in \mathcal{H}. \quad (1.25)$$

In Hermitian scattering theory, symmetry plays an important role as it implies relations among the S-matrix elements beyond those implied by its unitarity, see e.g. [58] and, for scattering in one dimension, Sec. 2.6 in [3]. Symmetries are also useful for non-Hermitian Hamiltonians, but the mathematical and conceptual framework must be generalized. We consider that a unitary or antiunitary operator A represents a symmetry of H if it satisfies at least one of these relations,

$$AH = HA, \quad (1.26)$$

$$AH = H^\dagger A. \quad (1.27)$$

For a right eigenstate of H , $|\psi\rangle$, with eigenvalue E , eq. (1.26) implies that $A|\psi\rangle$ is also a right eigenstate of H , with the same eigenvalue if A is unitary, and with the complex conjugate eigenvalue E^* if A is antiunitary. Equation (1.27) implies that $A|\psi\rangle$ is a right eigenstate of H^\dagger with eigenvalue E for A unitary or E^* for A antiunitary, or a left eigenstate of H with eigenvalue E^* for A unitary, or E for A antiunitary. For real-energy scattering eigenfunctions in the continuum, the ones we are interested in here, $E^* = E$. When eq. (1.27) holds we say that H is A -pseudohermitian [60]. Parity-pseudohermiticity has played an important role as being equivalent to space-time reflection (PT) symmetry for *local* potentials [20, 60]. A large set of these equivalences will be discussed below. A relation of the form (1.27) has been also used with differential operators to get real spectra beyond PT-symmetry for local potentials [10, 11].

Here we consider A to be a member of the Klein 4-group $K_4 = \{1, \Pi, \Theta, \Pi\Theta\}$ formed by unity, the parity operator Π , the antiunitary time-reversal operator Θ , and their product $\Pi\Theta$. The Klein 4-group is a discrete, Abelian group and every

element A satisfies $A^2 = 1$. We also assume that the Hamiltonian is of the form $H = H_0 + V$, with H_0 , the kinetic energy operator of the particle, being Hermitian and satisfying $[H_0, A] = 0$ for all members of the group, whereas the potential V may be non-local in position representation. The motivation to use Klein's group is that the eight relations implied by eqs. (1.26) and (1.27) generate all possible symmetry transformations of a non-local potential due to the identity, complex conjugation, transposition, and sign inversion, both in coordinate or momentum representation, see the 3rd and 4th columns of table 1.1, where each symmetry has been labeled by a roman number.

TABLE 1.1: Symmetries of the potential classified in terms of the commutativity or pseudo-Hermiticity of H with the elements of Klein's 4-group $\{1, \Pi, \theta, \Pi\theta\}$ (second column). The first column sets a simplifying roman-number code for each symmetry. The relations among potential matrix elements are given in coordinate and momentum representations in the third and fourth columns. The fifth column gives the relations they imply in the matrix elements of S and/or \widehat{S} matrices (S is for scattering by H and \widehat{S} for scattering by H^\dagger). From them the next four columns set the relations implied on scattering amplitudes. Together with generalized unitarity relations ((1.19)) they also imply relations for the moduli (tenth column), and phases (not shown). The last two columns indicate the possibility to achieve perfect asymmetric transmission or reflection: “ P ” means possible (but not necessary), “No” means impossible. In some cases “ P ” is accompanied by a condition that must be satisfied.

(1) Code	(2) Symmetry	$\langle x V y\rangle =$	$\langle p V p'\rangle =$	$\langle p S p'\rangle =$	$\langle p \widehat{S} p'\rangle =$	$T^l =$	$T^r =$	$R^l =$	$R^r =$	$\langle T^l =$	$\langle T^r =$	$\langle R^l =$	$\langle R^r =$
I	$1H = H1$	$\langle x V y\rangle$	$\langle p V p'\rangle$	$\langle p S p'\rangle$	$\langle p \widehat{S} p'\rangle$	T^l	T^r	R^l	R^r	$ T^l = T^r , R^l = R^r $	$ T^l = T^r , R^l = R^r $	P	P
II	$1H = H^\dagger 1$	$\langle y V x\rangle^*$	$\langle p' V p\rangle^*$	$\langle p \widehat{S} p'\rangle$	$\langle -p \widehat{S} p'\rangle$	\widehat{T}^l	\widehat{T}^r	\widehat{R}^l	\widehat{R}^r	$ T^l = T^r , R^l = R^r $	$ T^l = T^r , R^l = R^r $	No	No
III	$\Pi H = H\Pi$	$\langle -x V -y\rangle$	$\langle -p V -p'\rangle$	$\langle -p S -p'\rangle$	$\langle -p \widehat{S} -p'\rangle$	T^l	T^r	R^l	R^r	$ T^l = T^r , R^l = R^r $	$ T^l = T^r , R^l = R^r $	No	No
IV	$\Pi H = H^\dagger \Pi$	$\langle -y V -x\rangle^*$	$\langle -p' V -p\rangle^*$	$\langle -p \widehat{S} -p\rangle^*$	$\langle -p' \widehat{S} -p\rangle^*$	\widehat{T}^l	\widehat{T}^r	\widehat{R}^l	\widehat{R}^r	$ T^l = T^r , R^l = R^r $	$ T^l = T^r , R^l = R^r $	$P, TR^{l*}=1$	$P, TR^{l*}=1$
V	$\Theta H = H\Theta$	$\langle x V y\rangle^*$	$\langle -p V -p'\rangle^*$	$\langle -p' \widehat{S} -p\rangle^*$	$\langle -p' \widehat{S} -p\rangle^*$	\widehat{T}^l	\widehat{T}^r	\widehat{R}^l	\widehat{R}^r	$ R^l = R^r $	$ R^l = R^r $	$P, RR^{l*}=1$	$P, RR^{l*}=1$
VI	$\Theta H = H^\dagger \Theta$	$\langle y V x\rangle$	$\langle -p V -p\rangle$	$\langle -p S -p\rangle$	$\langle -p' \widehat{S} -p\rangle$	T^l	T^r	R^l	R^r	$ T^l = T^r $	$ T^l = T^r $	No	No
VII	$\Theta\Pi H = H\Theta\Pi$	$\langle -x V -y\rangle^*$	$\langle p V p\rangle^*$	$\langle p \widehat{S} p\rangle$	$\langle p' \widehat{S} p\rangle$	\widehat{T}^l	\widehat{T}^r	\widehat{R}^l	\widehat{R}^r	$ T^l = T^r $	$ T^l = T^r $	P	P
VIII	$\Theta\Pi H = H^\dagger \Theta\Pi$	$\langle -y V -x\rangle$	$\langle p' V p\rangle$	$\langle p' S p\rangle$	$\langle p' S p\rangle$	T^l	T^r	R^l	R^r	$ R^l = R^r $	$ R^l = R^r $	P	P

TABLE 1.2: Transformation rules of the Möller and scattering operators with linear and antilinear operators.

Type of symmetry	A linear	A antilinear
$AH = HA$	$\begin{aligned} A\Omega_{\pm} &= \Omega_{\pm}A \\ AS &= SA \end{aligned}$	$\begin{aligned} A\Omega_{\pm} &= \widehat{\Omega}_{\mp}A \\ AS &= \widehat{S}^{\dagger}A \end{aligned}$
$AH = H^{\dagger}A$	$\begin{aligned} A\Omega_{\pm} &= \widehat{\Omega}_{\pm}A \\ AS &= \widehat{S}A \end{aligned}$	$\begin{aligned} A\Omega_{\pm} &= \Omega_{\mp}A \\ AS &= S^{\dagger}A \end{aligned}$

With the definitions of symmetry in eqs. (1.26), (1.27) and the tools from scattering formalism in 1.1 we can now find the effects of the symmetries in the scattering operator S , which will pose restrictions in the scattering amplitudes. We start by specifying the transformation rules of the Möller operators (1.12) under a symmetry operator A of the Klein 4-group. The Möller operators are transformed differently depending on whether A is unitary or antiunitary and whether the Hamiltonian obeys a usual symmetry (1.26) or pseudohermiticity (1.27). For example, for A unitary and (1.26) we have

$$\begin{aligned}
 A\Omega_+ &= A \lim_{t \rightarrow -\infty} e^{iHt/\hbar} e^{-iH_0t/\hbar} \\
 &= \lim_{t \rightarrow -\infty} e^{iHt/\hbar} A e^{-iH_0t/\hbar} \\
 &= \lim_{t \rightarrow -\infty} e^{iHt/\hbar} e^{-iH_0t/\hbar} A \\
 &= \Omega_+ A,
 \end{aligned} \tag{1.28}$$

and

$$\begin{aligned}
 A\Omega_- &= A \lim_{t \rightarrow +\infty} e^{iH^{\dagger}t/\hbar} e^{-iH_0t/\hbar} \\
 &= \lim_{t \rightarrow +\infty} e^{iH^{\dagger}t/\hbar} A e^{-iH_0t/\hbar} \\
 &= \lim_{t \rightarrow +\infty} e^{iH^{\dagger}t/\hbar} e^{-iH_0t/\hbar} A \\
 &= \Omega_- A.
 \end{aligned} \tag{1.29}$$

Using eqs. (1.28) and (1.29) we finally get

$$\begin{aligned}
 AS &= A\Omega_-^\dagger\Omega_+ \\
 &= \Omega_-^\dagger A\Omega_+ \\
 &= \Omega_-^\dagger\Omega_+ A \\
 &= SA, \\
 &\Downarrow \\
 S &= A^\dagger SA.
 \end{aligned} \tag{1.30}$$

The rest of combinations of the type of A (unitary/antiunitary) with the type of symmetry ((1.26) or (1.27)) are summarized in table 1.2. Since the symmetry operators commute with the free Hamiltonian H_0 , the action of any of them on a momentum eigenstate will give, as a result, a state with the same energy. In fact, as can be seen in table 1.3, the result of the action of any element A of the 4-group on a state $|p\rangle$ is either $|p\rangle$ or $|-p\rangle$. For this reason, we can work with the on-shell representation of the scattering operator to obtain extra relations between the scattering amplitudes. As an example I will demonstrate what happens to the scattering amplitudes when the symmetry III is satisfied, *i.e.*, $\Pi H = H\Pi$. Considering a momentum $p > 0$ and using $S = \Pi^\dagger S\Pi$ (see table 1.2) I find

$$\begin{pmatrix} \langle p|S|p\rangle & \langle p|S| -p\rangle \\ \langle -p|S|p\rangle & \langle -p|S| -p\rangle \end{pmatrix} = \begin{pmatrix} \langle -p|S| -p\rangle & \langle -p|S|p\rangle \\ \langle p|S| -p\rangle & \langle p|S|p\rangle \end{pmatrix}. \tag{1.31}$$

Now, using the on-shell representation of the scattering operator (1.18) and the definition of $S(p)$ (1.10) I arrive at

$$\begin{aligned}
 T^l(p) &= T^r(p), \\
 R^l(p) &= R^r(p).
 \end{aligned} \tag{1.32}$$

Instead of deriving the equivalent relation to (1.32) for all the symmetries explicitly, I summarize the results for the matrix elements of the S operator in the 5th column and for the scattering amplitudes in the columns 6-9 of table 1.1. Explicit examples on how to find the relations in the 5th and 6th columns of table 1.1 for other symmetries can be found in [3].

If we now take into account the generalized unitary relations $\widehat{S}^\dagger S = S\widehat{S}^\dagger = 1$, in terms of amplitudes (1.19), the columns 6-9 of table 1.1 imply further consequences

TABLE 1.3: Action of the Klein 4-group operators on the position and momentum eigenkets. A scalar $\alpha \in \mathbb{C}$ is included in the table to make the unitary/antiunitary nature of the elements of the group explicit.

	$\alpha x\rangle$	$\alpha p\rangle$
1	$\alpha x\rangle$	$\alpha p\rangle$
Π	$\alpha -x\rangle$	$\alpha -p\rangle$
Θ	$\alpha^* x\rangle$	$\alpha^* -p\rangle$
$\Pi\Theta$	$\alpha^* -x\rangle$	$\alpha^* p\rangle$

on the amplitudes' moduli (tenth column of table 1.1) and phases (not shown). The final two columns use the previous results to determine if perfect asymmetry is possible for transmission or reflection. This makes evident that Hermiticity (II) and parity (III) preclude, independently, any asymmetry in the scattering coefficients; PT-symmetry (VII) or Θ -pseudohermiticity (VI) forbid transmission asymmetry (all local potentials satisfy automatically symmetry VI), whereas time-reversal symmetry (i.e., a real potential in coordinate space) (V) or PT-pseudohermiticity (VIII) forbid reflection asymmetry.

1.3.1 Equivalences between symmetries

The occurrence of one particular symmetry in the potential (conventionally “first symmetry”) does not exclude a second symmetry to be satisfied as well. When a double symmetry holds, excluding the identity, the “first” symmetry implies the equivalence of the second symmetry with a third symmetry. We have already mentioned that Π -pseudohermiticity (IV) is equivalent to PT -symmetry (VII) for local potentials. Being local is just one particular way to satisfy symmetry VI, namely Θ -pseudohermiticity. The reader may verify with the aid of the third column for $\langle x|V|y\rangle$ in table 1.1, that indeed, if symmetry VI is satisfied (first symmetry), symmetry IV has the same effect as symmetry VII. They become equivalent. Another well known example is that for a local potential (symmetry VI is satisfied), a real potential in coordinate space is necessarily Hermitian, so symmetries V and II become equivalent. These examples are just particular cases of the full set of equivalences given in table 1.4. The concept of equivalence for symmetries was refined and studied in more detail in [16].

TABLE 1.4: Equivalences among symmetries for the potential elements. Given the symmetry of the upper row, the table provides the equivalent symmetries. For example, if II is satisfied, then III=IV holds. In words, if the potential is Hermitian, parity symmetry amounts to parity pseudohermiticity. In terms of the matrix elements of the potential, if $\langle x|V|y\rangle = \langle y|V|x\rangle^*$ and also $\langle x|V|y\rangle = \langle -x|V| - y\rangle$, $\forall(x,y)$, then $\langle x|V|y\rangle = \langle -y|V| - x\rangle^*$ holds as well. One may proceed similarly for all other relations. The commutation with the identity (I) is excluded as this symmetry is satisfied by all potentials.

II	III	IV	V	VI	VII	VIII
III=IV	II=IV	II=III	II=VI	II=V	II=VIII	II=VII
V=VI	V=VII	V=VIII	III=VII	III=VIII	III=V	III=VI
VII=VIII	VI=VIII	VI=VII	IV=VIII	IV=VII	IV=VI	IV=V

1.4 Asymmetric devices

I will describe now the set of devices that we want to design and how the eight non-Hermitian symmetries of the Klein 4-group make this possible or impossible in some cases. Table 1.5 gives a descriptive list of the 6 kinds of asymmetric devices that we consider (see also fig. 1.1 for a schematic representation of the devices). The first column gives the name that we have chosen for each of the devices. Second and third columns show the expected behaviour for left or right incidence, respectively. The fourth column shows the descriptive code for each of the devices. The descriptive codes have always the following structure, LI/RI , where LI and RI are codes that describe the behaviour for left and right incidence respectively. LI and RI are composed by a combination of the symbols \mathcal{T} , \mathcal{R} , \mathcal{A} . \mathcal{T} stands for devices with full transmission ($|T| = 1$), \mathcal{R} for full reflection ($|R| = 1$). \mathcal{A} is the code for full absorption ($|R| = |T| = 0$). For example, a device with reflection asymmetry $|R^l| = 1$, $|R^r| = 0$ and with $|T^r| = |T^l| = 1$ would in our case be a particular “transparent, one-way reflector”, as full transmission occurs from both sides and its descriptive code would be $\mathcal{T}\mathcal{R}/\mathcal{T}$. This effect is known as “unidirectional invisibility” [61, 62]. The device denominations in fig. 1.1 or table 1.5 are intended to be compact and systematic, and do not necessarily coincide with some extended terminology, in part because the range of possibilities is broader here than those customarily considered, and because we use a 1 or 0 condition for the moduli.

Combining the information of the last two-columns in table 1.1 with the additional condition that all scattering coefficients be 0 or 1, we elaborate the last two

columns of table 1.5, which provides the symmetries that do not allow the implementation of the devices in fig. 1.1. The complementary table 1.6 gives instead the symmetries that allow, but do not necessarily imply, a given type of device.

TABLE 1.5: Device types for transmission and/or reflection asymmetry, restricted to 1 or 0 moduli for the scattering amplitudes. The fifth column indicates the symmetries in table 1.1 that forbid the device.

Device type	Left incidence	Right incidence	Code	Forbidden by	Example
One-way mirror	transmits and reflects	absorbs	$\mathcal{T}\mathcal{R}/\mathcal{A}$	II, III, IV, V, VI, VII, VIII	
One-way barrier	transmits	reflects	\mathcal{T}/\mathcal{R}	II, III, IV, V, VI, VII, VIII	
One-way T-filter	transmits	absorbs	\mathcal{T}/\mathcal{A}	II, III, IV, V, VI, VII	fig. 1.2
Mirror&1-way transmitter	transmits and reflects	reflects	$\mathcal{T}\mathcal{R}/\mathcal{R}$	II, III, VI, VII	
One-way R-filter	reflects	absorbs	\mathcal{R}/\mathcal{A}	II, III, IV, V, VII, VIII	[63]
Transparent 1-way reflector	transmits and reflects	transmits	$\mathcal{T}\mathcal{R}/\mathcal{T}$	II, III, V, VII	figs. 1.3

TABLE 1.6: Device types allowed for a given symmetry.

Symmetry	Allowed devices
I	All types
II	None
III	None
IV	$\mathcal{T}\mathcal{R}/\mathcal{R}, \mathcal{T}\mathcal{R}/\mathcal{T}$
V	$\mathcal{T}\mathcal{R}/\mathcal{R}$
VI	$\mathcal{R}/\mathcal{A}, \mathcal{T}\mathcal{R}/\mathcal{T}$
VII	$\mathcal{T}\mathcal{R}/\mathcal{T}$
VIII	$\mathcal{T}/\mathcal{A}, \mathcal{T}\mathcal{R}/\mathcal{R}$

1.5 Designing potentials for asymmetric devices

We will demonstrate how to design non-local potentials with different asymmetric responses. For simplicity we look for non-local potentials $V(x, y)$ that vanish outside the finite region of space $|x| \leq d$ and $|y| \leq d$.

I follow an inverse scattering approach similar to [64]. This approach starts by imposing an ansatz for the wave functions and the potential in the stationary Schrödinger equation

$$\frac{\hbar^2 k^2}{2m} \psi(x) = -\frac{\hbar^2}{2m} \frac{d^2}{dx^2} \psi(x) + \int_{-d}^d dy V(x, y) \psi(y). \quad (1.33)$$

The free parameters are fixed making use of the boundary conditions. The form of the wave function incident from the left is $\psi_l(x) = e^{ikx} + R^l e^{-ikx}$ for $x < -d$ and $\psi_l(x) = T^l e^{ikx}$ for $x > d$, where $k = p/\hbar$. The wave function incident from the right is instead $\psi_r(x) = e^{-ikx} T^r$ for $x < -d$ and $\psi_r(x) = e^{-ikx} + R^r e^{ikx}$ for $x > d$.

Our strategy is to assume polynomial forms for the two wave functions in the interval $|x| < d$, $\psi_l(x) = \sum_{j=0}^5 c_{l,j} x^j$ and $\psi_r(x) = \sum_{j=0}^5 c_{r,j} x^j$, and also a polynomial ansatz of finite degree for the potential $V(x, y) = \sum_i \sum_j v_{ij} x^i y^j$. Inserting these ansatzes in eq. (1.33) and from the conditions that $\psi_{l,r}$ and their derivatives must be continuous, all coefficients $c_{l,j}$, $c_{r,j}$ and v_{ij} can be determined. Symmetry properties of the potential can also be imposed via additional conditions on the potential coefficients v_{ij} . For example we may use this method to obtain a one-way T-filter (\mathcal{T}/\mathcal{A}) device (third device in table 1.5) with a non-local PT-pseudohermitian potential (symmetry VIII of table 1.1) for a chosen wave vector $k = k_0$. The absolute value and argument of the resulting potential $V(x, y)$ are

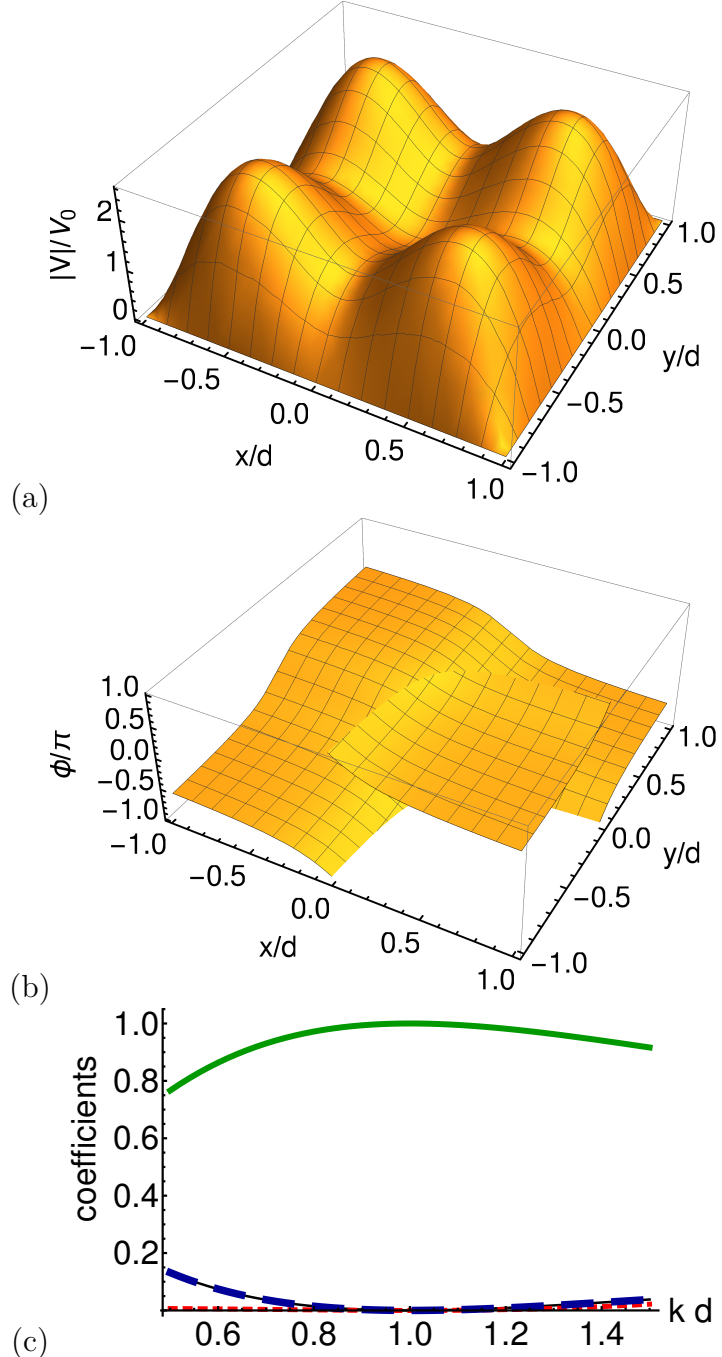


FIGURE 1.2: (Color online) One-way T-filter (\mathcal{T}/\mathcal{A} , $|T^l| = 1, T^r = R^l = R^r = 0$) with potential $V(x, y) = |V(x, y)|e^{i\phi(x, y)}$ set for $k_0 = 1/d$. (a) Absolute value $|V(x, y)|$; (b) Argument $\phi(x, y)$; (c) Transmission and reflection coefficients: $|R^l|^2$ (black, solid line), $|T^l|^2$ (green, solid line), $|R^r|^2$ (blue, tick, dashed line), $|T^r|^2$ (red, dotted line). $V_0 = \hbar^2/(2md^3)$.

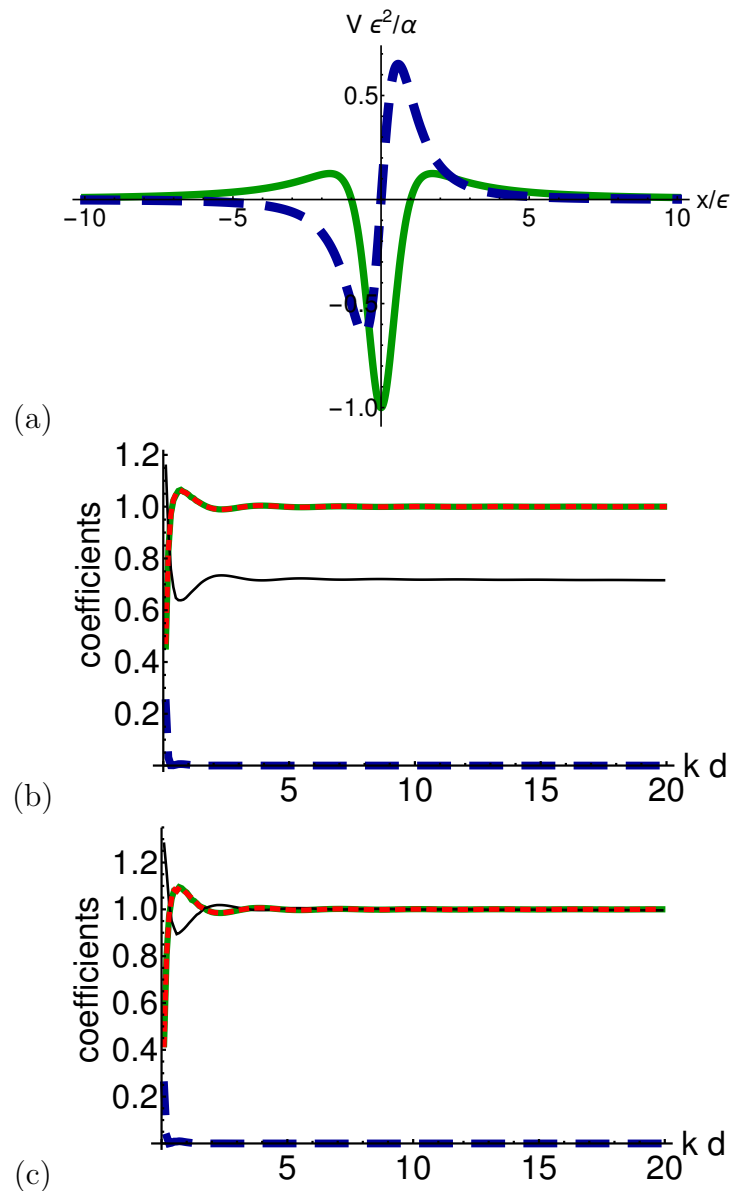


FIGURE 1.3: (Color online) Transparent 1-way reflector with a local PT potential: (a) Approximation of the potential (1.37), real part (green solid line), imaginary part (blue dashed line). (b,c) Transmission and reflection coefficients versus momentum kd ; left incidence: $|R^l|^2$ (black, solid line), $|T^l|^2$ (green, solid line); right incidence: $|R^r|^2$ (blue, tick, dashed line), $|T^r|^2$ (red, dotted line, coincides with green, solid line). $\epsilon/d = 10^{-4}$. (b) $\alpha = 1.0\hbar^2/(4\pi m)$ (c) $\alpha = 1.225\hbar^2/(4\pi m)$ (the black, solid line coincides here mostly with the red, dotted and green, solid lines).

shown in figs. 1.2(a) and 1.2(b) together with its scattering coefficients as a function of the incident wave vector, fig. 1.2(c). As can be seen in fig. 1.2(c) the imposed scattering coefficients are fulfilled exactly for the chosen wave vector. They are also satisfied approximately in a neighborhood of k_0 . Other examples of potentials for the devices in fig. 1.1 can be found in the supplemental material of ref. [13].

1.6 Extending the scattering asymmetry to a broad incident-momentum domain

The inversion technique just described may be generalized to extend the range of incident momenta for which the potential works by imposing additional conditions and increasing correspondingly the number of parameters in the wave function ansatz. For example we may impose that the derivatives of the amplitudes, in one or more orders, vanish at k_0 , or 0/1 values for the coefficients not only at k_0 but at a series of grid points k_1, k_2, \dots, k_N [3, 64–66].

Here we put forward instead a method that provides a very broad working-window domain. While we make formally use of the Born approximation, the exact numerical computations demonstrate the robustness and accuracy of the approach to achieve that objective by making use of an adjustable parameter in the potential. The very special role of the Born approximation in inverse problems has been discussed and demonstrated in [67–69]. Specifically we study a transparent one-way reflector $\mathcal{T}\mathcal{R}/\mathcal{T}$. Our aim is now to find a local PT-symmetric potential such that asymmetric reflection results, $T^l = T^r = 1, R^r = 0, |R^l| = 1$ for a broad range of incident momenta. A similar goal was pursued in [21] making use of a supersymmetric transformation, without imposing $|R^l| = 1$.

In the Born approximation and for a local potential $V(x)$, the reflection amplitudes take the simple form

$$R^l = -\frac{2\pi im}{p} \langle -p|V|p\rangle, \quad R^r = -\frac{2\pi im}{p} \langle p|V| - p\rangle. \quad (1.34)$$

Defining the Fourier transform

$$\tilde{V}(k) = \frac{1}{\sqrt{2\pi}} \int_{-\infty}^{\infty} dx V(x) e^{-ikx} \quad (1.35)$$

we get for $k = p/\hbar > 0$:

$$R^l = -\frac{\sqrt{2\pi}im}{k\hbar^2}\tilde{V}(-2k), \quad R^r = -\frac{\sqrt{2\pi}im}{k\hbar^2}\tilde{V}(2k). \quad (1.36)$$

Assuming that the potential is local and PT-symmetrical, we calculate the transition coefficient from them using generalized unitarity as $|T|^2 = 1 - R^{r*}R^l$.

To build a $\mathcal{T}\mathcal{R}/\mathcal{T}$ device we demand: $\tilde{V}(k) = \sqrt{2\pi}\alpha k$ ($k < 0$) and $\tilde{V}(k) = 0$ ($k \geq 0$). By inverse Fourier transformation, this implies

$$\begin{aligned} V(x) &= -\alpha \frac{\partial}{\partial x} \lim_{\epsilon \rightarrow 0} \frac{1}{x - i\epsilon} = \alpha \lim_{\epsilon \rightarrow 0} \frac{1}{(x - i\epsilon)^2} \\ &= \alpha \lim_{\epsilon \rightarrow 0} \left[\frac{x^2 - \epsilon^2}{(x^2 + \epsilon^2)^2} + i \frac{2x\epsilon}{(x^2 + \epsilon^2)^2} \right], \end{aligned} \quad (1.37)$$

which is indeed a local, PT -symmetric potential for α real. α is directly related to the reflection coefficient, within the Born approximation, $R^l = 4\pi im\alpha/\hbar^2$. As the Born approximation may differ from exact results, in the following we shall keep α as an adjustable parameter.

In a possible physical implementation, the potential in eq. (1.37) will be approximated by keeping a small finite $\epsilon > 0$, see fig. 1.3(a). Then, its Fourier transform is $\tilde{V}(k) = \sqrt{2\pi}\alpha k e^{\epsilon k}$ ($k < 0$) and $\tilde{V}(k) = 0$ ($k \geq 0$). In figs. 1.3(b) and (c), the resulting coefficients for $\epsilon/d = 10^{-4}$ and two different values of α are shown. These figures have been calculated by numerically solving the Schrödinger equation exactly. Remarkably, the Born approximation contains all the information required to build the required potential shape up to a global factor. Such a prominent role of the Born approximation in inverse problems has been noted in different applications [67–69]. For a range of α , the potential gives $|R^r| \approx 0$, a nearly constant $|R^l|^2$, and $|T^r| = |T^l| \approx 1$ in a broad k -domain, see fig. 1.3(b). Adjusting the value of α , fig. 1.3(c), sets $|R^l| \approx 1$ as desired.

1.7 Discussion

Scattering asymmetries are necessary to develop technologically relevant devices such as one-way mirrors, filters and barriers, invisibility cloaks, diodes, or Maxwell demons. So far, much effort has been devoted to build and apply local PT-symmetric potentials but the possible scattering asymmetries with them are

quite limited. We find that six types of devices with asymmetric scattering are possible when imposing 0 or 1 scattering coefficients. PT-symmetry can only realize one of them, but this symmetry is just one among eight possible symmetries of complex non-local potentials. The eight symmetries arise from the discovery that Klein's four-group $\{1, \Pi, \Theta, \Theta\Pi\}$, combined with two possible relations among the Hamiltonian, its adjoint, and the symmetry operators of the group, eqs. (1) and (2), produce all possible symmetries generated by complex conjugation, coordinate inversion and transposition. The conventional definition of a symmetry in terms of the commutation of a unitary/antiunitary operator A with the Hamiltonian H is not enough, and A -pseudohermiticity must be considered as well on the same footing. Extending the concept of what a symmetry is for complex, non-local potentials is a fundamental, far-reaching step of this work. This group theoretical analysis and classification is not only esthetically pleasing, but also of practical importance, as it reveals the underlying structure and span of the possibilities available in principle to manipulate the asymmetrical response of a potential for a structureless particle. Although the present theory is for the scattering of quantum particles, the analogies between quantum physics and optics suggest to extend the concepts and results for optical asymmetric devices.

Chapter 2

***S*-matrix pole symmetries for non-Hermitian scattering Hamiltonians**

Non-Hermitian Hamiltonians may have in general complex eigenvalues. However, in 1998 Carl M. Bender showed that non-Hermitian potentials having PT-symmetry can have a completely real spectra [19]. Later, in a series of works published in 2002, Ali Mostafazadeh generalized this finding [22, 70, 71]. A Hamiltonian with a discrete spectrum that satisfies (1.26), for a Hermitian and antilinear operator $A_{\text{antilinear}}$; or (1.27) for a Hermitian and linear operator A_{linear} , will have eigenvalues that are real or come in complex-conjugate pairs [22, 70, 71]. An aspect uncovered in refs. [22, 70, 71] is that, under the same conditions, the complex poles of the scattering matrix can also come in complex conjugate pairs.

This chapter aims at extending the results in chapter 1 and refs. [22, 70, 71] in several directions:

- i) I will provide an alternative characterization of the 8 symmetries formed by the elements of the Klein 4-group and the relations (1.26), (1.27) in terms of the invariance of H with respect to the action of superoperators.
- ii) Moreover, four of these eight symmetries imply the same type of pole structure of S -matrix eigenvalues in the complex momentum plane that was found for PT symmetry [3], namely, zero-pole correspondence at complex-conjugate points, and poles on the imaginary axis or forming symmetrical pairs with respect to the

imaginary axis. This configuration with poles located on the imaginary axis or as symmetrical pairs has some important consequences. In particular, it provides stability of the real energy eigenvalues with respect to parameter variations of the potential. While a simple pole on the imaginary axis can move along that axis when a parameter is changed, it cannot move off this axis (since this would violate the pole-pair symmetry) or bifurcate. The formation of pole pairs occurs near special parameter values for which two poles on the imaginary axis collide. When the poles are mapped to the energy complex plane $E = p^2/2m$, they have the same symmetry structure of complex conjugate pairs as the discrete eigenvalues of an A -pseudohermitian Hamiltonian, which expands the results of refs. [22, 70, 71].

The remainder of the chapter is organized as follows. In section 2.1, I characterize the symmetry operations defined in chapter 1 as the invariance of the Hamiltonian with respect to the action of eight linear or antilinear superoperators. In section 2.2, I discuss the physical consequences of the symmetries in the pole structure of the scattering matrix eigenvalues. Four symmetries are shown to lead to complex poles corresponding to real energies or conjugate (energy) pairs. This result generalizes what was found in refs. [22, 70, 71]. In section 2.3, I exemplify the general results with separable potentials exhibiting parity-pseudohermiticity and time-reversal symmetry. These are the two non-trivial symmetries of the four which have complex-conjugate pairs of eigenvalues (in the sense that the other two, hermiticity and PT-symmetry, are already well discussed). In section 2.4, I discuss and summarize the results.

TABLE 2.1: Symmetries of the Hamiltonian with respect to the commutativity or pseudohermiticity of H with the elements of \mathbf{K}_4 (column 2) in terms of the action of superoperators \mathcal{L} on the potential V in coordinate (Column 4) or momentum (Column 6) representation. This table follows the same code convention with roman numbers for the symmetries as chapter 1 and can be seen as an extension of table 1.1 incorporating the superoperator formalism

(1) Code	(2) Symmetry	(3) $\langle x V y\rangle$	(4) $\mathcal{L}(\text{coord})$	(5) $\langle p V p'\rangle$	(6) $\mathcal{L}(\text{momentum})$	(7) $\langle p S p'\rangle$	(8) T^l	(9) T^r	(10) R^l	(11) R^r
I	$1H = H1$	$\langle x V y\rangle$	1	$\langle p V p'\rangle$	1	$\langle p S p'\rangle$	T^l	T^r	R^l	R^r
II	$1H = H^\dagger 1$	$\langle y V x\rangle^*$	$\mathcal{T}\mathcal{C}$	$\langle p' V p\rangle^*$	$\mathcal{T}'\mathcal{C}$	$\langle p \widehat{S} p'\rangle$	\widehat{T}^l	\widehat{T}^r	\widehat{R}^l	\widehat{R}^r
III	$\Pi H = H\Pi$	$\langle -x V -y\rangle$	\mathcal{I}	$\langle -p V -p'\rangle$	\mathcal{I}'	$\langle -p S -p'\rangle$	T^r	T^l	R^r	R^l
IV	$\Pi H = H^\dagger \Pi$	$\langle -y V -x\rangle^*$	$\mathcal{C}\mathcal{T}\mathcal{I}$	$\langle -p' V -p\rangle^*$	$\mathcal{C}'\mathcal{T}'\mathcal{I}'$	$\langle -p \widehat{S} -p'\rangle$	\widehat{T}^r	\widehat{T}^l	\widehat{R}^r	\widehat{R}^l
V	$\Theta H = H\Theta$	$\langle x V y\rangle^*$	\mathcal{C}	$\langle -p V -p'\rangle^*$	$\mathcal{I}\mathcal{C}'$	$\langle -p' \widehat{S} -p\rangle$	\widehat{T}^r	\widehat{T}^l	\widehat{R}^r	\widehat{R}^l
VI	$\Theta H = H^\dagger \Theta$	$\langle y V x\rangle$	\mathcal{T}	$\langle -p' V -p\rangle$	$\mathcal{I}'\mathcal{T}'$	$\langle -p' S -p\rangle$	T^r	T^l	R^r	R^l
VII	$\Theta\Pi H = H\Theta\Pi$	$\langle -x V -y\rangle^*$	$\mathcal{I}\mathcal{C}$	$\langle p V p'\rangle^*$	\mathcal{C}'	$\langle p' \widehat{S} p\rangle$	\widehat{T}^l	\widehat{T}^r	\widehat{R}^l	\widehat{R}^r
VIII	$\Theta\Pi H = H^\dagger \Theta\Pi$	$\langle -y V -x\rangle$	$\mathcal{I}\mathcal{T}$	$\langle p' V p\rangle$	\mathcal{T}'	$\langle p' S p\rangle$	T^l	T^r	R^l	R^r

2.1 Superoperator formalism

The eight symmetries discussed in chapter 1, which are listed again in Table 2.1 may also be regarded as the invariance of the Hamiltonian with respect to transformations represented by superoperators \mathcal{L} [14] defined by

$$\mathcal{L}(H) = \begin{cases} A^\dagger H A & \text{I, III, V, VII} \\ A^\dagger H^\dagger A & \text{II, IV, VI, VIII} \end{cases}. \quad (2.1)$$

This definition of the superoperator action is independent of the representation we use, but its realization in coordinates or momenta representation in terms of the operations of complex conjugation \mathcal{C} , transposition \mathcal{T} , and inversion \mathcal{I} (sign reversal of momentum or position), is different. In coordinate representation, these superoperators take the following forms (see column 3 in Table 2.1),

$$\begin{aligned} 1H &= \iint |x\rangle\langle x|H|y\rangle\langle y|dxdy, \\ \mathcal{T}(H) &= \iint |x\rangle\langle y|H|x\rangle\langle y|dxdy, \\ \mathcal{C}(H) &= \iint |x\rangle\langle x|H|y\rangle^*\langle y|dxdy, \\ \mathcal{I}(H) &= \iint |x\rangle\langle -x|H| - y\rangle\langle y|dxdy, \end{aligned} \quad (2.2)$$

while in momentum representation, these superoperators are

$$\begin{aligned} 1H &= \iint |p\rangle\langle p|H|q\rangle\langle q|dpdq, \\ \mathcal{T}'(H) &= \iint |p\rangle\langle q|H|p\rangle\langle q|dpdq, \\ \mathcal{C}'(H) &= \iint |p\rangle\langle p|H|q\rangle^*\langle q|dpdq, \\ \mathcal{I}'(H) &= \iint |p\rangle\langle -p|H| - q\rangle\langle q|dpdq. \end{aligned} \quad (2.3)$$

Adopting the trace inner product for linear operators F and G

$$\langle\langle F|G\rangle\rangle = \text{tr}(F^\dagger G) \quad (2.4)$$

we can show that all superoperators (also the primmed ones) and their products \mathcal{L} are either unitary (for $\mathcal{L} = 1, \mathcal{T}, \mathcal{I}, \mathcal{T}\mathcal{I}$), or antiunitary (for $\mathcal{L} = \mathcal{C}, \mathcal{CT}, \mathcal{CI}, \mathcal{CTI}$),

with respect to the inner product as defined by

$$\langle\langle \mathcal{L}F|\mathcal{L}G\rangle\rangle = \langle\langle F|G\rangle\rangle \quad (\mathcal{L} \text{ unitary}), \quad (2.5)$$

$$\langle\langle \mathcal{L}F|\mathcal{L}G\rangle\rangle = \langle\langle F|G\rangle\rangle^* \quad (\mathcal{L} \text{ antiunitary}). \quad (2.6)$$

They all satisfy $\mathcal{L}\mathcal{L}^\dagger = \mathcal{L}^\dagger\mathcal{L} = 1$ where the adjoints are defined differently for linear or antilinear superoperators,

$$\langle\langle F|\mathcal{L}^\dagger G\rangle\rangle = \langle\langle \mathcal{L}F|G\rangle\rangle \quad (\mathcal{L} \text{ unitary}), \quad (2.7)$$

$$\langle\langle F|\mathcal{L}^\dagger G\rangle\rangle = \langle\langle \mathcal{L}F|G\rangle\rangle^* \quad (\mathcal{L} \text{ antiunitary}). \quad (2.8)$$

Moreover the eight superoperators satisfy $\mathcal{L}^\dagger = \mathcal{L}$.

The set $\{1, \mathcal{I}, \mathcal{T}, \mathcal{C}, \mathcal{CT}, \mathcal{TC}, \mathcal{TI}, \mathcal{IC}, \mathcal{CTI}\}$ (and the primmed ones) forms the elementary Abelian group $E8$ [72]. This is a homocyclic group, namely, the direct product of isomorphic cyclic groups of order 2 with generators $\mathcal{C}, \mathcal{T}, \mathcal{I}$. Only for the subgroup $\{1, \mathcal{I}, \mathcal{CT}, \mathcal{CTI}\}$ the superoperators have the same representation-independent form in terms of complex conjugation, transposition, and inversion in momentum and position bases.

A direct application of the superoperator framework is the generalization of Wigner's formulation of symmetries [59]. He associated symmetry transformations to unitary or antiunitary operators preserving the (Hilbert space) inner product, namely the “transition probabilities” $|\langle A\psi, A\phi\rangle|^2 = |\langle\psi, \phi\rangle|^2$. For general states described by density operators ρ_1, ρ_2 , transition probabilities are computed as $\langle\langle \rho_1|\rho_2\rangle\rangle$ and the transformations described by the unitary or antiunitary superoperators preserve the transition probability. Hamiltonian symmetries are, within the conventional Wigner scheme, the symmetry transformations that leave the Hamiltonian invariant ($A^\dagger H A = H$, so that A and H commute). Here the Hamiltonian symmetry is more broadly defined as the invariance $\mathcal{L}H = H$, which includes transformations beyond the conventional scheme.

2.2 S-matrix pole structure

In refs. [22, 70, 71], Mostafazadeh derived the sufficient and necessary conditions of diagonalizable Hamiltonians with a discrete spectrum for having a spectrum made of real eigenvalues and complex-conjugate pairs of eigenvalues. The

condition was that the Hamiltonian had to be A -pseudohermitian with respect to a Hermitian linear operator A or commute with a Hermitian antilinear operator B . In fact, the two conditions are equivalent [71]: if a Hamiltonian is A -pseudohermitian one can find a Hermitian antilinear B that commutes with H and viceversa. In this section I generalize the results in [22, 70, 71] to scattering Hamiltonians. I show, for the symmetry operators in the Klein 4-group, that the poles of the S -matrix have the same structure as the eigenvalues of the discrete spectrum, as described in [22, 70, 71], when the Hamiltonian satisfies symmetries V and VII of table 2.1, *i.e.*, eq. (1.26) for A antiunitary ($A = \Theta, \Pi\Theta$), or symmetries II and IV of table 2.1, *i.e.*, eq. (1.27) for A unitary ($A = 1, \Pi$).

In section 1.1 we introduced the scattering matrix (S -matrix) formalism, which was used to derive the results of chapter 1 regarding the scattering coefficients. It was possible to decompose the S -matrix into the on-the-energy-shell matrices \mathbf{S} for real and positive momentum in terms of transmission and reflection amplitudes for right and left incidence, see eq. (1.10). The \mathbf{S} matrix contains the scattering amplitudes for incoming wave packets with well defined momentum being scattered into states with the same kinetic energy and reflected and transmitted components. The on-shell scattering matrix \mathbf{S} allowed us to obtain the generalized unitary relations (1.16) in terms of the scattering amplitudes (1.19). For negative p the matrix elements of \mathbf{S} give the amplitudes of scattering states with a pure outgoing plane wave towards the right or the left. Moreover we assume, as it is customary, that the amplitudes may be continued analytically beyond the real axis. The existence of a continuation on the complex plane domain depends on decay properties of the potentials and may be checked for each potential. The analytical continuation is indeed possible for the model potentials of the following section.

We will look for the poles of the S -matrix in the eigenvalues of its on-shell decomposition \mathbf{S} . The eigenvalues of \mathbf{S} can be calculated from the transmission and reflection amplitudes as

$$S_j = \frac{(T^l + T^r) + (-1)^j[(T^l - T^r)^2 + 4R^l R^r]^{1/2}}{2} \quad (2.9)$$

for $j = 1, 2$, and of course there is a similar expression for \widehat{S}_j (The scattering matrix for the adjoint Hamiltonian) with hatted amplitudes. In general they satisfy the

relations [3],

$$S_j(p) = \widehat{S}_j^*(-p^*) , \quad (2.10)$$

and

$$\widehat{S}_j^*(p^*)S_j(p) = 1 . \quad (2.11)$$

Combining eqs. (2.10) and (2.11) gives

$$S_j(p) = S_j^{-1}(-p) . \quad (2.12)$$

Equation (2.12) is remarkable since it reveals the presence of a pole (zero) at $-p$ if there is a zero (pole) at p . If the following relations are fulfilled,

$$T^{r,l}(p) = \widehat{T}^{r,l}(p) \text{ or } T^{r,l}(p) = \widehat{T}^{l,r}(p), \quad (2.13)$$

$$R^{r,l}(p) = \widehat{R}^{r,l}(p) \text{ or } R^{r,l}(p) = \widehat{R}^{l,r}(p), \quad (2.14)$$

then

$$S_j(p) = \widehat{S}_j(p), \quad (2.15)$$

which together with eq. (2.10) gives

$$S_j(p) = S_j^*(-p^*). \quad (2.16)$$

In plain language, eq. (2.16) tells that if eqs. (2.13) and (2.14) are satisfied, the poles and zeros of S_j must be symmetrically distributed with respect to the imaginary axis of the momentum complex plane. Combined with eq. (2.12) this also means that each pole has a symmetrical zero with respect to the real axis. This symmetrical distribution of poles and zeros is the same as in the Hermitian case (see fig. 2.1), the only difference being the possibility of finding pairs of symmetrical poles in the upper complex plane when $H \neq H^\dagger$. They represent normalizable “bound states with complex energies”. When they are not present, the discrete spectrum becomes purely real.

According to Table 2.1, eqs. (2.13) and (2.14) are fulfilled for symmetries II (hermiticity), VII (PT-symmetry), IV (parity pseudohermiticity), and V (time-reversal invariance). Thus, Hamiltonians having these symmetries have their S -matrix poles symmetrically distributed about the imaginary axis. For local potentials the last two symmetries coalesce with the first two well-known cases [13], namely, IV becomes equivalent to PT-symmetry, and V becomes equivalent

to hermiticity. For non-local potentials, though, these symmetries correspond to genuinely distinct properties. In the following section we shall demonstrate this fact with potentials that are either purely parity-pseudohermitian (and not PT-symmetrical), or time-reversal invariant but not Hermitian.

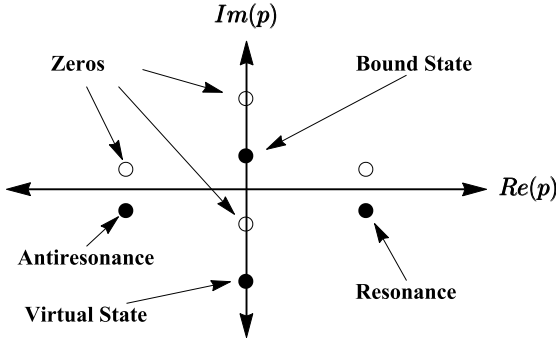


FIGURE 2.1: Example of configuration of poles (filled circles) and zeros (empty circles) of the S -matrix eigenvalues in the complex momentum plane for Hermitian Hamiltonians. Poles in the upper half plane ($\text{Im}(p) > 0$) correspond to bound eigenstates of the Hamiltonian, i.e. localized states with negative energy. Poles in the lower half plane correspond to virtual states ($\text{Re}(p) = 0$), resonances ($\text{Re}(p) > 0$) and antiresonances ($\text{Re}(p) < 0$). The singularities with negative imaginary part correspond to states that do not belong to the Hilbert space since they are not normalizable. However, they can produce observable effects in the scattering amplitudes, in particular when they approach the real axis. The pole structure of symmetries IV, V, and VII, see Table 2.1, is similar, but pole pairs are also possible in the upper half-plane.

2.3 Separable Potentials

In order to illustrate and test the theoretical concepts that we have discussed, in particular the symmetrical configuration of poles with respect to the imaginary axis in the complex momentum plane for certain Hamiltonian symmetries, we will use some solvable toy models consisting on rank-one separable potentials. Separable potentials are quite useful models as a solvable approximation to realistic ones, in particular in nuclear, atomic, and molecular physics [73]. Often they lead to explicit expressions for wave functions or scattering amplitudes, so they are used to test concepts and new methods. They are also instrumental in learning about different dynamical phenomena (for example transient effects, short-time and long-time behavior, or anomalous decay laws) and their relation to complex-plane singularities [74–77]. Their simplest version takes the form $|\chi\rangle V_0 \langle\chi|$ for some χ . In particular, with a complex V_0 , they have been used to examine anomalous

(negative) time delays caused by crossing of zeroes of the S -matrix eigenvalues or S -matrix elements across the momentum real axis [78].

In this work we consider the simple structure $V = V_0 |\phi\rangle\langle\chi|$, with V_0 (potential strength) real, and conveniently chosen normalised states $|\phi\rangle$, $|\chi\rangle$. The aim of this section is to demonstrate the formal results of the previous section without attempting to simulate any specific systems, but we note that separable, non-Hermitian potentials are instrumental to model nuclear reactions, in particular by increasing the rank (number of separable terms) [79]. Separable non-Hermitian potentials also provide solvable approximations to non-local non-Hermitian potentials that arise naturally in quantum optics to describe the interaction of a ground state atom with a laser beam [80].

I proceed to look for the poles of the S matrix in the following way. Since the scattering amplitudes in S are simply related to matrix elements of $T_{op}(z)$ (eq. (1.7)) in momentum representation, see eq. (1.9), the singularities in the scattering amplitudes and the eigenvalues of S will come from the singularities of $T_{op}(z)$ [75]. For a separable potential, the transition operator T_{op} can be written (see Appendix A.1) as

$$T_{op} = \frac{V_0}{1 - V_0 Q_0(E)} |\phi\rangle\langle\chi|, \quad (2.17)$$

where $Q_0(E) = \langle\chi| (E - H_0)^{-1} |\phi\rangle$ and $H_0 = p^2/(2m)$. Therefore, the singularities (poles) of S are found by solving

$$Q_0(E)V_0 = 1, \quad (2.18)$$

Once $Q_0(E)$ is calculated, the transmission and reflection amplitudes can be found from (1.9) using the momentum representation of $|\phi\rangle$ and $|\chi\rangle$ (see Appendix A.2).

In the following subsections I will build a Hamiltonian with symmetry V (time reversal) and another one with symmetry IV (parity pseudohermicity) and illustrate the symmetries of the S matrix poles in momentum complex plane.

2.3.1 Time-reversal symmetric potential

We start with an example of a separable potential which only satisfies symmetry V (apart from the trivial symmetry I). The normalised vector $|\chi\rangle$, is given in

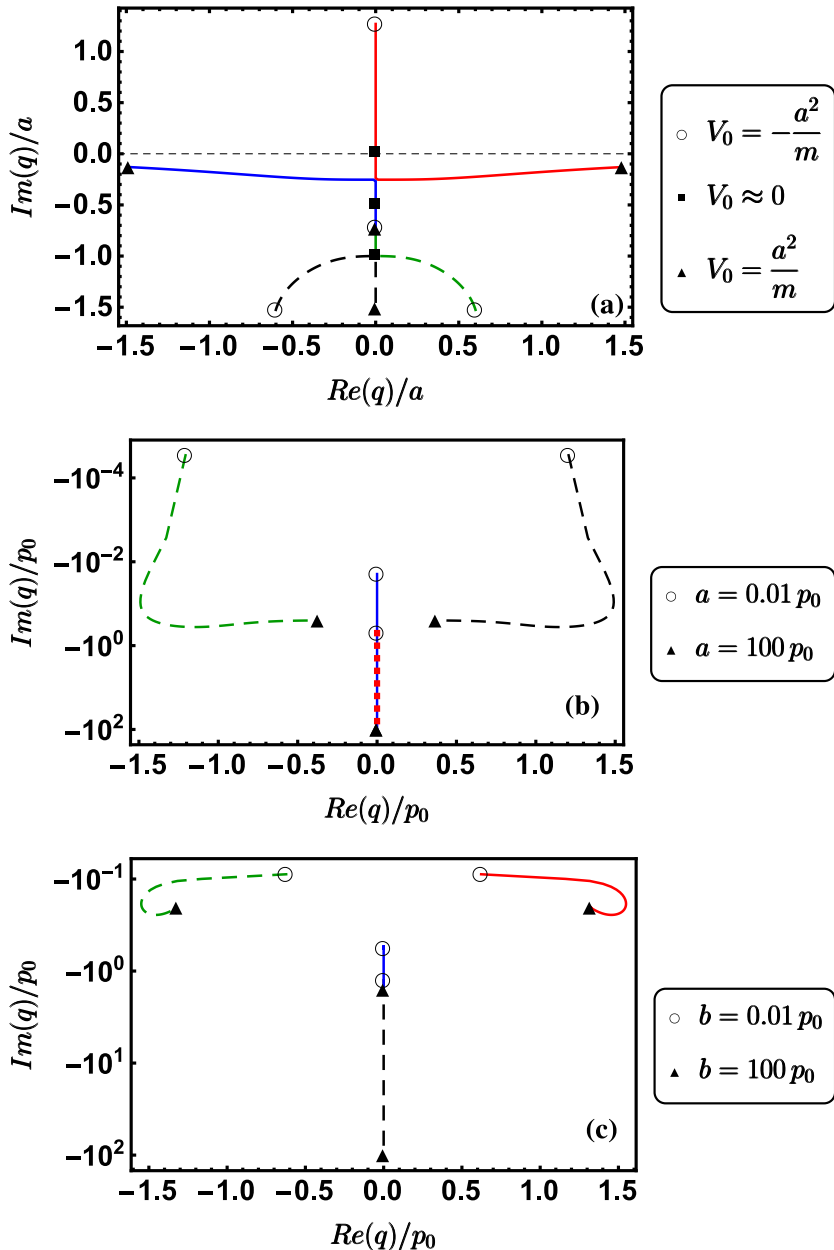


FIGURE 2.2: Poles and pole trajectories of time-reversal symmetric potential (2.21) for (a) varying V_0 with $a = 2b$; (b) varying a with $b = 0.5 p_0$, $V_0 > 0$; and (c) varying b with $a = p_0$, $V_0 > 0$. At pole collisions we connect each of the incoming trajectories with a different emerging trajectory but the choice of outgoing branch is arbitrary since the two colliding poles lose their identity.

position and momentum representation as

$$\begin{aligned} \langle x|\chi\rangle &= \sqrt{\frac{a}{\hbar}} e^{-a|x|/\hbar}, \\ \langle p|\chi\rangle &= \sqrt{\frac{2a^3}{\pi}} \frac{1}{p^2 + a^2}. \end{aligned} \quad (2.19)$$

We choose $|\phi\rangle$ similarly as

$$\begin{aligned}\langle x|\phi\rangle &= \sqrt{\frac{2ab}{\hbar(a+b)}} \begin{cases} e^{-bx/\hbar} & x > 0, \\ e^{ax/\hbar} & x < 0, \end{cases} \\ \langle p|\phi\rangle &= \sqrt{\frac{ab}{\pi(a+b)}} \frac{a+b}{(p+ia)(p-ib)}. \end{aligned}\quad (2.20)$$

The real and positive parameters \hbar/a and \hbar/b determine the width of the potential functions in coordinate representation. b is chosen different from a to introduce a right/left asymmetry in $\langle x|\phi\rangle$. In coordinate representation the potential is given as

$$\langle x|V|y\rangle = V_0 \sqrt{\frac{2ba^2}{\hbar^2(a+b)}} \begin{cases} e^{-(a|y|+bx)/\hbar} & x > 0, \\ e^{a(x-|y|)/\hbar} & x < 0. \end{cases}\quad (2.21)$$

Clearly the potential is always even in y and in the limiting case where $a = b$, it is also even in x . For $a = b$, the potential will satisfy parity symmetry (III) and also PT symmetry (VII), without asymmetric transmission or reflection.

We define first a complex momentum $q = \sqrt{2mE}$ (for complex E) with positive imaginary part. To calculate $Q_0(q)$ explicitly we use a closure relation in momentum representation, and complex contour integration around the poles at ia , q and ib . The result is then analytically continued to the whole q -plane,

$$Q_0(q)/m = -\frac{i\sqrt{2b}[2a(a+b)^2 - q^2(3a+b) - iq(2a+b)(3a+b)]}{q(a+b)^{3/2}(a-iq)^2(b-iq)},\quad (2.22)$$

with which we may calculate the transmission and reflection amplitudes. The four roots of eq. (2.18) are the core poles of \mathbf{S} .

Using m , V_0 and \hbar we define the length and momentum scales $L_0 = \hbar/\sqrt{mV_0}$ and $p_0 = \sqrt{mV_0}$. In fig. 2.2(a), we can see the trajectory of the \mathbf{S} -matrix core poles (zeros of $1 - V_0 Q_0(q)$) for varying V_0 . Notice a bound state for $V_0 < 0$ and collisions of the eigenvalue pairs around $V_0 = 0$. In figs. 2.2(b) and 2.2(c), where V_0 is positive and a or b are varied, there are two virtual states and one resonance/anti-resonance pair. In all cases the symmetry of the poles about the imaginary axis which corresponds to real energies or complex-conjugate pairs of energies, is evident. For larger values of the a or b parameters (not shown) the pair collides so that all poles end up as virtual states.

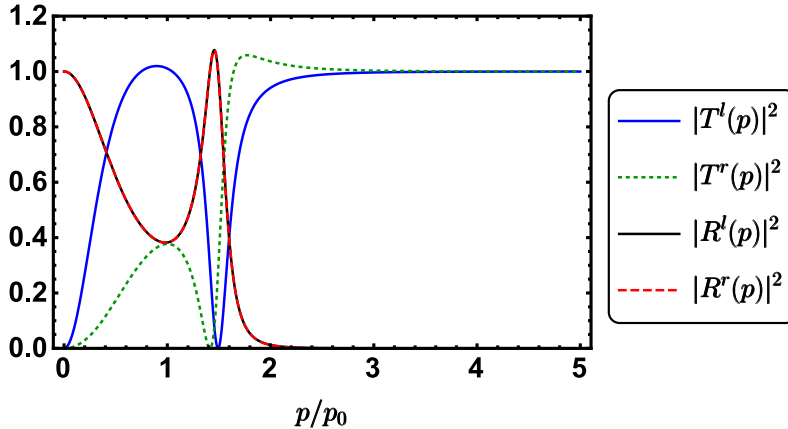


FIGURE 2.3: Transmission and reflection coefficients of the time-reversal symmetric potential (symmetry V) (2.21) with $a = p_0$, $b = 0.5 p_0$ and $V_0 > 0$.

Figure 2.3 depicts the associated transmission and reflection coefficients (square moduli of the amplitudes) as functions of the momentum p . $|R^l(p)| = |R^r(p)|$ for all p due to symmetry V, see column (11) of table 1.1. The coefficients can be greater than one in contrast to the Hermitian case.

2.3.2 Parity pseudohermitian potential

As a second example we will consider a separable potential which only fulfills symmetry IV. The normalised vector $|\chi\rangle$ in position and momentum representation is

$$\begin{aligned} \langle x|\chi\rangle &= \sqrt{\frac{a}{\hbar}} \begin{cases} e^{-(a+ib)x/\hbar} & x > 0, \\ e^{ax/\hbar} & x < 0, \end{cases} \\ \langle p|\chi\rangle &= \sqrt{\frac{a}{2\pi}} \frac{2a+ib}{(p+ia)(p+b-ia)}, \end{aligned} \quad (2.23)$$

where $a > 0$ and b is real. We choose $|\phi\rangle$ as

$$\begin{aligned} \langle x|\phi\rangle &= \sqrt{\frac{a}{\hbar}} \begin{cases} e^{-ax/\hbar} & x > 0, \\ e^{(a+ib)x/\hbar} & x < 0, \end{cases} \\ \langle p|\phi\rangle &= \sqrt{\frac{a}{2\pi}} \frac{2a+ib}{(p-ia)(p-b+ia)}, \end{aligned} \quad (2.24)$$

where \hbar/a gives, as before, the width in coordinate representation. The potential functions in coordinate representation become asymmetrical because of the imaginary terms ib in the exponent added only on one side. This term leads to

oscillations in real and imaginary parts. In momentum representation b appears as a real shift in the position of one of the poles. In coordinate representation the potential is

$$\langle x|V|y\rangle = \frac{aV_0}{\hbar} \begin{cases} e^{-[a(x+y)-iby]/\hbar}, & x > 0, y > 0 \\ e^{a(y-x)/\hbar}, & x > 0, y < 0 \\ e^{[a(x-y)+ib(x+y)]/\hbar}, & x < 0, y > 0 \\ e^{[a(x+y)+ibx]/\hbar}, & x < 0, y < 0 \end{cases}. \quad (2.25)$$

The case $b = 0$ implies that the potential is real and hence satisfies time-reversal symmetry (V) with equal reflection amplitudes (as in the previous case), and also symmetry VIII.

By calculating Q_0 again explicitly using complex contour integration around the poles at $-q$, $-b - ia$ and $b - ia$, we get that

$$Q_0(q)/m = \frac{8a^2q^3 - 4a^2q(10a^2 + b^2) - ia(4a^2 + b^2)^2 + 32ia^3q^2}{q(4a^2 + b^2)(a - iq)^2[b^2 + (a - iq)^2]}.$$

Equation (2.18) has five roots in this case constituting core poles of the S-matrix elements.

Figure 2.4 depicts the trajectories of these poles for varying a , b or V_0 . As for the previous potential, the poles are symmetric with respect to the imaginary axis. In fig. 2.4(a) there is a single bound state for $V_0 < 0$ while for positive values there are a resonance/antiresonance pair and a pair of virtual states. There are collisions of eigenvalues for values of V_0 close to 0. In fig. 2.4(b) two complex-conjugate (bound) eigenvalues cross the real axis and become a resonance/antiresonance pair. At the exact point where the eigenvalues are on the real axis, the scattering amplitudes diverge, however the eigenvalues of the S matrix do not, since divergences of the left and right amplitudes cancel each other. For $a \approx 4.55 p_0$ a resonance/antiresonance pair collides and becomes a pair of virtual states. In fig. 2.4(c) another crossing of the real axis takes place, but in this case when decreasing b .

Figure 2.5 depicts the associated transmission and reflection coefficients as functions of the momentum p . The eigenvalues are not always equal since parity pseudohermicity does not imply any strict restriction to them [13]. For large momenta, i.e. $p \gg \sqrt{2}p_0$, the potential is transparent giving $T^l, T^r \approx 1$. For $p \approx 1.5 p_0$ the right incidence transmission has a pronounced peak. Comparing with 2.4(c), we

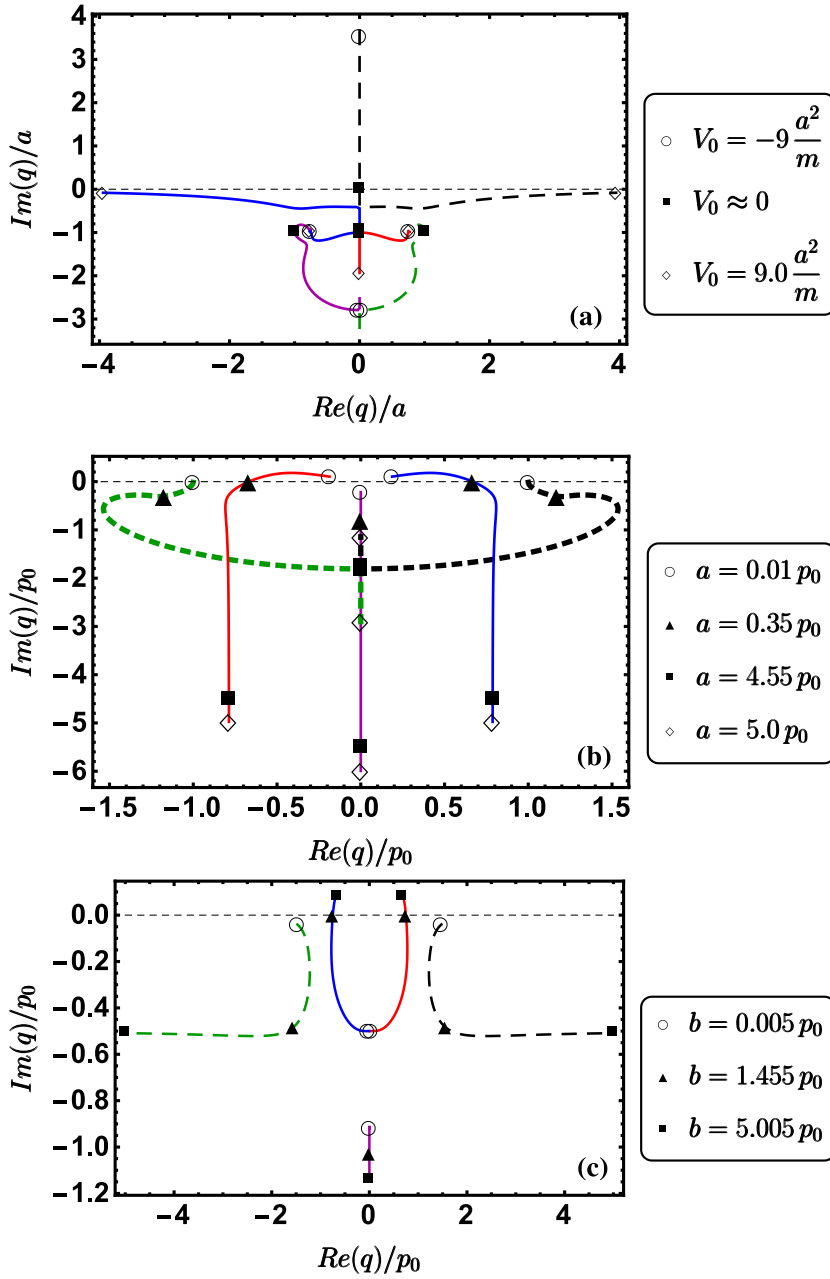


FIGURE 2.4: Poles and pole trajectories for the parity pseudohermitian potential (2.25) (a) varying V_0 with $a = b$; (b) varying a with $b = p_0, V_0 > 0$; (c) varying b with $a = 0.5 p_0, V_0 > 0$.

notice that the values of the potential parameters and the momentum are close to the ones for which the real axis crossing takes place. Around $p = 0.6 p_0$ the potential acts as a \mathcal{T}/\mathcal{R} device or one-way-barrier (see table 1.5).

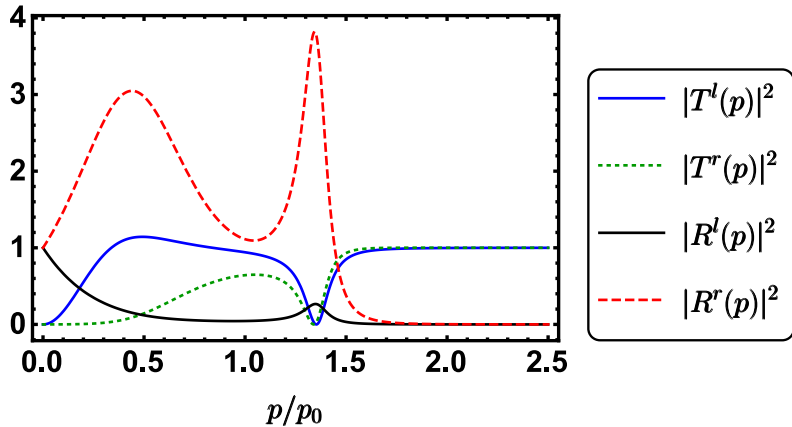


FIGURE 2.5: Transmission and reflection coefficients for $a = b = 0.5 p_0$ and $V_0 > 0$.

2.4 Discussion

In this chapter I have studied some aspects of the scattering of a structureless particle in one dimension by generally non-local and non-Hermitian potentials.

Conditions that were found for discrete Hamiltonians to imply conjugate pairs of discrete eigenenergies (pseudohermiticity with respect to a linear operator or commutativity of H with an antilinear operator [22, 70, 71]) can in fact be extended to scattering Hamiltonians in the continuum, implying symmetry relations not just for bound-state eigenvalues but also for complex poles of the S -matrix. Specifically the poles of S matrix eigenvalues are symmetrically located with respect to the imaginary axis, also in the lower momentum plane, so that resonances and antiresonance energies are conjugate pairs as well. In terms of the eight possible Hamiltonian symmetries associated with Klein's group of A operators (unity, parity, time reversal and PT) and their commutation or pseudohermiticity with H , the symmetrical disposition of the poles applies to four of them, which includes hermiticity and PT-symmetry. Potential models and pole motions are provided for the two other non trivial symmetries: time-reversal symmetry and parity pseudohermiticity.

Chapter 3

Quantum-Optical implementation of non-Hermitian potentials for asymmetric scattering

In chapters 1 and 2, non-local potentials for asymmetric scattering were constructed as mathematical models but no physical implementation was discussed. In this chapter a feasible quantum-optical implementation of non-Hermitian, non-local, non-PT potentials is put forward to implement different scattering asymmetries, including transmission asymmetries. Using Feshbach's projection technique it is found that the effective potentials for a ground-state atom crossing a laser beam in a region of space are generically non-local and non-Hermitian. Shaping the spatial-dependence of the, generally complex, Rabi frequency, and selecting a specific laser detuning allows to produce different potential symmetries and asymmetric scattering effects, including asymmetric transmission.

The rest of this chapter is organized as follows. In Sec. 3.1, I shall explain how to generate different NH symmetries in a quantum-optical setting of an atom impinging on a laser illuminated region. In Sec. 3.2, I provide specific examples of devices (constructed using numerical optimisation) with different asymmetric scattering responses. Realistic experimental parameters are also examined. In Sec. 3.3, the asymmetric behavior is explained with a classical approximation of the motion and the non-commutativity of rotations on the Bloch sphere, which gives good estimates for the potential parameters. Finally, in Sec. 3.4, I summarize the main findings in the chapter.

TABLE 3.1: Conditions leading to specific symmetries in the potential (3.4). A given symmetry also implies others, see the last column.

Symmetry	Conditions	Implies
(I) $1H = H1$	none	-
(II) $1H = H^\dagger 1$	$q = -q^*$ (i.e. $\text{Re } q = 0$)	I
(III) $\Pi H = H\Pi$	$\Omega(x) = e^{i\phi}\Omega(-x)$	I
(IV) $\Pi H = H^\dagger \Pi$	$q = -q^* \& \Omega(x) = e^{i\phi}\Omega(-x)$	III, II, I
(V) $\Theta H = H\Theta$	$q = -q^* \& \Omega(x) = e^{i\phi}\Omega(x)^*$	VI, II, I
(VI) $\Theta H = H^\dagger \Theta$	$\Omega(x) = e^{i\phi}\Omega(x)^*$	I
(VII) $\Theta\Pi H = H\Theta\Pi$	$q = -q^* \& \Omega(x) = e^{i\phi}\Omega(-x)^*$	VIII, II, I
(VIII) $\Theta\Pi H = H^\dagger \Theta\Pi$	$\Omega(x) = e^{i\phi}\Omega(-x)^*$	I

3.1 Effective non-local potential for the ground state of a two-level atom

The key task is to physically realize some of the potential and asymmetric device types described in chapter 1, which are again summarized in table 3.2. I start with a two-level atom with ground level $|1\rangle$ and excited state $|2\rangle$ impinging onto a laser illuminated region. For a full account of the model and further references see [81]. The motion is assumed to be one dimensional, either because the atom is confined in a waveguide or because the direction x is uncoupled to the others. I only account explicitly for atoms before the first spontaneous emission in the wave function [82–84]. If the excited atom emits a photon, it disappears from the coherent wave function ensemble. I assume that no resetting into the ground state occurs. The physical mechanism may be an irreversible decay into a third level [85], or atom ejection from the waveguide or the privileged 1D direction due to random recoil [86]. The state $\Phi_k = (\phi_k^{(1)}, \phi_k^{(2)})^\top$ for the atom before the first spontaneous emission impinging with wave number k in a laser adapted interaction picture, obeys, after applying the rotating-wave approximation, an effective stationary Schrödinger equation with a time-independent Hamiltonian [80, 81] $\mathcal{H}\Phi_k(x) = E\Phi_k(x)$, where

$$\mathcal{H} = H_0\mathbf{1} + \mathcal{V} = \frac{1}{2m} \begin{pmatrix} p^2 & 0 \\ 0 & p^2 \end{pmatrix} + \mathcal{V}(x), \quad (3.1)$$

$$\mathcal{V}(x) = \frac{\hbar}{2} \begin{pmatrix} 0 & \Omega(x) \\ \Omega(x)^* & -(2\Delta + i\gamma) \end{pmatrix}. \quad (3.2)$$

I assume perpendicular incidence of the atom on the laser sheet for simplicity. Here $E = \hbar^2 k^2 / 2m$ is the energy, and $\Omega(x)$ is the position-dependent, on-resonance Rabi

TABLE 3.2: Device types for transmission and/or reflection asymmetry in the first row (see Sec. 1.4 for nomenclature). The second row gives the corresponding symmetries that allow each device.

$\mathcal{T}\mathcal{R}/\mathcal{A}$	\mathcal{T}/\mathcal{R}	\mathcal{T}/\mathcal{A}	$\mathcal{T}\mathcal{R}/\mathcal{R}$	\mathcal{R}/\mathcal{A}	$\mathcal{T}\mathcal{R}/\mathcal{T}$
I	I	I, VIII	I, VIII	I, VI	I, IV, VI, VII

frequency, where real and imaginary parts may be controlled independently using two laser field quadratures [87]; γ is the inverse of the lifetime of the excited state; $\Delta = \omega_L - \omega_{12}$ is the detuning (laser angular frequency minus the atomic transition angular frequency ω_{12}); $p = -i\hbar\partial/\partial x$ is the momentum operator; and $\mathbf{1} = |1\rangle\langle 1| + |2\rangle\langle 2|$ is the unit operator for the internal-state space. Complementary projectors $P = |1\rangle\langle 1|$ and $Q = |2\rangle\langle 2|$ are defined to select ground and excited state components. Using the Feshbach partitioning technique [5, 88, 89], I find for the ground state amplitude $\phi_k^{(1)}$ the equation

$$E\phi_k^{(1)}(x) = H_0\phi_k^{(1)}(x) + \int dy \langle x, 1 | \mathcal{W}(E) | y, 1 \rangle \phi_k^{(1)}(y), \quad (3.3)$$

where $\mathcal{W}(E) = P\mathcal{V}P + P\mathcal{V}Q(E + i0 - Q\mathcal{H}Q)^{-1}Q\mathcal{V}P$, is generically non-local and energy-dependent. Specifically, I have now achieved a physical realization of an effective (in general) non-local, non-Hermitian potential whose kernel has the form

$$V(x, y) = \langle x, 1 | \mathcal{W}(E) | y, 1 \rangle = \frac{m}{4} \frac{e^{i|x-y|q}}{iq} \Omega(x)\Omega(y)^*, \quad (3.4)$$

where $q = \frac{\sqrt{2mE}}{\hbar}(1 + \mu)^{1/2}$, $\text{Im } q \geq 0$, and $\mu = \frac{2\Delta + i\gamma}{2E/\hbar}$. eq. (3.4) is worked out in momentum representation to do the integral using the residue theorem. This is a generalized, non-local version of the effective potentials known for the ground state [85, 90], which are found from eq. (3.4) in the large μ limit [80]. The reflection and transmission amplitudes $R^{r,l}$ and $T^{r,l}$ may be calculated directly using the potential (3.4) or as corresponding amplitudes for transitions from ground state to ground state in the full two-level theory (see Appendix B).

3.1.1 Possible symmetries of the non-local potential

The necessary conditions for the different symmetries of a non-Hermitian and non-local Hamiltonian were worked out in Sec. 1.4. In the second column of table 3.1, those conditions have been particularized for the effective potential of the

2-level atom (3.4). For example, symmetry III (parity) requires that $V(x, y) = V(-x, -y)$ (see table 1.1). Inserting the functional form of the potential from eq. (3.4) into this condition, it results in the requirement $\Omega(x)\Omega(y)^* = \Omega(-x)\Omega(-y)^*$. This is fulfilled if $\Omega(x) = \Omega(-x)e^{i\phi}$ with some arbitrary phase freedom ϕ .

Since $\Omega(x)$ does not depend on q , symmetries IV, V and VII imply that symmetry II is obeyed as well (Hermiticity). Moreover, symmetry III (parity) should be discarded for our purpose since it does not allow for asymmetric transmission or reflection [13]. This leaves us with three interesting symmetries to explore: VI, which allows for asymmetric reflection; VIII which allows for asymmetric transmission; and I, which in principle allows for arbitrary asymmetric responses, except for physical limitations imposed by the two-level model see Appendix B.

As seen from table 3.1, $\text{Re}(q) = 0$ makes the potential Hermitian, so it must be avoided. If $\gamma = 0$, $\mu \in \mathbb{R}$. Hence $\mu + 1 < 0$ gives $\text{Re}(q) = 0$ and $\mu + 1 > 0$ gives $\text{Im}(q) = 0$. $\mu + 1 > 0$ amounts to a condition on the detuning compared to the incident energy, namely $\Delta > -E/\hbar$. In the following I implement potentials with symmetries VIII, VI, and I, with detunings and energies satisfying the condition $\mu + 1 > 0$.

3.2 Design of asymmetric devices

I will now apply this method to physically realize non-local potentials of the form (3.4). I shall work out explicitly a \mathcal{T}/\mathcal{A} device with symmetry VIII, an \mathcal{R}/\mathcal{A} device with symmetry VI, and a “partial”- $\mathcal{T}\mathcal{R}/\mathcal{A}$ device, having 1/2 transmission and reflection coefficients from the left, with symmetry I. The \mathcal{T}/\mathcal{A} and the “partial”- $\mathcal{T}\mathcal{R}/\mathcal{A}$ device have transmission asymmetry so they cannot be built with local or PT -symmetric potentials. Let us motivate the effort with some possible applications, relations and analogies of these devices. \mathcal{T}/\mathcal{A} and \mathcal{R}/\mathcal{A} are, respectively, transmission and reflection filters. They are analogous to half-wave electrical rectifiers that either let the signal from one side “pass” (transmitted) or change its sign (reflected) while suppressing the other half signal. They may play the role of half-rectifiers in atomtronic circuits. A \mathcal{T}/\mathcal{A} device allows us, for example, to empty a region of selected particles, letting them go away while not letting particles in. The “atom diode” devices worked out e.g. in [6, 91–93] were

of type \mathcal{R}/\mathcal{A} . As the mechanism behind them was adiabatic, a broad range of momenta with the desired asymmetry could be achieved. In comparison, the current approach is not necessarily adiabatic so it can be adapted to faster processes.

As for the “partial”- \mathcal{RT}/\mathcal{A} device, it reflects and transmits from one side while absorbing from the other side. In an optical analogy an observer from the left perceives it as a darkish mirror. An observer from the right “sees” the other side because of the allowed transmission but cannot be seen from the left since nothing is transmitted from right to left. Our device is necessarily a “partial” one as there cannot be net probability gain because of the underlying two-level system, and a “full” version with both reflection and transmission coefficients equal to one would need net probability gain.

The three devices are worked out for $\gamma = 0$, a valid approximation for hyperfine transitions. I assume for the Rabi frequencies the forms

$$\begin{aligned}\Omega_{\text{VIII}}(x) &= a[g(x + x_0) + ig(x - x_0)], \\ \Omega_{\text{VI}}(x) &= bg(x + x_0) + cg(x - x_0), \\ \Omega_{\text{I}}(x) &= -ibg(x + x_0) + cg(x - x_0),\end{aligned}\tag{3.5}$$

in terms of smooth, realizable Gaussians $g(x) = \exp[-x^2/w^2]$. I fix $2d$ as an effective finite width of the potential area beyond which the potential is negligible and assumed to vanish. I will express in the following the different length parameters as a multiple of d to keep results general. In addition, I will use as a scaling factor for the velocity $v_d = \hbar/(md)$, and for time $\tau = md^2/\hbar$.

In the following calculations I fix the width of the Gaussians to be $w = \sqrt{2}d/10$. I always first set a target velocity v_0 to achieve the desired asymmetric scattering response. The real parameters a, b, c, x_0 in eq. (3.5), and Δ are then numerically optimized with the GRAPE (Gradient Ascent Pulse Engineering) algorithm [94, 95].

The Rabi frequencies will fulfill the indicated symmetries VIII, VI, and I. $\Omega_{\text{VI}}(x)$ should not be even (i.e. $b \neq c$) to avoid symmetry II. In addition, $\Omega_{\text{I}}(x)$ should not fulfill any other symmetry than I. The corresponding Rabi frequencies $\Omega(x)$ are depicted in figs. 3.1, top row. The scattering coefficients are shown in the bottom row. fig. 3.1 demonstrates that the three potentials satisfy the asymmetric response conditions imposed at the selected velocity and also in a region nearby.

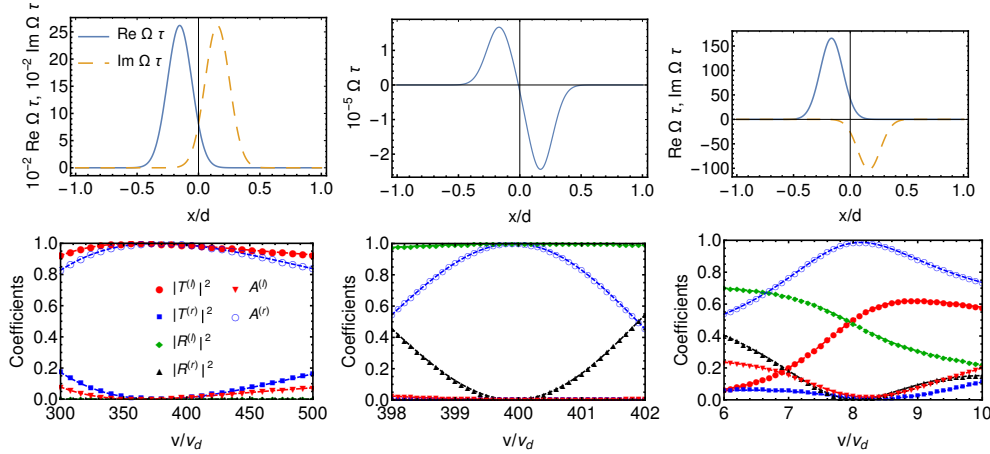


FIGURE 3.1: Left column: \mathcal{T}/\mathcal{A} device with symmetry VIII. Top: $\Omega_{\text{VIII}}(x)$; Bottom: transmission and reflection coefficients. $v_0/v_d = 400$, $a\tau = 2618.19$, $x_0/d = 0.1532$, $\tau\Delta = 1413.01$. Middle column: \mathcal{R}/\mathcal{A} device with symmetry VI. Top: $\Omega_{\text{VI}}(x)$ (it is real); Bottom: transmission and reflection coefficients. $v_0/v_d = 400$, $b\tau = -244516.1$, $c\tau = 167853.9$, $x_0/d = 0.1679$, $\tau\Delta = 193.508$. Right column: “Partial”- \mathcal{TR}/\mathcal{A} device with symmetry I. Top: $\Omega_I(x)$, real (blue, solid line) and imaginary parts (orange, dashed line); Bottom: transmission and reflection coefficients. $v_0/v_d = 8$, $b\tau = 102.6520$, $c\tau = 165.8355$, $x_0/d = 0.1648$, $\tau\Delta = 90.5337$. In all cases $\tau = md^2/\hbar$ and $v_d = \hbar/(md)$.

The “partial”- \mathcal{TR}/\mathcal{A} device fulfills $|T^l|^2 = |R^l|^2 = 1/2$ and full absorption from the right. The potential I use for that device has symmetry I only, i.e., “no symmetry” other than the trivial commutation with the identity. No other potential symmetry would allow this type of device.

The effective non-local potential $V(x, y)$, see eq. (3.4), corresponding to the v/v_d ratios used for the three devices is shown in fig. 3.2. Note that the non-local potential has dimensions energy/length, so we divide the absolute value by a factor $V_0 = \hbar^2/(md^3)$ to plot a dimensionless quantity.

In the parameter optimization I see that increasing the velocities further does not pose a problem for the \mathcal{T}/\mathcal{A} device, it is more challenging for an \mathcal{R}/\mathcal{A} device, and it is quite difficult for the partial- \mathcal{RT}/\mathcal{A} device. The device \mathcal{T}/\mathcal{A} is feasible for an experimental implementation as the ratio v_0/v_d can be easily increased to desired values, for reasonable values of the Rabi frequency and laser waist [96].

Moreover, the velocity width with the desired behavior is much broader for \mathcal{T}/\mathcal{A} . Therefore a \mathcal{T}/\mathcal{A} device is the best candidate for an experimental implementation. As a check of feasibility, let us assume a Beryllium ion. Its hyperfine structure provides a good two-level system for which I can neglect decay (i.e. $\gamma \approx 0$

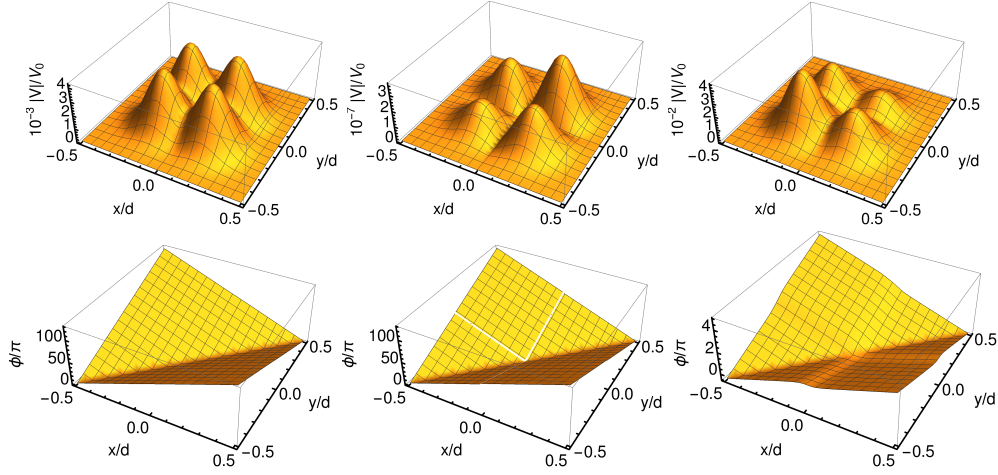


FIGURE 3.2: Non-local potentials $V(x, y)$: absolute value (top), argument (bottom). Left column: Potential for \mathcal{T}/\mathcal{A} device with symmetry VIII. Middle column: Potential for \mathcal{R}/\mathcal{A} device with symmetry VI. Right column: “Partial”- $\mathcal{T}\mathcal{R}/\mathcal{A}$ device with symmetry I. $V_0 = \hbar^2/(md^3)$.

is indeed realistic). $m = 1.49 \times 10^{-26}$ kg and I set a length $d = 10 \mu\text{m}$ compatible with the small laser waists (in this case $1.4 \mu\text{m}$) achieved for individual ion addressing [96]. The scaling factors take the values

$$\begin{aligned} v_d &= 0.67 \text{ mm/s}, \\ \tau &= 1.49 \times 10^{-2} \text{ s}, \end{aligned}$$

which gives $v \approx 27 \text{ cm/s}$ for $v/v_d = 400$, (there is no major obstacle to get devices for higher velocities, in particular the classical approximations in Sec. 3.3 can be used to estimate the values of the parameters) and Rabi frequencies, see fig. 3.1, in the hundreds of kHz range. The relative ion-laser beam velocity could be as well implemented by moving the beam in the laboratory frame.

3.3 Classical approximation for \mathcal{T}/\mathcal{A} device

In a \mathcal{T}/\mathcal{A} device such as the one presented, an incident plane wave from the left ends up as a pure transmitted wave with no reflection or absorption. However, a wave incident from the right is fully absorbed. How can that be? Should not the velocity-reversed motion of the transmitted wave lead to the reversed incident wave? For a more intuitive understanding I may seek help in the underlying two-level model. In the larger space the potential is again local and Hermitian. A simple semiclassical approximation is to assume that the particle moves with

constant speeds $\pm v$ for left ($v > 0$) or right ($-v < 0$) incidence, so that at a given time it is subjected to the 2×2 time-dependent potentials $\mathcal{V}(\pm vt)$. The incidence from the left and right give different time dependences for the potential. The scattering problem then reduces to solving the time-dependent Schrödinger equation for the amplitudes of a two-level atom with time-dependent potential, i.e. to solving the following time-dependent Schrödinger equation ($\gamma = 0$)

$$i\hbar \frac{\partial}{\partial t} \chi_{\pm}(t) = \mathcal{V}(\pm vt) \chi_{\pm}(t), \quad (3.6)$$

with the appropriate boundary conditions $\chi_+(-\infty) = \chi_-(-\infty) = (1 0)$. The solutions for $v/v_d = 400$ are shown in fig. 3.3. In fig. 3.3(a), $\chi_+(t)$ (left incidence) is depicted: the particle ends with high probability in the ground state at the final time. In fig. 3.3(b), $\chi_-(t)$ (right incidence) shows that the ground state population is transferred to the excited state. Projected onto the ground-state level alone, this corresponds to full absorption of the ground state population at the final time.

For an even rougher but also illustrative picture, again in a semiclassical time-dependent framework, I may substitute the smooth Gaussians for $\text{Re}(\Omega)$ and $\text{Im}(\Omega)$ in fig. 3.1 by two simple, contiguous square functions of height $\Omega > 0$ and width $\tilde{w} > 0$. Then, the 2×2 potential at a given time is, in terms of Pauli matrices,

$$\mathcal{V}(x) = \frac{\hbar}{2} \Delta (\sigma_Z - \mathbf{1}) + \frac{\hbar}{2} \begin{cases} \Omega \sigma_X & -\tilde{w} < x < 0 \\ -\Omega \sigma_Y & 0 < x < \tilde{w} \\ 0 & \text{otherwise} \end{cases} \quad (3.7)$$

where $x = \pm vt$ and let $T = 2\tilde{w}/v$.

The time-evolution of this process, $\chi_{\pm}(t)$, up to a phase factor may be regarded as two consecutive rotations $R_j = e^{-i\beta \mathbf{n}_j \cdot \boldsymbol{\sigma}/2}$ ($j = 1, 2$), with $\beta = \frac{T}{2} \sqrt{\Omega^2 + \Delta^2}$, of the two-level state on the Bloch sphere about the axes

$$\mathbf{n}_1 = \frac{1}{\sqrt{\Omega^2 + \Delta^2}} (\Omega, 0, \Delta), \quad (3.8)$$

$$\mathbf{n}_2 = \frac{1}{\sqrt{\Omega^2 + \Delta^2}} (0, -\Omega, \Delta). \quad (3.9)$$

The initial state at a time $t = -T/2$ is again $\chi_+(-T/2) = \chi_-(-T/2) = (1 0)$. The unitary time-evolution operator to reach the final time $T/2$ takes the form $e^{i\Delta T/2} R_2 R_1$ for incidence from the left (χ_+) and $e^{i\Delta T/2} R_1 R_2$ for incidence from

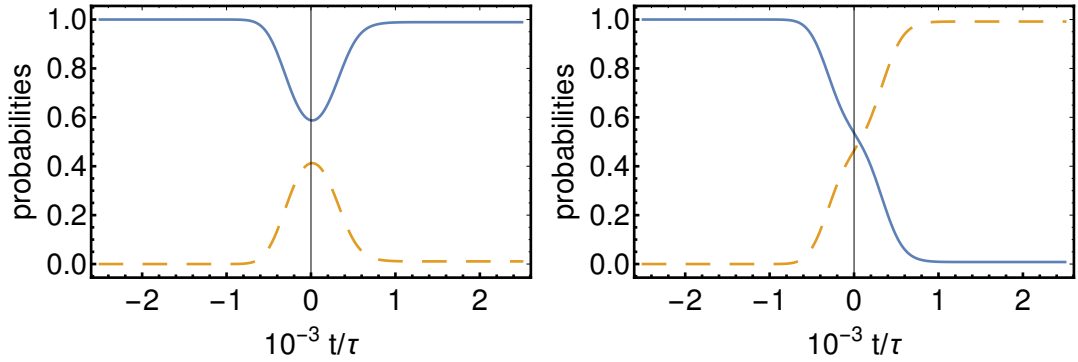


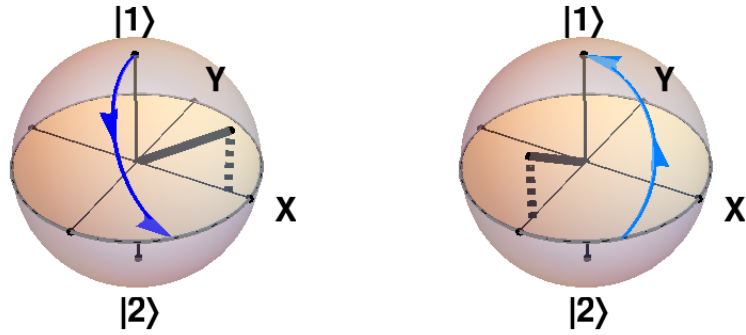
FIGURE 3.3: Simplified model of the asymmetric \mathcal{T}/\mathcal{A} device with symmetry VIII: (a) $\chi_+(t)$, (b) $\chi_-(t)$; ground-state population $|\chi_{\pm(t),1}|^2$ (blue, solid line), excited- $|\chi_{\pm(t),2}|^2$ (orange, dashed line). $v/v_d = 400$, $a\tau = 2618.19$, $x_0/d = 0.1532$, $\tau\Delta = 1413.01$.

the right (χ_-). The time T and the parameters Ω, Δ will be fixed to reproduce the results of the full calculation with the exact model so that the system starts in the ground state to end either in the ground state ($|\chi_+(\mathbf{T}/2)|^2 = 1$) or in the excited state by performing the rotations in one order or the reverse order ($|\chi_-(\mathbf{T}/2)|^2 = 0$). This gives $\Omega/\Delta = \sqrt{2}$ and $\mathbf{T} = 4\pi/(3\sqrt{3}\Delta)$. It follows that $\mathbf{n}_1 = \frac{1}{\sqrt{3}}(\sqrt{2}, 0, 1)$ and $\mathbf{n}_2 = \frac{1}{\sqrt{3}}(0, -\sqrt{2}, 1)$.

The different outcomes can thus be understood as the result of the non-commutativity of rotations on the Bloch sphere, see fig. 3.4: In fig. 3.4(a), first the rotation $R_1(\mathbf{T}/2)$ and then the rotation $R_2(\mathbf{T}/2)$ are performed. Starting in the ground state $|1\rangle$, the system ends up in the excited state $|2\rangle$. In fig. 3.4(b), first the rotation $R_2(\mathbf{T}/2)$ and then the rotation $R_1(\mathbf{T}/2)$ are performed: now the system starts and ends in the ground state $|1\rangle$.

These results can also be used to approximate the parameters of the potential in the quantum setting. As an approximation of the height a I assume that the area $a \int_{-\infty}^{\infty} dx g(x) = a\sqrt{\pi}w$ is equal to $\tilde{w}\Omega = \mathbf{T}v_0\Omega/2 = v_0\pi(2/3)^{3/2}$. This results in an approximation $a \approx \frac{v_0}{w}\sqrt{\pi}(2/3)^{3/2}$. As an additional approximation, we assume that $(a/\sqrt{2})/\Delta \approx \Omega/\Delta = \sqrt{2}$, so I get $\Delta \approx a/2 \approx \frac{v_0}{2w}\sqrt{\pi}(2/3)^{3/2}$. A comparison between these approximations and the numerically achieved parameters, see fig. 3.5, shows a good agreement over a large velocity range. This allows one to find good initial values for further numerical optimization.

(a) Order of rotations: first $R_1(T/2)$ (left figure) and then $R_2(T/2)$ (right figure).



(b) Order of rotations: first $R_2(T/2)$ (left figure) and then $R_1(T/2)$ (right figure).

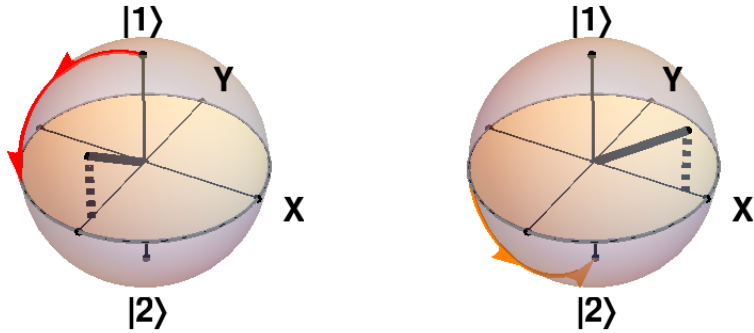


FIGURE 3.4: Simplified time-dependent model of the asymmetric \mathcal{T}/\mathcal{A} device with symmetry VIII: Bloch sphere explaining non time-reversal invariance, see text for details. The state trajectories are depicted in two-steps on the sphere. The rotation axes are also depicted. (a) The process simulates incidence from the left. The state starts and ends in $|1\rangle$. (b) The process simulates incidence from the right. The state starts at $|1\rangle$ and ends at $|2\rangle$.

3.4 Discussion

Since devices of technological interest, such as one-way filters for transmission or reflection, one-way barriers, one-way mirrors, and others, may be built based on the asymmetric scattering response of non-Hermitian Hamiltonians, there is both fundamental interest and applications in sight to implement Non-Hermitian scattering Hamiltonians. The results in this chapter are a step forward in that direction, specifically I propose a quantum-optical implementation of potentials

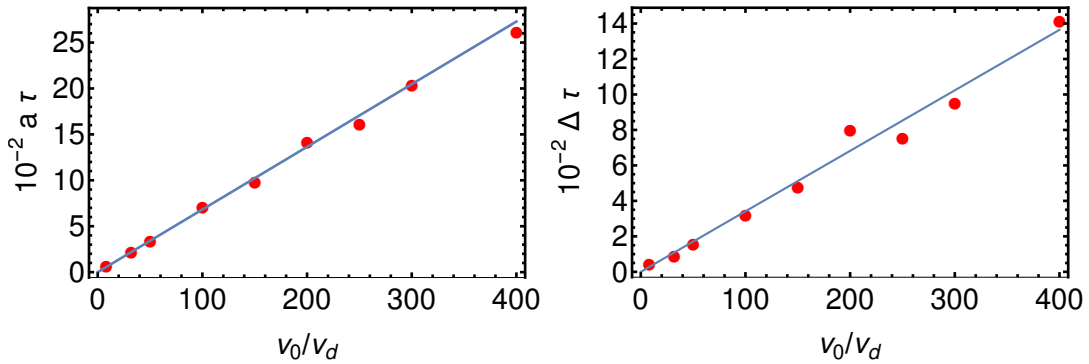


FIGURE 3.5: Asymmetric \mathcal{T}/\mathcal{A} device with symmetry VIII: comparison between numerically achieved parameters (red dots) and approximated parameters (blue, solid lines) versus velocity v_0 . (a) Height of Rabi frequency a , (b) detuning Δ .

with asymmetric scattering response. They are non-local and non-PT symmetrical, which allows for asymmetric transmission.

In general the chosen Hilbert space may be regarded as a subspace of a larger space. For example, the space of a “structureless particle” in 1D is the ground-state subspace for a particle with internal structure, consisting of two-levels in the simplest scenario. It is then possible to regard the Non-Hermitian physics in the reduced space as a projection of the larger space, which may itself be driven by a Hermitian or a Non-Hermitian Hamiltonian. I have used the Hermitian option in the examples, where I assumed a zero decay constant, $\gamma = 0$, for the excited state. A non-zero γ implies a Non-Hermitian Hamiltonian in the larger two-level space. The description may still be enlarged, including quantized field modes to account for the atom-field interaction with a Hermitian Hamiltonian. As an outlook, depending on the application, there might be the need for a more fundamental and detailed descriptive level. Presently I discuss the desired physics (i.e., the scattering asymmetries) at the level of the smallest 1D space of the ground state, while taking refuge in the two-level space to find a feasible physical implementation.

Part II

Heat rectification in mesoscopic systems

Chapter 4

Local Rectification of Heat Flux

In this chapter, a model for an atom-chain thermal rectifier is presented. The atoms in the chain are trapped in on-site harmonic potentials, and interact with their nearest neighbours by Morse potentials (or also by harmonic potentials in a simplified version). The chain is homogeneous except for a local modification of the interactions and trapping potential at one site, the “impurity”. The rectification mechanism is due here to the localized impurity, the only asymmetrical element of the structure, apart from the externally imposed temperature bias, and does not rely on putting in contact different materials or other known mechanisms such as grading or long-range interactions. The effect survives if all interaction forces are linear except the ones for the impurity.

The rest of the chapter is organized as follows. In section 4.1, I shall describe the homogeneous 1D chain, without the impurity. For this system, I numerically solve the dynamical equations, to show that the usual heat conduction applies. In section 4.2, I modify the potentials for one of the atoms and demonstrate the rectification effect. I also observe rectification when all the interaction Morse potentials are substituted by harmonic oscillators. Finally, in section 4.3, I summarize and discuss the results of this chapter.

4.1 Homogeneous one-dimensional chain

I start with a homogeneous 1D chain with N atoms coupled at both extremes to heat baths, at different temperatures T_h and T_c for “hot” and “cold” respectively.

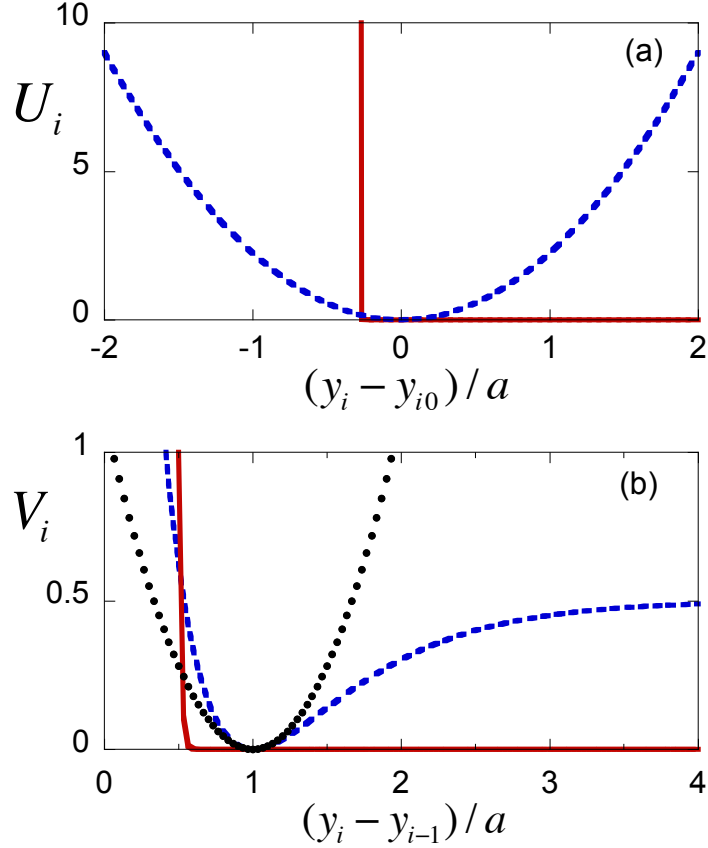


FIGURE 4.1: (a) On-site potentials: harmonic potential centered at the equilibrium position of each atom (dashed blue line) as a function of the displacement from this position $x_i = y_i - y_{i0}$ in a -units, and the on-site potential for the impurity, $i = N/2 + 1$ (N even, red solid line). (b) Interaction potentials as a function of the distance between nearest neighbors: Morse potential (blue dashed line) valid for all atoms except for $i = N/2 + 1$, N even, where the modified potential (red solid line) is used. The harmonic approximation of the Morse potential is also depicted (eq. (4.5), black dots, only used for fig. 4.5, below). Parameters: $D = 0.5$, $g = 1$, $\gamma = 45$, $d = 100$ and $b = 105$, used throughout the chapter.

The baths are modeled with a Nosé-Hoover method as described in [97]. Atoms 1 and N represent the first and the N -th atom in the chain, from left to right, that will be in contact with the baths. All the atoms are subjected to on-site potentials and to nearest-neighbor interactions, and their equilibrium positions y_{i0} are assumed to be equally spaced by a distance a . $x_i = y_i - y_{i0}$, $i = 1, \dots, N$, represent the displacements from the equilibrium positions of the corresponding atoms with positions y_i .

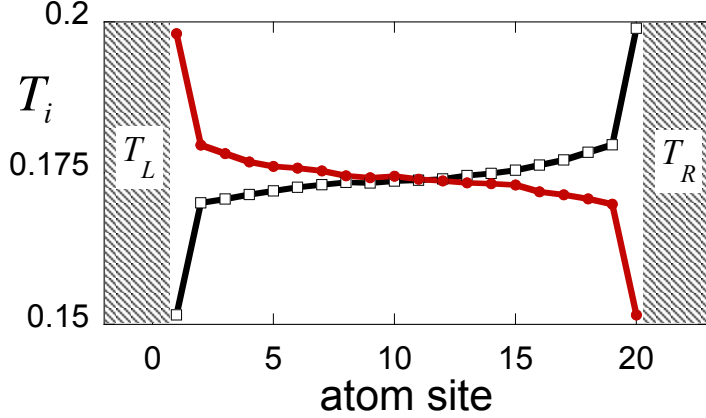


FIGURE 4.2: Symmetric temperature profiles for a homogeneous chain, without impurity. For $T_h = T_L$, $T_c = T_R$ (red solid dots) the (absolute value of) the heat flux is $J_{L \rightarrow R}$, equal to $J_{R \rightarrow L}$ for the reverse configuration of the bath temperatures, $T_h = T_R$, $T_c = T_L$ (black empty squares). Parameters as in fig. 4.1.

The classical Hamiltonian of the atom chain can be written in a general form as

$$H = \sum_{i=1}^N H_i, \quad (4.1)$$

with

$$\begin{aligned} H_1 &= \frac{p_1^2}{2m} + U_1(x_1) + V_L, \\ H_i &= \frac{p_i^2}{2m} + U_i(x_i) + V_i(x_{i-1}, x_i) \quad i = 2, \dots, N-1, \\ H_N &= \frac{p_N^2}{2m} + U_N(x_N) + V_N(x_{N-1}, x_N) + V_R, \end{aligned} \quad (4.2)$$

where the p_i are the momenta, $U_i(x_i)$ is the on-site potential for the i th atom, and $V_i(x_{i-1}, x_i)$ represents the atom-atom interaction potential. V_R and V_L are the interactions coupling the boundary atoms to the Nosé-Hoover thermostats, see [97].

There are a large number of 1D models that obey this general Hamiltonian. Different choices of the trapping and interaction potentials would give different conductivity behaviors. I choose a simple form of the Hamiltonian in which each atom is subjected to a harmonic on-site potential and a Morse interaction potential

between nearest neighbors (see fig. 4.1, dashed lines),

$$U_i(x_i) = \frac{1}{2}m\omega^2x_i^2, \quad (4.3)$$

$$V_i(x_{i-1}, x_i) = D \{e^{-\alpha[x_i - x_{i-1}]} - 1\}^2, \quad (4.4)$$

where ω is the trapping angular frequency, and D and α are time-independent parameters of the Morse potential. A “minimalist version” of the model where V becomes the harmonic limit of eq. (4.4), dotted line in fig. 1, will also be considered in the final discussion,

$$V_i(x_{i-1}, x_i) = k(x_i - x_{i-1})^2/2, \quad k = 2D\alpha^2. \quad (4.5)$$

For convenience, dimensionless units are used and the mass of all particles is set to unity.

I start by studying the homogeneous configuration with no impurity and potentials (4.3) and (4.4), solving numerically the dynamical equations for the Hamiltonian (4.1) with a Runge-Kutta-Fehlberg algorithm. I have chosen a low number of atoms, $N = 20$, with thermal baths at $T_h = 0.20$ and $T_c = 0.15$ at both ends of the chain with 16 thermostats each. The real temperature is related to the dimensionless one through $T_{real} = Tma^2\omega^2/k_B$ so, for typical values $m \approx 10^{-26}$ kg, $\omega \approx 10^{13}$ s⁻¹, $a \approx 10^{-10}$ m, and using $k_B = 1.38 \times 10^{-23}$ JK⁻¹, the dimensionless temperatures 0.15, 0.20, translate into 100, 150 K. It is advisable to use temperatures around these values in order to ensure that the displacements of the particles are realistic [98].

First I demonstrate the conductivity behavior of the model. To this end, I calculate the local heat flux J_i and temperature T_i , performing the numerical integration for long enough times to reach the stationary state. The local temperature is found as the time average $T_i = \langle p_i^2/m \rangle$, whereas J_i , from the continuity equation [99], is given by

$$J_i = -\dot{x}_i \frac{\partial V(x_{i-1}, x_i)}{\partial x_i}. \quad (4.6)$$

From now on I only consider the time average $\langle J_i(t) \rangle$, which converges to a constant value for all sites once the system is in the stationary nonequilibrium state. I depict the temperature profiles, for $N = 20$, first with $T_L = T_h$ and $T_R = T_c$ (L and R stand for left and right) and after switching the positions of the thermal baths in fig. 4.2. The profiles are symmetric, as expected, and the heat flux does not have

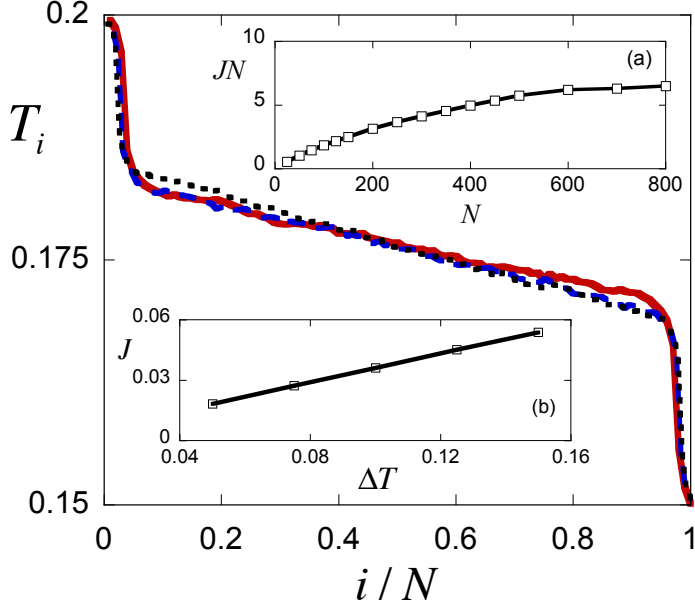


FIGURE 4.3: Temperature profile along the homogeneous chain for different number of atoms: 100 (dotted black line), 125 (dashed blue line) and 150 (solid red line). The atom sites have been rescaled with the total number of atoms. The time averages have been carried over a time interval of $\approx 2 \times 10^6$ after a transient of $\approx 1 \times 10^5$. In the inset (a), the product JN vs. N demonstrates that for long chains JN is independent of N . In (b) the linear dependence of J with ΔT for a fixed number of atoms, $N = 100$, is shown. Parameters as in fig. 4.1.

a preferred direction [25, 99]. Denoting the absolute values of the fluxes from the left (when $T_L = T_h$) as $J_{L \rightarrow R}$, and from the right (when $T_R = T_h$) as $J_{R \rightarrow L}$, I find that $J_{L \rightarrow R} = J_{R \rightarrow L} = J = 1.6 \times 10^{-2}$, in the dimensionless units, consistent with the values found in other models [25, 99].

The profile of the temperature is linear with boundary non-linearities at the edges, close to the thermal baths, due to the boundary conditions [100]. In fig. 4.3, I depict T_i vs i/N for $N = 100, 125$ and 150 with the same boundary conditions. For these larger atom numbers I have connected the first 3 and the last 3 atoms to the Nosé-Hoover baths. In the inset (a) of fig. 4.3 the product JN vs. N is plotted, showing that for a low N limit there is a well defined conductivity per unit length whereas for longer chains, JN tends to be constant which indicates a normal thermal conductivity independent of the length. Fixing the number of atoms to 100, as in the inset (b) of fig. 4.3, I observe a linear dependence between the flux and ΔT .

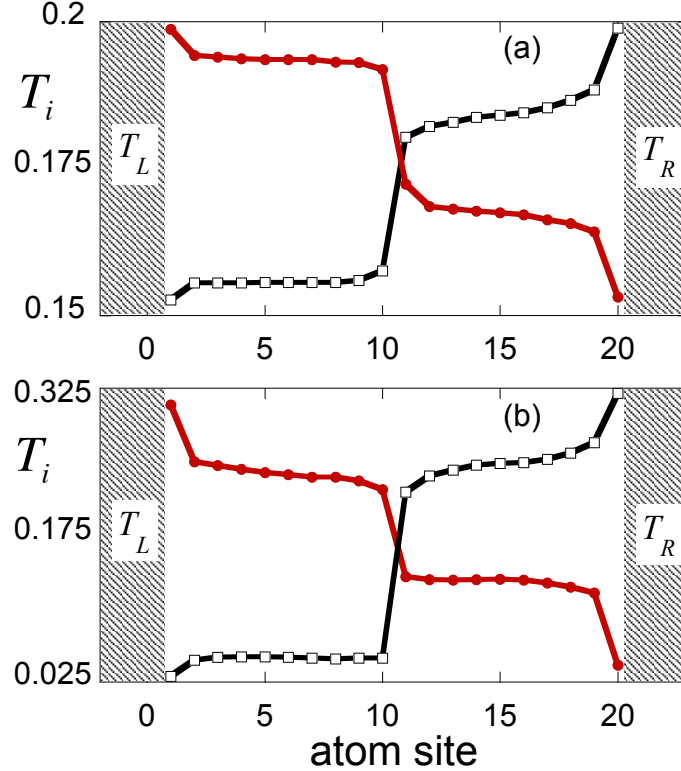


FIGURE 4.4: Temperature profile for the chain of $N = 20$ atoms, with an impurity in the $N/2 + 1$ position, with $T_L = T_h$ and $T_R = T_c$ (circles) and with the thermostat baths switched (squares). Parameters as in fig. 4.1. (a) $T_c = 0.15$, $T_h = 0.2$. $J_{L \rightarrow R} = 0.00769$ vs $J_{R \rightarrow L} = 0.00581$, with gives a rectification $R = 31\%$; (b) $T_c = 0.025$, $T_h = 0.325$. $J_{L \rightarrow R} = 0.0499$ vs $J_{R \rightarrow L} = 0.0140$, with $R = 256\%$.

4.2 Impurity-based thermal rectifier

To rectify the heat flux I modify the potentials for site $j = N/2 + 1$ with N even, as

$$U_j(x_j, t) = de^{-b[x_j(t)+a/3]}, \quad (4.7)$$

$$V_j(x_{j-1}, x_j, t) = ge^{-\gamma[x_j(t)-x_{j-1}(t)+a/2]}. \quad (4.8)$$

All the parameters involved, d, b , and g, γ are time-independent. In fig. 4.1 the modifications introduced with respect to the ordinary sites are shown (solid lines). The different on-site and interaction terms introduce soft-wall potentials (instead of hard-walls to aid in integrating the dynamical equations) that make it difficult for the impurity to transmit its excitation to the left whereas left-to-right transmission is still possible. This effect is facilitated by the relative size of the coefficients, $a/3 < a/2$, that determine the position of the walls. These positions imply that

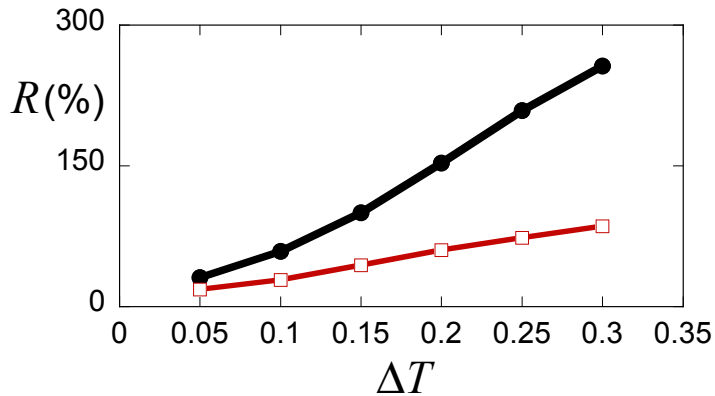


FIGURE 4.5: Rectification factor R as a function of the temperature difference between ends of the chain of atoms, ΔT . I have changed both T_h and T_c according to $T_c = 0.15 - (\Delta T - 0.05)/2$ and $T_h = 0.2 + (\Delta T - 0.05)/2$, with $N = 20$, keeping the rest of parameters as in fig. 4.1. Interatomic potentials: Morse potential, eq. (4.4) (black line with circles, see the temperature profiles of extreme points in fig. 4.4); harmonic potential, eq. (4.5) (red line with squares).

an impurity excited by a hot right bath cannot affect its left cold neighbour near its equilibrium position at the $j - 1$ site. However, if the left $j - 1$ atom is excited from a hot bath on the left, it can get close enough to the impurity to kick it and transfer kinetic energy.

After extensive numerical simulations, I have chosen the values of these parameters as in fig. 4.1, such that the conductivity in the forward direction, $J_{L \rightarrow R}$, and the rectification factor, defined as $R = (J_{L \rightarrow R} - J_{R \rightarrow L})/J_{R \rightarrow L} \times 100$, are both large for $T_h = 0.2$, $T_c = 0.15$. A large R without a large $J_{L \rightarrow R}$ could in fact be useless [27]. Note that the parameters are not necessarily the optimal combination, which in any case would depend on the exact definition of “optimal” (technically on how $J_{L \rightarrow R}/J$ and R are weighted and combined in a cost function and on the limits imposed on the parameter values). This definition is an interesting question but it goes beyond the scope of this chapter, which is to demonstrate and discuss the effect of the localized impurity.

I have used again $N = 20$ atoms connected to baths of 16 thermostats each, with the same temperatures as for the homogeneous chain, and numerically solved the dynamical equations to calculate the local temperature and the heat flux for both configurations of the baths. The interatomic potential for the regular atoms is the Morse potential (4.4). In fig. 4.4(a), the temperature profiles show a clear asymmetry between $L \rightarrow R$ and $R \rightarrow L$. Specifically, I find $J_{L \rightarrow R} = 7.6 \times 10^{-3}$ and

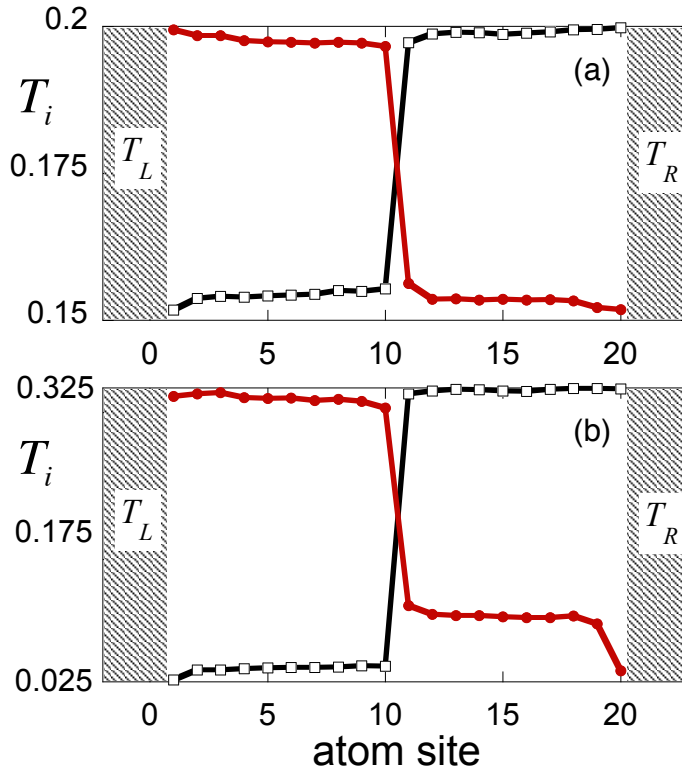


FIGURE 4.6: Temperature profile for a harmonic interacting chain of $N = 20$ atoms, with an impurity in the $N/2 + 1$ position, with $T_L = T_h$ and $T_R = T_c$ (circles) and with the thermostat baths switched (squares), for (a) $\Delta T = 0.05$ and (b) $\Delta T = 0.3$. The corresponding rectification factors are (a) $R = 18\%$ and (b) $R = 85\%$. Parameters regarding the impurity are the same as in fig. 4.1.

$J_{R \rightarrow L} = 5.8 \times 10^{-3}$ which gives $R = 31\%$. The effect decays with longer chains, with, for example, $R = 19\%$ for $N = 100$, and $R = 17.8\%$ for $N = 150$.

These temperature profiles depend on the difference between the bath temperatures, see e.g. fig. 4.4(b). Increasing the temperature gap, but keeping T_h low enough so that the displacement of the atoms from their equilibrium positions is realistic, I find higher values of R . Figure 4.5 shows the strong dependence of R with ΔT (black circles). I have changed both T_h and T_c so that the mean temperature $(T_c + T_h)/2$ remains constant.

4.3 Discussion

I have presented a scheme for thermal rectification using a one-dimensional chain of atoms which is homogeneous except for the special interactions of one of them, the impurity, and the couplings with the baths at the boundaries. These

proof-of-principle results for an impurity-based rectification mechanism may encourage further exploration of the impurity-based rectification, in particular of the effect of different forms for the impurity on-site potential and its interactions with neighboring atoms. In contrast to the majority of chain models, the structural asymmetry in the present model is only in the impurity. The idea of a localized effect was already implicit in early works on a two-segment Frenkel-Kontorova model [26, 38], where rectification depended crucially on the interaction constant coupling between the two segments. However, the coupling interaction was symmetrical and the asymmetry was provided by the different nature (parameters) of the segments put in contact. Also different from common chain models are the potentials chosen here. Instead of using the Morse potential as an on-site model, see e.g. [25], I have considered a natural setting where this potential characterizes the interatomic interactions, and the on-site potential is symmetrical with respect to the equilibrium position, and actually harmonic. The numerical results indicate that this model is consistent with normal conduction, and also helps to isolate and identify the local-impurity mechanism for rectification. In this regard it is useful to consider a further simplification, in the spirit of the minimalists models proposed by Pereira [55], so as to distill further the essence of the local rectification mechanism. If the Morse interatomic interaction is substituted by the corresponding harmonic interaction, see the black dotted line in fig. 4.1(b), the rectification effect remains, albeit slightly reduced, see fig. 4.5. The chain is then perfectly linear with the only non-linear exception localized at the impurity. The temperature dependent feature mentioned in [55] as the second necessary condition for rectification besides asymmetry, is here localized in the impurity too, and consists of a different capability to transfer kinetic energy depending on the temperatures on both sides of the impurity. Figure 4.6 shows temperature profiles for the purely harmonic chain to be compared with the Morse-interaction chain in fig. 4.4. Flatter profiles are found on both sides of the impurity, as corresponds to the abnormal transport expected for harmonic chains [101]. It would be interesting to combine the impurity effect with other rectification mechanisms (such as grading, long-range interactions, or use of different segments), or with more impurities in series to enhance further the rectification effect.

Even though the motivation was to mimic the effect of a localized atom diode that lets atoms pass only one way, unlike the atom diode [6], all interactions in the present model are elastic. The model may be extended by adding an irreversible, dissipative element so as to induce not only rectification but a truly Maxwell demon

for heat transfer [92, 102]. On the experimental side, one dimensional chains of neutral atoms in optical lattices can be implemented with cold atoms [103]. An impurity with different internal structure could be subjected to a different on-site potential imprinted by a holographic mask [104], and asymmetrical interatomic interactions could be implemented by trapping a controllable polar molecule or mediated by atoms in parallel lattices [105].

Chapter 5

Asymmetric heat transport in ion crystals

In this chapter I propose to bridge the gap between mathematical models and actual physical systems by exploring the implementation of a thermal rectifier in a realistic, graded system with long-range interactions: a chain of ultracold ions in a segmented Paul trap with frequency-graded microtraps for each ion. Long-range interactions are due to the Coulomb forces, and the baths at the ends of the chain may be implemented with optical molasses (see fig. 5.1). The trapping frequencies of the microtraps are controlled individually in order to create a graded and asymmetric trap-frequency profile along the chain. This asymmetry will lead to a heat flow that depends on the sign of the temperature difference of the baths. Heat transport in trapped-ion chains has been studied in several works [106–110] and interesting phenomena like phase transitions have been investigated [106–109]. The idea of using locally-controlled traps is already mentioned in [106] to implement disorder and study its effects. The device I present here may be challenging to implement, but at reach with the current technology, in particular that of microfabricated traps [111–113]. Thus the setting is thought for a small, realistic number of controllable ions.

The chapter is organized as follows. In section 5.1, I describe the physical system of trapped ions with graded trap frequencies. I also set the stochastic dynamics due to the action of lasers at the chain edges. In section 5.2, I implement an efficient method to find the steady state using Novikov’s theorem and solving an algebraic system of equations. In section 5.3, I present simulations of this system

exhibiting thermal rectification and discuss the dependence with the number of ions, different options for the ion-laser coupling, and the advantages/disadvantages of using a graded frequency profile instead of a segmented one. Finally, in section 5.4, I summarize the conclusions, and discuss connections with other works.

5.1 Physical System

Consider a linear lattice of N individual harmonic traps of (angular) trapping frequencies ω_n evenly distributed along the x axis at a distance a from each other. Each trap contains a single ion that interacts with the rest via Coulomb potentials. All the ions are of the same species, with mass m and charge q . The Hamiltonian that describes the dynamics of the system is (I consider only one-dimensional motion along the chain axis)

$$H(\mathbf{x}, \mathbf{p}) = \sum_{n=1}^N \left[\frac{p_n^2}{2m} + \frac{m\omega_n^2}{2} (x_n - x_n^{(0)})^2 \right] + V_{int}(\mathbf{x}), \quad (5.1)$$

where $\{x_n, p_n\}$, position and momentum of each ion, are the components of the vectors \mathbf{x}, \mathbf{p} , $x_n^{(0)} = na$ are the centers of the harmonic traps, and V_{int} is the sum of the Coulomb interaction potential between all pairs of ions,

$$V_{int}(\mathbf{x}) = \frac{1}{2} \sum_n \sum_{l \neq n} V_C(|x_n - x_l|), \quad (5.2)$$

with $V_C(|x_n - x_l|) = \frac{q^2}{4\pi\epsilon_0} \frac{1}{|x_n - x_l|}$. The ends of the chain are in contact with two thermal reservoirs at temperatures T_L for the left bath and T_R for the right bath respectively. The action of the reservoirs on the dynamics of the chain is modeled via Langevin baths at temperatures T_L and T_R [101, 114]. The equations of motion of the chain, taking into account the baths and the Hamiltonian, are

$$\begin{aligned} \dot{x}_n &= \frac{1}{m} p_n, \\ \dot{p}_n &= -m\omega_n^2(x_n - x_n^{(0)}) - \frac{\partial V_{int}}{\partial x_n} - \frac{\gamma_n}{m} p_n + \xi_n(t), \end{aligned} \quad (5.3)$$

where γ_n and $\xi_n(t)$ are only non-zero for the ions in the end regions, in contact with the left and right baths in the sets $\mathcal{L} = \{1, 2, \dots, N_L\}$ and $\mathcal{R} = \{N - (N_R - 1), \dots, N - 1, N\}$, see fig. 5.1. γ_n are friction coefficients and

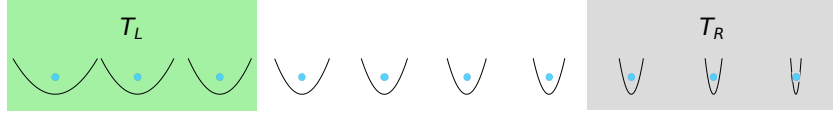


FIGURE 5.1: Schematic representation of the frequency-graded chain of trapped ions proposed as a thermal rectifier. The left and right ends of the chain are in contact with optical molasses at temperatures T_L and T_R (green and grey boxes respectively). Each ion is in an individual trap. The (angular) frequencies of the traps increase homogeneously from left to right, starting from ω_1 and ending at $\omega_1 + \Delta\omega$. The ions interact through the Coulomb force, which is long range, and therefore all the ions interact among them, even distant neighbors. By default I use 15 ions.

$\xi_n(t)$ are uncorrelated Gaussian noise forces satisfying $\langle \xi_n(t) \rangle = 0$ and $\langle \xi_n(t) \xi_m(t') \rangle = 2D_n \delta_{nm} \delta(t - t')$, D_n being the diffusion coefficients. These Gaussian forces are formally the time derivatives of independent Wiener processes (Brownian motions) $\xi_n(t) = \sqrt{2D_n} \frac{dW_n}{dt}$ [107, 115] and eq. (5.3) is a stochastic differential equation (SDE) in the Stratonovich sense [115].

The baths are physically implemented by optical molasses consisting of a pair of counterpropagating Doppler-cooling lasers [107]. The friction and diffusion coefficients for the ions in contact with the baths are given in [107, 116, 117]

$$\begin{aligned} \gamma_n &= -4\hbar k_{L,R}^2 \left(\frac{I_{L,R}}{I_0} \right) \frac{2\delta_{L,R}/\Gamma}{[1 + (2\delta_{L,R}/\Gamma)^2]^2}, \\ D_n &= \hbar^2 k_{L,R}^2 \left(\frac{I_{L,R}}{I_0} \right) \frac{\Gamma}{1 + (2\delta_{L,R}/\Gamma)^2}, \\ n &\in \mathcal{L}, \mathcal{R}, \end{aligned} \quad (5.4)$$

where k_L (k_R) and I_L (I_R) are the wave vector and intensity of the left (right) laser. δ_L (δ_R) is the detuning of the left (right) laser with respect to the angular frequency ω_0 of the atomic transition the laser is exciting, and Γ is the corresponding natural line width of the excited state. The expressions in eq. (5.4) are valid only if the intensities of the lasers are small compared to the saturation intensity I_0 , $I_{L,R}/I_0 \ll 1$. In this bath model, the friction term in eq. (5.3) comes from the cooling action of the laser and the white noise force $\xi_n(t)$ corresponds to the random recoil of the ions due to spontaneous emission of photons [116, 117]. Using the diffusion-dissipation relation $D = \gamma k_B T$ [118], the temperatures of the optical molasses baths are given by

$$T_{L,R} = -\frac{\hbar\Gamma}{4k_B} \frac{1 + (2\delta_{L,R}/\Gamma)^2}{(2\delta_{L,R}/\Gamma)}, \quad (5.5)$$

with k_B being the Boltzmann constant. If the laser intensities are low enough, the temperatures of the baths are controlled by modifying the detunings. When $\delta = \delta_D = -\Gamma/2$ the optical molasses reach their minimum possible temperature, the Doppler limit $T_D = \hbar\Gamma/(2k_B)$. Note that away from the Doppler limit the same temperature may be achieved for two different values of the detuning. These two possibilities imply different couplings (two different pairs of γ and D values) and thus different physical effects that will be studied in Sec. 5.3.3.

5.2 Calculation of the stationary heat currents

The local energy of each site is defined by

$$H_n = \frac{1}{2m}p_n^2 + \frac{1}{2}m\omega_n^2(x_n - x_n^{(0)})^2 + \frac{1}{2}\sum_{l \neq n}V_C(|x_n - x_l|). \quad (5.6)$$

Differentiating H_n with respect to time I find the continuity equation

$$\dot{H}_n = \frac{p_n}{m}\left[\xi_n(t) - \gamma_n\frac{p_n}{m}\right] - \frac{1}{2m}\sum_{l \neq n}\frac{\partial V_C(|x_n - x_l|)}{\partial x_n}(p_n + p_l). \quad (5.7)$$

Two different contributions can be distinguished: $j_n^B \equiv \frac{p_n}{m}\left[\xi_n(t) - \gamma_n\frac{p_n}{m}\right]$, which is the energy flow from the laser reservoir to the ions at the edges of the chain (only for $n \in \mathcal{L}, \mathcal{R}$), and $\dot{H}_n^{int} \equiv -\frac{1}{2m}\sum_{l \neq n}\frac{\partial V_C(|x_n - x_l|)}{\partial x_n}(p_n + p_l)$, which gives the “internal” energy flow due to the interactions with the rest of the ions. In the steady state $\langle \dot{H}_n \rangle = 0$, and therefore

$$\langle j_n^B \rangle + \langle \dot{H}_n^{int} \rangle = 0, \quad (5.8)$$

where $\langle \dots \rangle$ stands for the expectation value with respect to the ensemble of noise processes $\boldsymbol{\xi}(t)$ ($\boldsymbol{\xi}$ represents a vector with components ξ_n). Equation (5.8) implies that, in the steady state, the internal rates \dot{H}_n^{int} vanish for the inner ions of the chain because $j_n^B = 0$ for $n \notin \mathcal{L}, \mathcal{R}$. In chains with nearest-neighbor (NN) interactions, $\langle \dot{H}_n^{int} \rangle$ simplifies to two compensating and equal-in-magnitude contributions that define the homogeneous heat flux across the chain. For long-range interactions this is not so and defining the flux is not so straightforward. A formal possibility is to impose nearest-neighbor interatomic interactions for some atoms in the chain [40], but this approach is not realistic in the current system so I define

instead the heat currents for the left and right baths as

$$\begin{aligned} J_L(t) &= \sum_{n \in \mathcal{L}} \langle j_n^B \rangle, \\ J_R(t) &= \sum_{n \in \mathcal{R}} \langle j_n^B \rangle, \end{aligned} \quad (5.9)$$

respectively. These expressions are in general time-dependent. In the steady state $J_{L,\text{steady}}$ and $J_{R,\text{steady}}$ should cancel each other since the local energies stabilize and internal energy flows cancel. I will use either $J_{L,\text{steady}}$ or $J_{R,\text{steady}}$ to calculate the total energy flow in the chain, always taking the absolute value, i.e., $J \equiv |J_{L,\text{steady}}| = |J_{R,\text{steady}}|$. J is defined as J_\rightarrow when the hot bath is on the left and J_\leftarrow when it is on the right.

To compute the average heat fluxes of the baths $\langle j_n^B \rangle$ in eq. (5.9) I need the averages $\langle p_n(t)\xi_n(t) \rangle$. Instead of explicitly averaging $p_n(t)\xi_n(t)$ over different realizations of the white noise, I use Novikov's theorem [115, 119, 120]. Novikov's theorem states that the ensemble average (over the realizations of the noise) of the product of some functional $\phi(t)$, which depends on a set of n_{noise} Gaussian noises $\xi_i(t)$ with zero mean value, $\langle \xi_i(t) \rangle = 0$, and the noise itself, is given by

$$\langle \xi_i(t)\phi(t) \rangle = \sum_{j=1}^{n_{\text{noise}}} \int_0^t dt' \langle \xi_i(t)\xi_j(t') \rangle \left\langle \frac{\delta\phi(t)}{\delta\xi_j(t')} \right\rangle, \quad (5.10)$$

where $\delta\phi(t)/\delta\xi_j(t')$ is the functional derivative of $\phi(t)$ with respect to the j -th component of the noise. Since the noises are independent from each other and δ -correlated,

$$\begin{aligned} \langle \xi_i(t)\phi(t) \rangle &= 2D_i \underbrace{\int_0^t dt' \delta(t-t') \left\langle \frac{\delta\phi(t)}{\delta\xi_i(t')} \right\rangle}_{= \frac{1}{2} \lim_{t' \rightarrow t^-} \left\langle \frac{\delta\phi(t)}{\delta\xi_i(t')} \right\rangle} \\ &= D_i \lim_{t' \rightarrow t^-} \left\langle \frac{\delta\phi(t)}{\delta\xi_i(t')} \right\rangle. \end{aligned} \quad (5.11)$$

The $1/2$ factor from the integral in eq. (5.11) comes from the assumption that the Dirac delta function is the limit of even correlation functions when the correlation time goes to 0. The notation $\lim_{t' \rightarrow t^-}$ stands for the limit when t' goes to t from below ($t' < t$). To evaluate the functional derivatives of the position $x_n(t)$ and momentum $p_n(t)$ coordinates with respect to the white noises, I integrate eq. (5.3) to have its formal solution as a functional depending on the white Gaussian noises

$\xi_n(t)$,

$$\begin{aligned} x_n(t) &= x_n(0) + \frac{1}{m} \int_0^t ds p_n(s), \\ p_n(t) &= p_n(0) + \int_0^t ds \left[-\frac{\partial H}{\partial x_n}(s) - \frac{\gamma_n}{m} p_n(s) + \xi_n(s) \right]. \end{aligned} \quad (5.12)$$

Taking the functional derivatives of eq. (5.12) I get for $t' < t$

$$\begin{aligned} \frac{\delta x_n(t)}{\delta \xi_m(t')} &= \frac{1}{m} \int_{t'}^t ds \frac{\delta p_n(s)}{\delta \xi_m(t')}, \\ \frac{\delta p_n(t)}{\delta \xi_m(t')} &= \delta_{nm} - \int_{t'}^t ds \frac{\delta}{\delta \xi_m(t')} \left[\frac{\partial H}{\partial x_n}(s) + \frac{\gamma_n}{m} p_n(s) \right]. \end{aligned} \quad (5.13)$$

The integration limits in eq. (5.13) go from t' to t since the functional derivatives are 0 when $s < t'$, because the values of the noise in the future cannot affect a signal in the present, which would break causality. I have also used that $\frac{\delta \xi_n(t)}{\delta \xi_m(t')} = \delta_{nm} \delta(t - t')$. Taking the limit $t' \rightarrow t^-$ in eq. (5.12) I obtain the values of the functional derivatives of x_n and p_n , $\lim_{t' \rightarrow t^-} \delta x_n(t)/\delta \xi_m(t') = 0$ and $\lim_{t' \rightarrow t^-} \delta p_n(t)/\delta \xi_m(t') = \delta_{nm}$ (δ_{nm} is the usual Kronecker delta). Thus I have $\langle x_n(t) \xi_m(t) \rangle = 0$ and $\langle p_n(t) \xi_m(t) \rangle = \delta_{nm} D_m$, which gives for the heat flow from the baths

$$\langle j_n^B \rangle = \frac{1}{m} \left[D_n - \gamma_n \frac{\langle p_n^2 \rangle}{m} \right]. \quad (5.14)$$

In all simulations I check that $|J_{L,\text{steady}}| = |J_{R,\text{steady}}|$ within the numerical tolerance of the computer. To measure the asymmetry of the heat currents I use the rectification factor R defined as

$$R = \frac{J_\rightarrow - J_\leftarrow}{\max(J_\rightarrow, J_\leftarrow)}. \quad (5.15)$$

R may go from -1 to 1 (In the figures I depict it in % between -100% and 100%). If there is no rectification $J_\rightarrow = J_\leftarrow$ and $R = 0$. For perfect rectification in the right (left) direction, $J_\rightarrow \gg J_\leftarrow$ ($J_\rightarrow \ll J_\leftarrow$), and $R = 1$ ($R = -1$). Notice that other definitions of rectification factors exist in many works on asymmetric heat transfer so comparisons should be done with care.

This model does not show the antithermodynamical behavior observed in other models [121, 122], and heat is found to flow in all cases from the hot to the cold bath.

5.2.1 Algebraic, small-oscillations approach to calculate the steady state

To find the temperature profiles and heat currents in the steady state the usual approach is to solve the SDE system in eq. (5.3) up to long times and for many realizations of the white noises $\xi(t)$. In that way, the ensemble averages $\langle p_n(t \rightarrow \infty)^2 \rangle$, necessary for both the temperature profiles and heat currents, are computed. This standard route implies a heavy computational effort, in particular when I want to study the heat transport for several bath configurations, frequency increments and chain parameters. It is possible to circumvent this difficulty and find ensemble averages like $\langle x_n x_m \rangle$, $\langle x_n p_m \rangle$, $\langle p_n p_m \rangle$ (second order moments) without integrating any SDE [123–125]. The idea is to impose the condition $d\langle \cdot \cdot \cdot \rangle / dt = 0$ for all the second order moments and linearize the dynamical equations of the system around equilibrium. A system of linear algebraic equations for the moments results, that can be easily solved without solving the SDE many times.

To linearize the SDE in eq. (5.3) I approximate the potential energy of the Hamiltonian in eq. (5.1), $V(\mathbf{x}) = V_{int}(\mathbf{x}) + m \sum_n \omega_n^2 (x_n - x_n^{(0)})^2 / 2$, by its harmonic approximation around the equilibrium positions \mathbf{x}^{eq} , defined by $\frac{\partial V(\mathbf{x})}{\partial \mathbf{x}} \Big|_{\mathbf{x}=\mathbf{x}^{eq}} = 0$. The approximate potential (ignoring the zero-point energy) is

$$V(\mathbf{x}) \approx \frac{1}{2} \sum_{n,m} K_{nm} (x_n - x_n^{eq})(x_m - x_m^{eq}), \quad (5.16)$$

with $K_{nm} = \frac{\partial^2 V(\mathbf{x})}{\partial x_n \partial x_m} \Big|_{\mathbf{x}=\mathbf{x}^{eq}}$ being the Hessian matrix entries of $V(\mathbf{x})$ around the equilibrium configuration [126]

$$K_{nm} = \begin{cases} m\omega_n^2 + 2 \left(\frac{q^2}{4\pi\varepsilon_0} \right) \sum_{l \neq n} \frac{1}{|x_n^{eq} - x_l^{eq}|^3} & \text{if } n = m \\ -2 \left(\frac{q^2}{4\pi\varepsilon_0} \right) \frac{1}{|x_n^{eq} - x_m^{eq}|^3} & \text{if } n \neq m \end{cases}. \quad (5.17)$$

Note that this approximation does not modify the two main features of the system, namely asymmetry and long-range interactions, which are manifest in the asymmetric distribution of ω_n and the non-zero off-diagonal elements of the K matrix, respectively. In the following I will use $y_n = x_n - x_n^{eq}$ to simplify the notation.

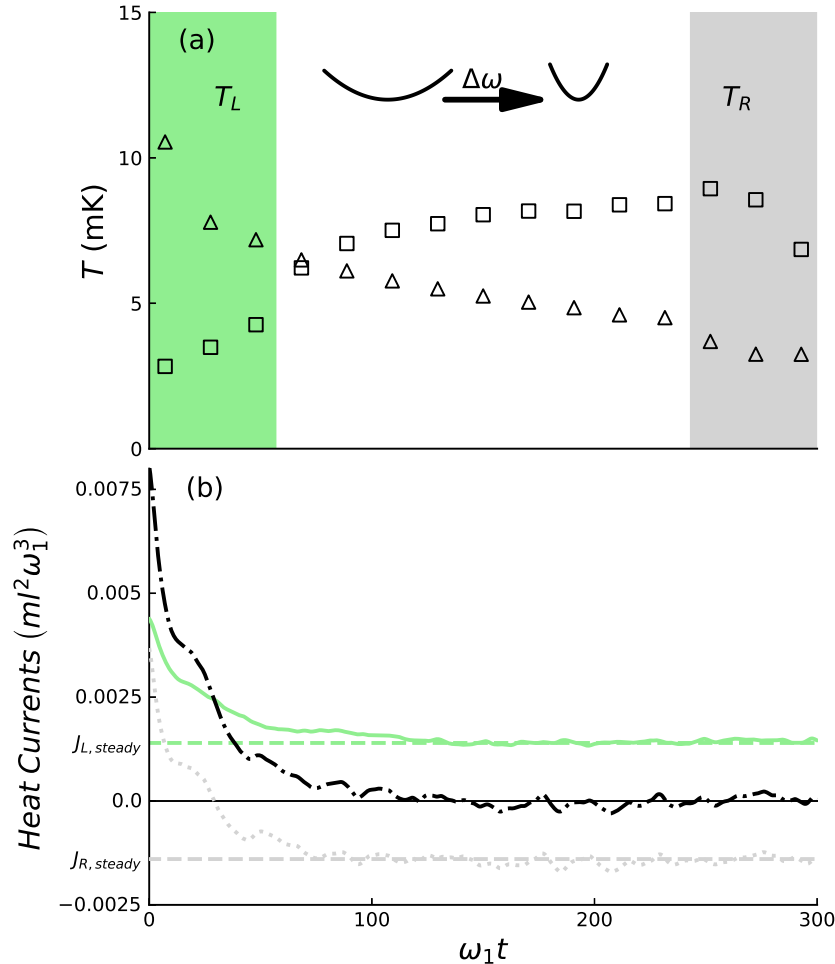


FIGURE 5.2: (a) Temperatures of the ions in the stationary state for a graded chain with the parameters described in section 5.3.1. The temperature profiles found with the algebraic method (eq. (5.19)) are indistinguishable from the ones found solving the Langevin equation (eq. (5.3)). Empty triangles (squares) correspond to $T_L = T_H$ ($T_L = T_C$) and $T_R = T_C$ ($T_R = T_H$). (b) Heat currents as a function of time for $T_L = T_H$ and $T_R = T_C$, see eq. (5.9): $J_L(t)$ (solid green line) from the left reservoir into the chain; $J_R(t)$ (dotted grey line) from the right reservoir into the chain (negative except at very short times); $J_L(t) + J_R(t)$ (dotted-dashed black line), which must go to zero in the steady state. The three lines tend to stationary values marked by horizontal lines. Parameters: $\omega_1 = 2\pi \times 50$ kHz, $a = 50$ μm , $\delta_H = -0.02\Gamma$, and $\delta_C = -0.1\Gamma$, which gives temperatures $T_H \approx 12$ mK and $T_C \approx 3$ mK. $\Delta\omega = 0.5\omega_1$. In all figures $\Gamma = 2\pi \times 41.3$ MHz.

The linearized dynamics around the equilibrium positions are given by

$$\begin{aligned}\dot{y}_n &= \frac{1}{m} p_n, \\ \dot{p}_n &= - \sum_l K_{nl} y_l - \frac{\gamma_n}{m} p_n + \xi_n(t).\end{aligned}\tag{5.18}$$

Now, I set $d\langle\cdots\rangle/dt = 0$ for all the moments. Using eq. (5.18) and applying Novikov's theorem I find

$$\begin{aligned}\langle p_n p_l \rangle - \gamma_l \langle y_n p_l \rangle - \sum_m K_{lm} \langle y_n y_m \rangle &= 0, \\ \sum_m [K_{nm} \langle y_m p_l \rangle + K_{lm} \langle y_m p_n \rangle] + \frac{1}{m} (\gamma_l + \gamma_n) \langle p_n p_l \rangle &= 2\delta_{nl} D_n.\end{aligned}\tag{5.19}$$

The system (5.19) is linear in the second order moments so it can be solved numerically to find the steady-state values of the moments. Besides eq. (5.19) I have that $\langle y_n p_l \rangle = -\langle y_l p_n \rangle$, which follows from eq. (5.18) and $d\langle y_n y_m \rangle / dt = 0$. Since there are $\frac{1}{2}N(N-1)$ independent $\langle y_n p_l \rangle$ moments, I choose the ones with $n < l$. Similarly, the moments $\langle y_n y_l \rangle$ and $\langle p_n p_l \rangle$ contribute with $\frac{1}{2}N(N+1)$ independent variables each and I choose the ones with $n \leq m$. Thus there are in total $\frac{1}{2}N(3N+1)$ independent moments that can be arranged in the vector

$$\boldsymbol{\eta} = \left[\begin{array}{l} \langle y_1 y_1 \rangle, \langle y_1 y_2 \rangle, \dots, \langle y_N y_N \rangle, \\ \langle p_1 p_1 \rangle, \langle p_1 p_2 \rangle, \dots, \langle p_N p_N \rangle, \\ \langle y_1 p_2 \rangle, \langle y_1 p_3 \rangle, \dots, \langle y_{N-1} p_N \rangle \end{array} \right]^T.\tag{5.20}$$

There are the same number of independent equations as independent moments: N^2 equations correspond to the first line in eq. (5.19), and $\frac{1}{2}N(N+1)$ equations to the second line because of the symmetry with respect to n, l . The system of equations (5.19) may be compactly written as $\mathbf{A}\boldsymbol{\eta} = \mathbf{B}$, where \mathbf{A} and \mathbf{B} are a $\frac{1}{2}N(3N+1)$ square matrix and vector.

5.3 Numerical Results

I now display the results of the simulations. To find the temperature profiles and the currents in the steady state I use the algebraic method described in section 5.2.1. I also check that the results coincide with those by solving eq. (5.3) for many different realizations of the noise forces $\xi(t)$ and averaging. The code for all the numerical simulations has been written in the language *Julia* [127, 128]. In particular, to solve the Langevin equation, I used *Julia*'s package *DifferentialEquations.jl* [129].

To model the baths and the chain I use atomic data taken from ion trap experiments [130, 131]. I consider 15 $^{24}\text{Mg}^+$ ions in all figures except in fig. 5.6. Only the three leftmost and three rightmost ions interact with Doppler cooling lasers. The Doppler cooling lasers excite the transition $3s^2 S_{1/2} \rightarrow 3p^2 P_{1/2}$, with angular frequency $\omega_0 = 2\pi \times 1069$ THz and excited state line width $\Gamma = 2\pi \times 41.3$ MHz [107]. For this ionic species and atomic transition the Doppler limit is $T_D = 1$ mK. The intensities of the laser beams are small compared to the saturation intensity I_0 so that eq. (5.4) holds. I take $I_n/I_0 = 0.08$ for the ions in the laser beams, whereas $I_n = 0$ for the rest.

The temperatures T_L, T_R of the left and right laser baths are controlled with their detunings δ_L, δ_R with respect to the atomic transition. I fix two values for the detunings, δ_H and δ_C , such that $T_H > T_C$ (hot and cold baths, also source and drain) and I define $J_\rightarrow (J_\leftarrow)$ as the stationary heat current in the chain when $T_L = T_H$ and $T_R = T_C$ ($T_L = T_C$ and $T_R = T_H$).

Except in Sec. 5.3.5 I consider a graded frequency profile. If the frequency of the leftmost trap is ω_1 , the frequency of the n th trap will be $\omega_n = \omega_1 + \Delta\omega \frac{n-1}{N-1}$ up to $\omega_1 + \Delta\omega$ for the rightmost trap. In Sec. 5.3.5, I compare the graded chain to a segmented chain, where the left half of the chain has trapping frequencies ω_1 while the other half has $\omega_1 + \Delta\omega$.

5.3.1 Evolution to steady state

To compare the results by solving eq. (5.3) and averaging and those from the algebraic method, I simulated a frequency graded chain with a trapping frequency $\omega_1 = 2\pi \times 50$ kHz for the leftmost ion, see fig. 5.2. The number of ions interacting

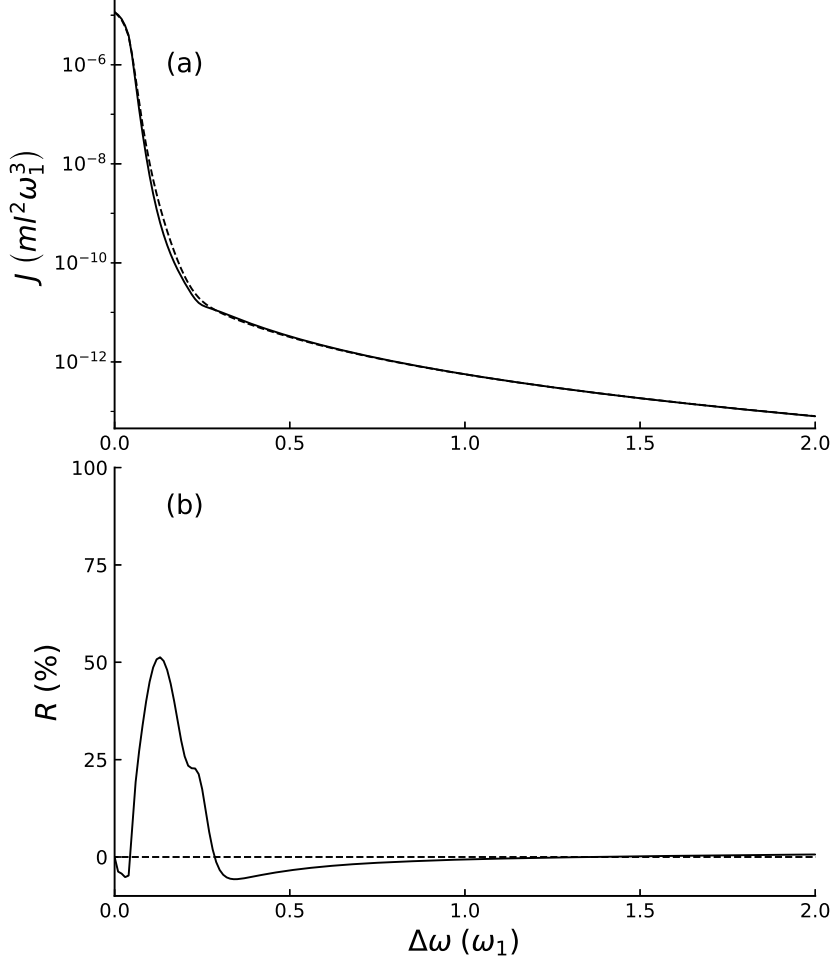


FIGURE 5.3: Graded chain of $N = 15$ $^{24}\text{Mg}^+$ ions. (a) Stationary fluxes for different frequency increments: J_{\rightarrow} (for $T_L = T_H$ and $T_R = T_C$, dashed line); J_{\leftarrow} (for $T_L = T_C$ and $T_R = T_H$, solid line) (b) Rectification factor. Parameters: $\omega_1 = 2\pi \times 1$ MHz, $l = 5.25$ μm , $a = 4.76 l$ (25 μm), $\delta_H = -0.02 \Gamma$, and $\delta_C = -0.1 \Gamma$.

with the laser beams (three on each bath) is consistent with the lattice constant and typical waists of Gaussian laser beams [130, 131]. To set the trap distance I fix first the characteristic length $l = \left(\frac{q^2}{4\pi\epsilon_0 m\omega_1^2}\right)^{1/3}$ as the distance for which the Coulomb repulsion of two ions equals the trap potential energy for an ion at a distance l away from the center of its trap. If $a < l$, the Coulomb repulsion of the ions is stronger than the trap confinement which makes the ions jump from their traps. With the parameters used in this section I have $l = 38.7 \mu\text{m}$ and set $a = 1.29 l = 50 \mu\text{m}$. The detunings of the *hot* and *cold* lasers are $\delta_H = -0.02 \Gamma$, and $\delta_C = -0.1 \Gamma$ which gives temperatures $T_H \approx 12$ mK and $T_C \approx 3$ mK. I fix the value $\Delta\omega = 0.5 \omega_1$ for the frequency increment.

The results of the two methods are in very good agreement. In the scale of fig.

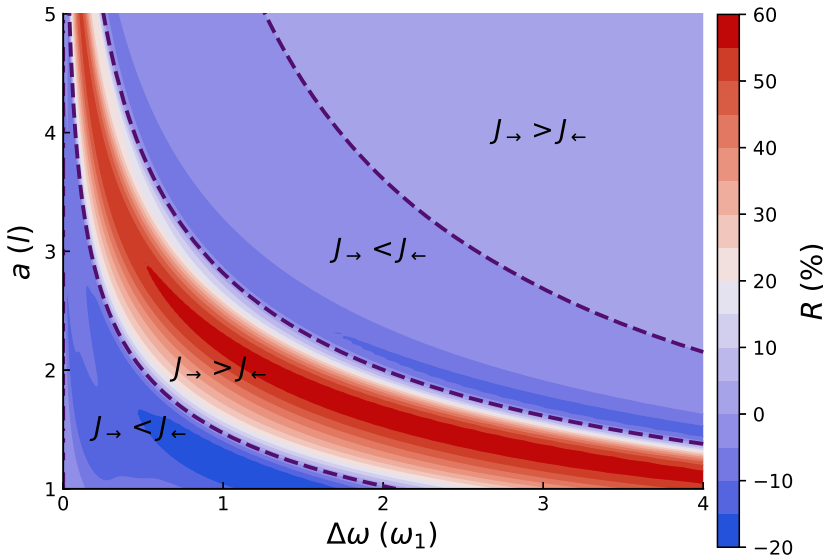


FIGURE 5.4: Rectification factor in a graded chain of $N = 15$ $^{24}\text{Mg}^+$ ions for different trap distances and frequency increment. The dashed lines are for $R = 0$ and delimit the regions $J_{\rightarrow} > J_{\leftarrow}$ and $J_{\rightarrow} < J_{\leftarrow}$. The parameters are $\omega_1 = 2\pi \times 1$ MHz, $l = 5.25$ μm , $\delta_H = -0.02$ Γ , and $\delta_C = -0.1$ Γ .

[5.2](#) (a) the calculated local temperatures are undistinguishable. In the calculation based on solving the dynamics I had to integrate eq. (5.3) for $N_{\text{trials}} = 1000$ realizations of white noise $\xi(t)$. The method based on the system of moments shortened the calculation time with respect to the dynamical trajectories by a factor of 1/700. In fact, the time gain is even more important because the dynamical method requires further processing, performing a time averaging to compute the stationary flux in addition to noise averaging, see fig. 5.2 (b).

Additionally, the relaxation to the steady state slows down when the frequencies of the traps increase since the deterministic part of the Langevin equation dominates the dynamics over the stochastic part, entering an under-damped regime. In contrast, this increase does not affect the algebraic method.

5.3.2 Rectification in frequency graded chains

In this subsection I demonstrate rectification for the frequency graded chain. I used the method described in section [5.2.1](#) for $^{24}\text{Mg}^+$ ions with the same parameters for the baths used before. I fix the trapping frequency of the leftmost trap to $\omega_1 = 2\pi \times 1$ MHz, and a trap spacing $a = 4.76 l$ (25 μm) (the characteristic length is $l = 5.25$ μm). Figure [5.3](#) depicts the results with these parameters in a graded chain. Figure [5.3](#) (a) shows that both J_{\rightarrow} and J_{\leftarrow} decrease rapidly as

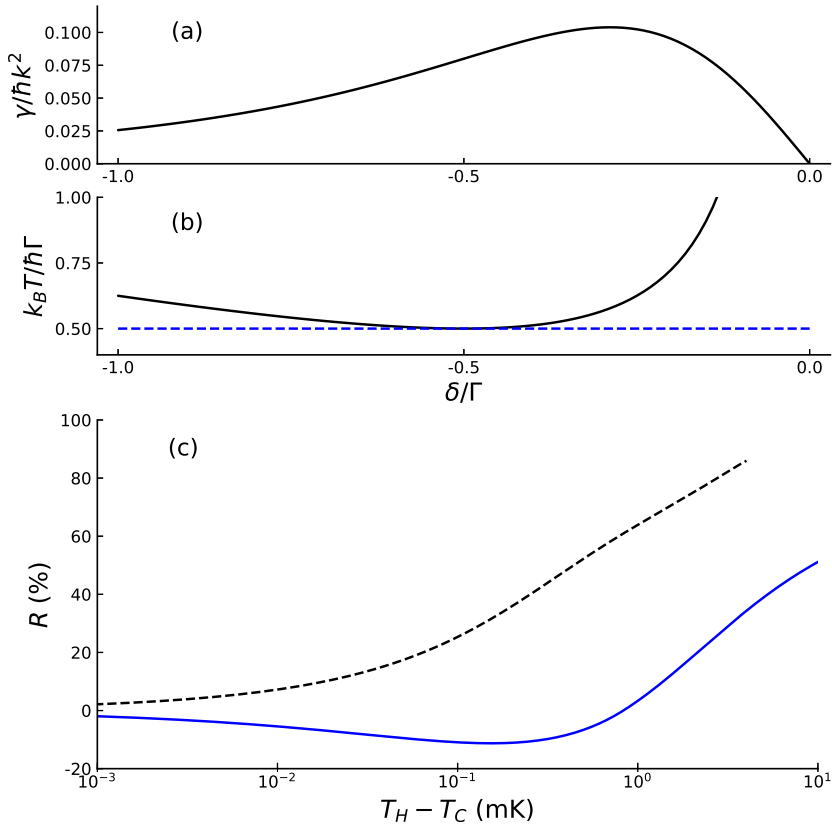


FIGURE 5.5: (a) Friction coefficient defined in eq. (5.4). (b) Bath temperature defined in eq. (5.5). (c) Rectification as a function of the temperature difference between the hot and cold baths $T_H - T_C$ for δ_H below (dashed black line) and above (solid blue line) the Doppler limit, and $\delta_C = \delta_D$ (Doppler limit). Parameters: $\omega_1 = 2\pi \times 1$ MHz, $\Delta\omega = 0.15\omega_1$, $l = 5.25\mu\text{m}$, $a = 4.76l$.

the frequency increment is increased. The rectification reaches its maximum value for a frequency difference of $\Delta\omega \approx 0.1\omega_1$. The fluxes cross so there are some points where the rectification is exactly zero, besides the trivial one at $\Delta\omega = 0$, at $\Delta\omega = 0.05\omega_1$, $0.3\omega_1$, $1.3\omega_1$. At these points the direction of rectification reverses, presumably as a consequence of the changes in the match/mismatch of the temperature dependent local power spectra. The change of rectification direction occurs for all the choices of parameters, as displayed in fig. 5.4. Figure 5.4 gives the rectification factor for different trap distances and frequency increments. 0-rectification curves separate regions with different rectification direction. The second region in fig. 5.4 (starting from the left) would be the most interesting one to build a thermal diode, since rectification reaches its largest values there.

For small values of $\Delta\omega$ there is little asymmetry in the chain and therefore modest rectification is expected whereas a very large $\Delta\omega$ implies very high trapping frequencies on the right implying a too strong confinement and vanishing

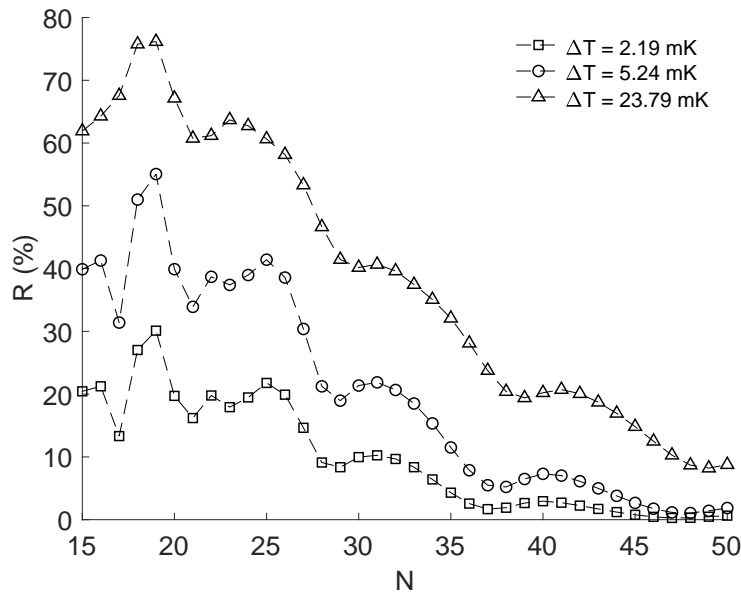


FIGURE 5.6: Rectification factor for different bath temperature differences ΔT as the number of ions is increased. The detuning of the cold bath laser is set to the Doppler limit $\delta_C = -\Gamma/2$. $\omega_1 = 2\pi \times 1$ MHz, $\Delta\omega = 0.15 \omega_1$, $l = 5.25 \mu\text{m}$, $a = 4.76 l$.

interactions. This bottleneck reduces the fluxes in both directions and the rectification. However, since $\Delta\omega$ is controllable, and the range of values of $\Delta\omega$ for which rectification is larger can be also controlled with the intertrap distance a , see fig. 5.4, the existence of a rectification window does not imply a major limitation.

5.3.3 Same bath temperatures, different bath couplings

As already mentioned (below eq. (5.5)), above and below the detuning $\delta_D = -\Gamma/2$ corresponding to the Doppler limit temperature, the optical molasses allow for two different couplings (two pairs of friction and diffusion coefficients in eq. (5.4)) between the ions and the laser corresponding to the same bath temperature. This duality may be seen explicitly in fig. 5.5. Specifically fig. 5.5 (a) depicts the variation of the friction coefficient for values of δ around δ_R , and fig. 5.5 (b) the corresponding temperatures. Interestingly, the different couplings imply different rectification factors. If I set $\delta_C = \delta_D = -\Gamma/2$, i.e., the cold bath is cooled to the Doppler limit, δ_H can be chosen to be below or above δ_D for the same temperature T_H . The corresponding rectification factors for the two choices are shown in fig. 5.5 (c), which demonstrates that significant rectification can be achieved by choosing $\delta_H < \delta_D$ for temperature increments that are smaller than or of the order of

$T_C = T_D$, for example $R \approx 20\%$ for $\Delta T = 0.1T_C$, or $R \approx 60\%$ for $\Delta T = T_C$. Finding good rectification at low (relative) temperature differences is considered to be one on the challenges in asymmetric heat transport research [132].

5.3.4 Dependence with number of ions

Keeping in mind that scaling the frequency-graded ion chain to a large numbers of ions is not a realistic option in this setting, it is nevertheless important to study the dependence with ion number from small to moderate numbers. In fig. 5.6 I observe an overall trend in which the rectification decreases with the number of ions in the chain (while it increases with temperature bias ΔT in the studied range). This effect is easy to understand, as increasing N while keeping the total variation of the trapping frequency $\Delta\omega$ constant, the frequency gradient decreases. This lowers the asymmetry in the chain and the rectification factor. Oscillations with N superimposed to the global trend are more visible for smaller N giving an optimal value at $N = 19$.

5.3.5 Graded versus segmented

I have also compared the performance of the graded thermal diode and a segmented version in which the left half of the chain is trapped with frequency ω_1 and the right half (including the middle ion) with $\omega_1 + \Delta\omega$. Even though the optimal rectification in fig. 5.7 (a) for the segmented chain is larger than for the graded chain, the fact that the fluxes are generally much larger for the graded chain, see fig. 5.7 (b), makes the graded chain more interesting for applications.

5.4 Discussion

In this chapter I have numerically demonstrated heat rectification in a chain of ions trapped in individual microtraps with graded frequencies, connected at both ends to thermal baths created by optical molasses. An alternative to implement a graded frequency profile in the lab could be combining a collective Paul trap for all the ions with on-site dipolar laser forces [106, 133–135].

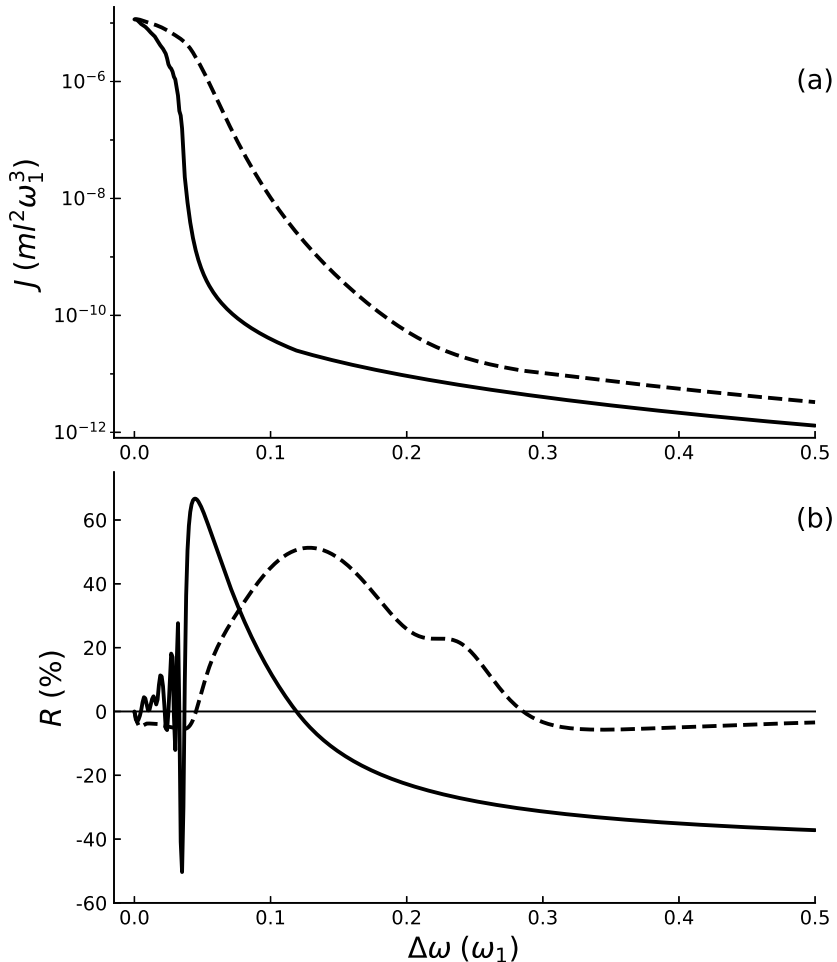


FIGURE 5.7: Comparison of graded and segmented chains with $N = 15$ $^{24}\text{Mg}^+$ ions. (a) Maximum of J_{\rightarrow} and J_{\leftarrow} for the graded and segmented chain for different frequency increments. (b) Rectification factor: graded chain (dashed lines); segmented chain (solid lines). Parameters: $\omega_1 = 2\pi \times 1$ MHz, $l = 5.25$ μm , $a = 4.76 l$, $\delta_H = -0.02 \Gamma$, and $\delta_C = -0.1 \Gamma$.

A goal of this chapter is to connect two communities, ion trappers and researchers on heat-rectification models. The results found are encouraging and demonstrate the potential of a trapped-ion platform to experimentally investigate heat rectification schemes. Trapped ions are quite interesting to this end because they are highly controllable, and may easily adopt several features to enhance rectification, such as the ones explored here (long-range interactions and an asymmetrical gradation), or others such as time-dependent forces [23, 136], or different non-linearities in on-site forces. The limitations and application domain should also be clear, the proposed platform is circumscribed to cold temperatures of the order of hundreds of μK to mK achieved by Doppler cooling. In this sense it is not aimed at competing with (it is rather complementary to) proposals for which

experiments [33–36] or simulations [132, 137, 138] demonstrate thermal rectification at room temperature or for hundreds of K. Also, the number of ions should realistically be kept small so the proposed ion chain is not aimed at achieving a macroscopic diode length, but at playing a role in thermal diode research and in the context of ion-trapped based quantum technologies.

Methodologically, the calculation of the steady state has been performed with an algebraic approach much faster than the time-consuming integration and averaging over noise and time of the dynamical equations. The algebraic approach linearizes the forces around equilibrium positions which, in this system and for the realistic parameters considered is well justified and tested numerically. The results found provide additional evidence that simple linear models may rectify heat flow [55]. I underline that this linear model is, arguably, even simpler than some linear “minimalist, toy models” in [55] that showed rectification (the on-site forces are already linear from the start and the temperature dependence of explicit model parameters is only in the coefficients of the Langevin baths), with the important bonus of being also realistic.

Chapter 6

Thermal rectification with a minimal model of two harmonic oscillators

As previously discussed in the introduction to this part of the Thesis, the presence of thermal rectification in the first models was explained by the temperature dependence of the phonon bands (power spectra) of the different segments of the chain [25, 26]. This temperature dependence of the phonon bands occurs naturally in systems where there are non-linear (anharmonic) interactions, therefore non-linearities have been regarded recurrently as an essential element for rectification [23, 37, 38, 50–54]. However, it was later pointed out by Pereira [55] that anharmonicity is not a necessary condition for rectification, since harmonic systems having some structural symmetry and temperature-dependent parameters can rectify.

In this chapter I put forward a minimal model for rectification composed of two neighboring atoms of different mass interacting harmonically, and in contact with thermal baths with temperature dependent couplings. Asymmetric heat transport is found if both the bath temperatures and the temperature-dependent bath-system couplings are exchanged. The model admits a natural realization in terms of two trapped ions subjected to respective optical molasses, which provide the necessary temperature dependence of the coupling parameters. Apart from the possibility of a physical realization, another interesting feature is the analytical treatment, which facilitates greatly the exploration in parameter space to identify

regimes of maximal rectification. The explicit solution of the stationary regime also provides tools for a better understanding of the physics and enhanced control. For example the match or mismatch of the spectra of the two masses for forward and reverse bias configurations, which will be made evident for the parameters with maximal rectification, may be analyzed in terms of dissipative normal modes characterized by complex eigenvalues.

Segal and Nitzan proposed models with some similarities to the one presented in this chapter [53, 54], specifically an anharmonic chain with different couplings to both baths. They also worked out quantum models [53, 54] in terms of an N -level system asymmetrically coupled to the baths. Both types of models have “harmonic limits”, which in the chain is reached by making the potentials harmonic, and in the quantum one by taking N to infinity assuming equispaced levels. The asymmetrical couplings however, were not interchanged when reversing the temperature bias (in these models that interchange would have suppressed the asymmetry because the forward bias configuration becomes a mirror image of the reverse bias one), so that the harmonic limit did not give any rectification.

The rest of the chapter is organized as follows: In section 6.1, I describe the physical model and its dynamical equations. In section 6.2, I introduce the covariance matrix and derive the equation that it satisfies in the steady state. In section 6.3, I solve the covariance matrix equation and find analytical expressions for the steady-state temperatures of the masses and heat currents. In section 6.4, I relate the parameters of the model to those of Doppler cooled trapped ions. In section 6.5, I look for configurations with high rectification. I also study the power spectra of the oscillators, which confirms the match or mismatch pattern for rectification. Finally, in section 6.6, I summarize the results and present the conclusions.

6.1 Physical Model

The physical model consists of two masses m_1 and m_2 coupled to each other by a harmonic interaction with spring constant k and natural length x_e . The masses m_1 and m_2 are confined by harmonic potentials centered at x_L , x_R with spring constants k_L , k_R respectively (see fig. 6.1). The Hamiltonian describing this model is

$$H = \frac{p_1^2}{2m_1} + \frac{p_2^2}{2m_2} + V(x_1, x_2), \quad (6.1)$$

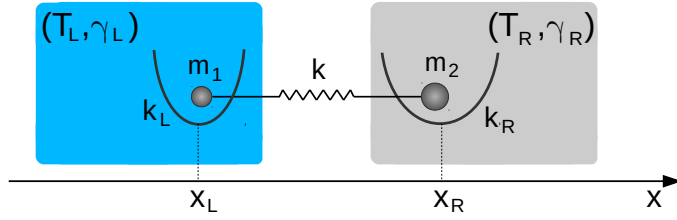


FIGURE 6.1: Diagram of the model described in section 6.1. Two masses are coupled to each other through a spring constant k . Each mass is harmonically trapped and connected to a bath characterized by its temperature T_i and its friction coefficient γ_i .

with $V(x_1, x_2) = \frac{k}{2} (x_1 - x_2 - x_e)^2 + \frac{k_L}{2} (x_1 - x_L)^2 + \frac{k_R}{2} (x_2 - x_R)^2$, where $\{x_i, p_i\}_i$ ($i = 1, 2$) are the position and momentum of each mass. Switching from the original coordinates x_i to displacements with respect to the equilibrium positions of the system $q_i = x_i - x_i^{eq}$, where x_i^{eq} are the solutions to $\partial_{x_i} V(x_1, x_2) = 0$, the Hamiltonian can be written as

$$H = \frac{p_1^2}{2m_1} + \frac{p_2^2}{2m_2} + \frac{k + k_L}{2} q_1^2 + \frac{k + k_R}{2} q_2^2 - k q_1 q_2 + V(x_1^{eq}, x_2^{eq}). \quad (6.2)$$

Dropping the constant term, this has the form of the Hamiltonian of a system around a stable equilibrium point,

$$H = \frac{1}{2} \vec{p}^\top \mathbb{M}^{-1} \vec{p} + \frac{1}{2} \vec{q}^\top \mathbb{K} \vec{q}, \quad (6.3)$$

where $\vec{q} = (q_1, q_2)^\top$, $\vec{p} = (p_1, p_2)^\top$, $\mathbb{M} = \text{diag}(m_1, m_2)$ is the mass matrix of the system and \mathbb{K} is the Hessian matrix of the potential at the equilibrium point, i.e., $\mathbb{K}_{ij} = \partial_{x_i, x_j}^2 V(\vec{x}) \Big|_{\vec{x} = \vec{x}^{eq}}$. In this model $\mathbb{K}_{11} = k + k_L$, $\mathbb{K}_{22} = k + k_R$ and $\mathbb{K}_{12} = \mathbb{K}_{21} = -k$. The generic form (6.3) can be adapted to different physical settings, in particular to two ions in individual traps, or to two ions in a common trap.

The masses are in contact with Langevin baths, which will be denoted as L (for left) and R (for right), at temperatures T_L and T_R for the mass m_1 and m_2 respectively (see fig. 6.1). The equations of motion of the system, taking into

account the Hamiltonian and the Langevin baths are

$$\begin{aligned}\dot{q}_1 &= \frac{p_1}{m_1}, \quad \dot{q}_2 = \frac{p_2}{m_2}, \\ \dot{p}_1 &= -(k + k_L)q_1 + kq_2 - \frac{\gamma_L}{m_1}p_1 + \xi_L(t), \\ \dot{p}_2 &= -(k + k_R)q_2 + kq_1 - \frac{\gamma_R}{m_2}p_2 + \xi_R(t),\end{aligned}\tag{6.4}$$

where γ_L, γ_R are the friction coefficients of the baths and $\xi_L(t), \xi_R(t)$ are Gaussian white-noise-like forces. The Gaussian forces have zero mean over noise realizations ($\langle \xi_L(t) \rangle = \langle \xi_R(t) \rangle = 0$) and satisfy the correlations $\langle \xi_L(t)\xi_L(t') \rangle = 0, \langle \xi_L(t)\xi_R(t') \rangle = 2D_L\delta(t-t'), \langle \xi_R(t)\xi_R(t') \rangle = 2D_R\delta(t-t')$. D_L and D_R are the diffusion coefficients, which satisfy the fluctuation-dissipation theorem, $D_L = \gamma_L k_B T_L, D_R = \gamma_R k_B T_R$, where k_B is the Boltzmann constant.

It is useful to define the phase-space vector $\vec{r}(t) = (\vec{q}, \mathbb{M}^{-1}\vec{p})^\top$ (notice that $\vec{v} = \mathbb{M}^{-1}\vec{p}$ is just the velocity vector). The equations of motion are

$$\dot{\vec{r}}(t) = \mathbb{A} \vec{r}(t) + \mathbb{L} \vec{\xi}(t),\tag{6.5}$$

with

$$\begin{aligned}\mathbb{A} &= \begin{pmatrix} \mathbb{0}_{2 \times 2} & \mathbb{1}_{2 \times 2} \\ -\mathbb{M}^{-1}\mathbb{K} & -\mathbb{M}^{-1}\mathbb{T} \end{pmatrix}, \\ \mathbb{L} &= \begin{pmatrix} \mathbb{0}_{2 \times 2} \\ \mathbb{M}^{-1} \end{pmatrix},\end{aligned}\tag{6.6}$$

and $\vec{\xi}(t) = (\xi_L(t), \xi_R(t))^\top, \mathbb{T} = \text{diag}(\gamma_L, \gamma_R)$. $\mathbb{0}_{n \times n}$ and $\mathbb{1}_{n \times n}$ are the n -dimensional squared 0 matrix and identity matrix respectively. With the vector notation the correlation of the white-noise forces can be written as

$$\left\langle \vec{\xi}(t) \vec{\xi}(t')^\top \right\rangle = 2\mathbb{D}\delta(t-t'),\tag{6.7}$$

where $\mathbb{D} = \text{diag}(D_L, D_R)$.

6.2 Covariance matrix in the steady state

In order to look for the steady-state currents in the system I will make use of the covariance matrix $\mathbb{C}(t)$ which is defined as

$$\mathbb{C}(t) = \langle \vec{r}(t) \vec{r}(t)^T \rangle. \quad (6.8)$$

The relation between the kinetic temperatures of the masses, $T_1(t)$ and $T_2(t)$, and the covariance matrix is given by

$$\begin{aligned} T_1(t) &\equiv \frac{\langle p_1^2(t) \rangle}{m_1 k_B} = \frac{m_1 C_{3,3}(t)}{k_B}, \\ T_2(t) &\equiv \frac{\langle p_2^2(t) \rangle}{m_2 k_B} = \frac{m_2 C_{4,4}(t)}{k_B}. \end{aligned} \quad (6.9)$$

As discussed in section 5.2.1, the covariances of the positions and velocities of the masses could be calculated integrating eq. (6.5) over an ensemble of noise realizations $\vec{\xi}(t)$ and taking the corresponding expectation values in the steady state. However, in section 5.2.1 it was pointed out the tremendous cost of doing this, so I introduced a way to linearize the system that let us find the steady-state covariances as the solutions for a set of algebraic equations [123–125]. In this case the system dynamics are already linear, so I can directly use the steady-state method described in 5.2.1. Besides, the solutions of the steady-state equations will be analytical for this two oscillators model.

To begin, I differentiate $\mathbb{C}(t)$ with respect to time and use eq. (6.5) to get

$$\begin{aligned} \frac{d}{dt} \mathbb{C}(t) &= \mathbb{A} \mathbb{C}(t) + \mathbb{C}(t) \mathbb{A}^T \\ &+ \mathbb{L} \left\langle \vec{\xi}(t) \vec{r}(t)^T \right\rangle + \left\langle \vec{r}(t) \vec{\xi}(t)^T \right\rangle \mathbb{L}^T. \end{aligned} \quad (6.10)$$

The solution of eq. (6.10) can be used to find the kinetic temperatures of the masses at all times but I am only interested in the steady-state values, *i.e.* the asymptotic values for $t \rightarrow \infty$. In the steady state, the covariance matrix is constant ($\frac{d}{dt} \mathbb{C}(t) = 0$), therefore it satisfies

$$\mathbb{A} \mathbb{C}^{s.s.} + \mathbb{C}^{s.s.} \mathbb{A}^T = -\mathbb{L} \left\langle \vec{\xi} \vec{r}^T \right\rangle^{s.s.} - \left\langle \vec{r} \vec{\xi}^T \right\rangle^{s.s.} \mathbb{L}^T, \quad (6.11)$$

with $\{\cdot\}^{s.s.} \equiv \lim_{t \rightarrow \infty} \{\cdot\}(t)$. The two terms $\langle \vec{\xi} \vec{r}^\top \rangle^{s.s.}$ and $\langle \vec{r} \vec{\xi}^\top \rangle^{s.s.}$ in (6.11) can be calculated using Novikov's theorem [119] as explained in section 5.2,

$$\langle \vec{\xi}(t) \vec{r}(t)^\top \rangle = \mathbb{D}\mathbb{L}^\top. \quad (6.12)$$

I have therefore, the following algebraic equation for the steady-state covariance matrix

$$\mathbb{A}\mathbb{C}^{s.s.} + \mathbb{C}^{s.s.}\mathbb{A}^\top = -\mathbb{B}, \quad (6.13)$$

with $\mathbb{B} = 2\mathbb{L}\mathbb{D}\mathbb{L}^\top$. By definition, the covariance matrix is symmetric, but there are also additional restrictions imposed by the equations of motion and the steady-state condition, which reduce the dimensionality of the problem of solving eq. (6.13) [57]. Since $d\langle q_i q_j \rangle / dt = 0$ in the steady state, I have

$$\begin{aligned} \langle p_1 q_1 \rangle^{s.s.} &= \langle p_2 q_2 \rangle^{s.s.} = 0, \\ \frac{\langle p_1 q_2 \rangle^{s.s.}}{m_1} &= -\frac{\langle q_1 p_2 \rangle^{s.s.}}{m_2}. \end{aligned} \quad (6.14)$$

Taking (6.14) into account, the steady-state covariance matrix takes the form

$$\mathbb{C}^{s.s.} = \begin{pmatrix} \langle q_1^2 \rangle^{s.s.} & \langle q_1 q_2 \rangle^{s.s.} & 0 & \frac{\langle p_2 q_1 \rangle^{s.s.}}{m_2} \\ \langle q_1 q_2 \rangle^{s.s.} & \langle q_2^2 \rangle^{s.s.} & -\frac{\langle p_2 q_1 \rangle^{s.s.}}{m_2} & 0 \\ 0 & -\frac{\langle p_2 q_1 \rangle^{s.s.}}{m_2} & \frac{\langle p_1^2 \rangle^{s.s.}}{m_1^2} & \frac{\langle p_1 p_2 \rangle^{s.s.}}{m_1 m_2} \\ \frac{\langle p_2 q_1 \rangle^{s.s.}}{m_2} & 0 & \frac{\langle p_1 p_2 \rangle^{s.s.}}{m_1 m_2} & \frac{\langle p_2^2 \rangle^{s.s.}}{m_2^2} \end{pmatrix}. \quad (6.15)$$

The explicit set of equations for the components of $\mathbb{C}^{s.s.}$ can be found in Appendix C.

6.3 Solutions

In this section I use the solution to eq. (6.13) to write down the temperatures and currents in the steady state. I use the software *Mathematica* to find analytic expressions for the temperatures,

$$\begin{aligned} T_1 &= \frac{T_L \mathcal{P}_{1,L}(k) + T_R \mathcal{P}_{1,R}(k)}{\mathcal{D}(k)}, \\ T_2 &= \frac{T_L \mathcal{P}_{2,L}(k) + T_R \mathcal{P}_{2,R}(k)}{\mathcal{D}(k)}, \end{aligned} \quad (6.16)$$

where $\mathcal{D}(k) = \sum_{n=0}^2 \mathcal{D}_n k^n$ and $\mathcal{P}_{i,(L/R)}(k) = \sum_{n=0}^2 a_{i,n,(L/R)} k^n$ are polynomials in the coupling constant k with coefficients

$$\begin{aligned}
 \mathcal{D}_0 &= a_{1,0,L} = a_{2,0,R} \\
 &= \gamma_L \gamma_R [h^{(1)}(\gamma_L k_R + \gamma_R k_L) + (m_1 k_R - m_2 k_L)^2], \\
 \mathcal{D}_1 &= a_{1,1,L} = a_{2,1,R} \\
 &= \gamma_L \gamma_R [h^{(0)} h^{(1)} + 2(m_1 - m_2)(m_1 k_R - m_2 k_L)], \\
 \mathcal{D}_2 &= h^{(0)} h^{(2)}, \\
 a_{1,2,L} &= \gamma_L (m_2 h^{(1)} + \gamma_R (m_1 - m_2)^2), \\
 a_{1,2,R} &= h^{(1)} m_1 \gamma_R, \\
 a_{2,2,L} &= h^{(1)} m_2 \gamma_L, \\
 a_{2,2,R} &= \gamma_R (m_1 h^{(1)} + \gamma_L (m_1 - m_2)^2), \\
 a_{1,0,R} &= a_{1,1,R} = a_{2,0,L} = a_{2,1,L} = 0,
 \end{aligned} \tag{6.17}$$

where

$$h^{(n)} \equiv \gamma_R m_1^n + \gamma_L m_2^n. \tag{6.18}$$

The currents from the baths to the masses are given by eq. (5.14)

$$J_L = k_B \frac{\gamma_L}{m_1} (T_L - T_1), \quad J_R = k_B \frac{\gamma_R}{m_2} (T_R - T_2), \tag{6.19}$$

with T_i given by eq. (6.16). Since, in the steady state, $J_L = -J_R$, the shorthand notation $J \equiv J_L$ will be used. Substituting eq. (6.16) into eq. (6.19), the heat current is

$$J = \kappa (T_L - T_R), \tag{6.20}$$

where $\kappa = k_B k^2 \gamma_L \gamma_R h^{(1)} / \mathcal{D}(k)$ acts as an effective thermal conductance.

6.4 Relation of the Model to a trapped ion setup

In this section I discuss the realization of the model with a pair of trapped ions. I consider two different setups: two ions in a collective trap, and two ions in individual traps. Later in section 6.5 I shall focus on two ions in individual traps to illustrate the analysis of rectification.

In both setups I assume strong confinement in the radial direction, making the effective dynamics one-dimensional. I will also assume that the confinement in the axial direction is purely electrostatic, which makes the effective spring constant independent of the mass of the ions [139]. Additionally, I will relate the temperatures and friction coefficients of the Langevin baths to those corresponding to Doppler cooling.

6.4.1 Collective trap

Consider two ions of unit charge with masses m_1 and m_2 trapped in a collective trap. Assuming strong radial confinement and purely electrostatic axial confinement, both ions feel the same harmonic oscillator potential with trapping constant k_{trap} [139]. The potential describing the system is

$$V_{\text{collective}} = \frac{1}{2}k_{trap}(x_1^2 + x_2^2) + \frac{\mathcal{C}}{x_2 - x_1}, \quad (6.21)$$

with $\mathcal{C} = Q^2/(4\pi\varepsilon_0)$. The equilibrium positions for this potential are

$$x_2^{eq} = -x_1^{eq} = \left(\frac{1}{2}\right)^{2/3} \left(\frac{Q^2}{4\pi\varepsilon_0 k_{trap}}\right)^{1/3}. \quad (6.22)$$

Assuming small oscillations of the ions around the equilibrium positions, the Hessian matrix of the system is

$$\begin{aligned} \mathbb{K}_{1,2} &= -\frac{Q^2}{2\pi\varepsilon_0} \frac{1}{(x_2^{eq} - x_1^{eq})^3} = -k_{trap}, \\ \mathbb{K}_{1,1} &= k_{trap} + \frac{Q^2}{2\pi\varepsilon_0} \frac{1}{(x_2^{eq} - x_1^{eq})^3} = 2k_{trap}, \\ \mathbb{K}_{2,2} &= k_{trap} + \frac{Q^2}{2\pi\varepsilon_0} \frac{1}{(x_2^{eq} - x_1^{eq})^3} = 2k_{trap}. \end{aligned} \quad (6.23)$$

Using eq. (6.23) I can relate the parameters of this physical setup to those of the model described in section 6.1,

$$k_L = k_R = k = k_{trap}. \quad (6.24)$$

6.4.2 Individual on-site traps

I can make the same assumptions for the axial confinement as in the previous subsection but now each of the ions is in an individual trap with spring constants $k_{trap,L}$ and $k_{trap,R}$ respectively. The potential of the system is

$$\begin{aligned} V_{individual} = & \frac{1}{2}k_{trap,L}(x_1 - x_L)^2 + \frac{1}{2}k_{trap,R}(x_2 - x_R)^2 \\ & + \frac{\mathcal{C}}{x_2 - x_1}, \end{aligned} \quad (6.25)$$

where x_L and x_R are the center positions of the on-site traps. The elements of the Hessian matrix in the equilibrium position are

$$\begin{aligned} \mathbb{K}_{1,2} &= -\frac{Q^2}{2\pi\varepsilon_0} \frac{1}{(x_2^{eq} - x_1^{eq})^3}, \\ \mathbb{K}_{1,1} &= k_{trap,L} + \frac{Q^2}{2\pi\varepsilon_0} \frac{1}{(x_2^{eq} - x_1^{eq})^3}, \\ \mathbb{K}_{2,2} &= k_{trap,R} + \frac{Q^2}{2\pi\varepsilon_0} \frac{1}{(x_2^{eq} - x_1^{eq})^3}. \end{aligned} \quad (6.26)$$

Comparing the parameters in eq. (6.26) with those in the model described in section 6.1 I identify

$$\begin{aligned} k_L &= k_{trap,L}, \\ k_R &= k_{trap,R}, \\ k &= \frac{Q^2}{2\pi\varepsilon_0} \frac{1}{(x_2^{eq} - x_1^{eq})^3}. \end{aligned} \quad (6.27)$$

In this case, the analytic expressions for the equilibrium positions are more complicated. I get for the distance between the equilibrium positions of the ions

$$(x_2 - x_1)^{(eq)} = \frac{1}{3} \Delta x_{LR} \\ - \frac{1}{6} \left[\frac{2^{2/3} \zeta}{k_{trap,L} k_{trap,R} (k_{trap,L} + k_{trap,R})} \right. \\ \left. + \frac{2^{4/3} k_{trap,L} k_{trap,R} (k_{trap,L} + k_{trap,R}) (x_R - x_L)^2}{\zeta} \right], \quad (6.28)$$

where $\Delta x_{LR} = (x_R - x_L)$ and $\zeta = (Y - \eta)^{(1/3)}$, with

$$Y = 3\sqrt{3} \left\{ C k_{trap,L}^4 k_{trap,R}^4 (k_{trap,L} + k_{trap,R})^7 \right. \\ \times \left[4k_{trap,L} k_{trap,R} \Delta x_{LR}^3 + 27C (k_{trap,L} + k_{trap,R}) \right] \left. \right\}^{1/2}, \\ \eta = k_{trap,L}^2 k_{trap,R}^2 (k_{trap,L} + k_{trap,R})^3 \\ \times [2k_{trap,L} k_{trap,R} \Delta x_{LR}^3 + 27C (k_{trap,L} + k_{trap,R})]. \quad (6.29)$$

In this setup, the coupling between the ions k can be controlled by changing the distance between the on-site traps.

6.4.3 Optical molasses and Langevin baths

As discussed in section 5.1, the Langevin dynamics can be implemented in a trapped-ion setup with the technique of optical molasses [116, 117, 140, 141]. The damping-like force in the Langevin equation comes from the absorption of the photons by the ions, while the diffusive force ($\vec{\xi}(t)$) is originated by the random recoil of the ions when they emit photons. To recall what was explained in 5.1, the effect of the optical molass amounts to having an effective temperature T_{molass} and effective friction coefficient γ_{molass} which are controlled with the laser intensity I and frequency detuning δ with respect to the selected internal atomic transition. The following expressions describe the molass effect [107, 116, 117]

$$\gamma_{molass}(I, \delta) = -4\hbar \left(\frac{\delta + \omega_0}{c} \right)^2 \left(\frac{I}{I_0} \right) \frac{2\delta/\Gamma}{[1 + (2\delta/\Gamma)^2]^2}, \\ T_{molass}(\delta) = -\frac{\hbar\Gamma}{4k_B} \frac{1 + (2\delta/\Gamma)^2}{(2\delta/\Gamma)}, \quad (6.30)$$

where ω_0 is the frequency of the selected internal atomic transition of the ion, Γ is the natural width (decay rate) of the excited state, and I_0 is the saturation intensity. For fixed Γ and I , γ_{molass} depends on δ , and thus, indirectly, on the temperature T_{molass} .

6.5 Looking for rectification

There is rectification if the flux J for the forward temperature bias is different from the flux \tilde{J} for reverse bias with the baths exchanged. To measure rectification, I will use the rectification coefficient $0 \leq R \leq 1$ defined as

$$R \equiv \frac{\left| |J| - |\tilde{J}| \right|}{\max(|J|, |\tilde{J}|)} = 1 - \min \left(\frac{\kappa}{\tilde{\kappa}}, \frac{\tilde{\kappa}}{\kappa} \right), \quad (6.31)$$

where $\kappa, \tilde{\kappa}$ are the heat conductance in the forward and reversed (after the baths are exchanged) configurations. The important point here is to define what is meant by *exchanging the baths*. In the following I will consider that a bath is characterized, not only by its temperature T but also by its coupling to the system by means of the friction coefficient γ , so, exchanging the baths is achieved by exchanging both the temperatures and the friction coefficients, as summarized in Table 6.1. For generic models this choice is a matter of definition, but for trapped ions it is a natural way to proceed.

When implementing temperatures and friction coefficients by lasers according to eq. (6.30), the exchange operation is straightforward when the two ions are either of the same species or isotopes of each other, since the only required action to exchange temperatures is to exchange the detunings without modifying the intensities. The detuning exchange, in turn, automatically exchanges the friction coefficients. However, for two different species, which involve two different atomic transitions, the laser wavelengths and the decay rates Γ depend on the species. Then, exchanging the temperatures by modifying the detunings, keeping the laser intensities constant, does not necessarily imply an exchange of the friction coefficients. Nevertheless it is possible to adjust the laser intensities so that the friction coefficients get exchanged and this is the assumption hereafter. In terms of the analysis of rectification in ref. [55], I am adding a temperature-dependent feature

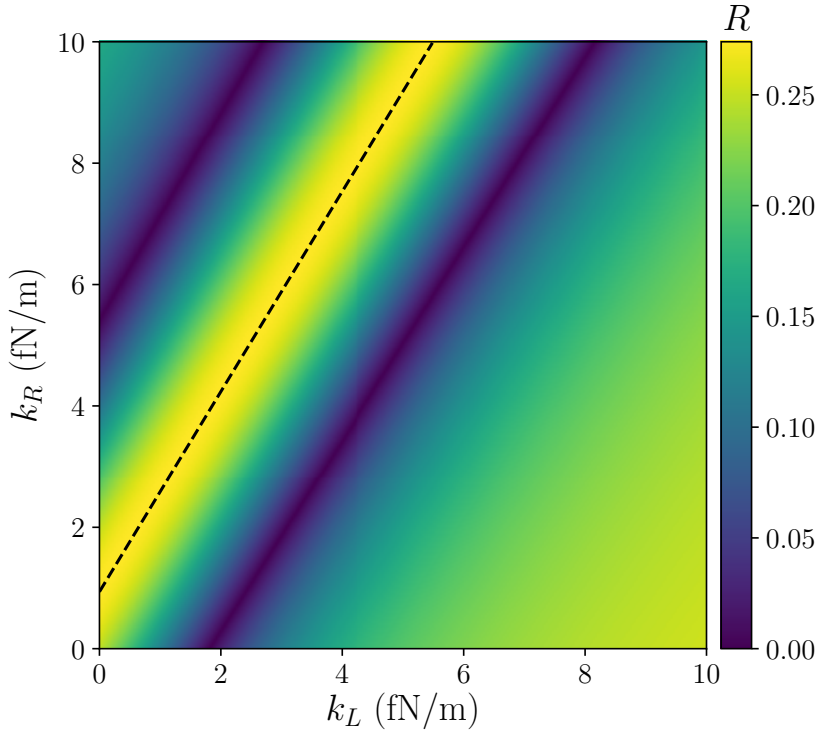


FIGURE 6.2: Rectification, R , in the $k_L k_R$ plane for $k = 1.17$ fN/m, $\gamma_L = 6.75 \times 10^{-22}$ kg/s, and $\gamma_R = 4.64\gamma_L$, $m_1 = 24.305$ a.u., $m_2 = 40.078$ a.u. The dashed line represents eq. (6.32).

TABLE 6.1: Definition of forward and reversed (exchanged) bath configurations. The variables with a tilde are the ones for the “reversed” configuration.

	forward	reversed
Bath Friction	γ_L, γ_R	$\tilde{\gamma}_L = \gamma_R, \tilde{\gamma}_R = \gamma_L$
Bath Temperature	T_L, T_R	$\tilde{T}_L = T_R, \tilde{T}_R = T_L$

to the system, namely, the friction coefficients depend on the bath temperature and are exchanged as the baths are reversed.

6.5.1 Parametric exploration

I have explored thoroughly the space formed by the parameters of the model $m_1, m_2, k, k_L, k_R, \gamma_L, \gamma_R$, to find and maximize asymmetric heat transport. I have fixed the values of some of the parameters to realistic ones while varying the rest. Unless stated otherwise the masses are $m_1 = 24.305$ a.u. and $m_2 = 40.078$ a.u., which correspond to Mg and Ca, whose ions are broadly used in trapped-ion physics. According to eqs. (6.20) and (6.31), R does not formally depend on the bath temperatures in this model for given friction coefficients. Of course,

the friction coefficients depend on the temperature indirectly, but also on laser intensities, see eq. (6.30), so in the parametric space $m_1, m_2, k, k_L, k_R, \gamma_L, \gamma_R$ there is no need to specify the bath temperatures to analyze the rectification in the following. The bath temperatures will be needed though to calculate the power spectra, and play an implicit role in the central assumption that their exchange implies an exchange of friction coefficients.

Figure 6.2 depicts the values of the rectification after sweeping the $k_L k_R$ plane for fixed values of k, γ_L , and γ_R . There is a ridge in the k_L, k_R plane for which the rectification is maximal, and can be found by solving $\partial_{k_L} R = 0$. In a weak dissipation regime ($\gamma_L/m_1 \ll \sqrt{k/m_1}, \gamma_R/m_2 \ll \sqrt{k/m_2}$), a Taylor series around $(\gamma_L, \gamma_R) = (0, 0)$ gives in zeroth order a straight line for the ridge,

$$\frac{k + k_R}{m_2} = \frac{k + k_L}{m_1}. \quad (6.32)$$

eq. (6.32) implies the resonance condition $\omega_L = \omega_R$ for the effective oscillation frequencies $\omega_L = \sqrt{(k + k_L)/m_1}$ and $\omega_R = \sqrt{(k + k_R)/m_2}$, see eq. (6.2). The lowest order correction to eq. (6.32) implies a small shift of the line, keeping the same slope,

$$\frac{k + k_R}{m_2} = \frac{k + k_L}{m_1} + \frac{(m_2 \gamma_L + m_1 \gamma_R)(m_1 \gamma_L + m_2 \gamma_R)}{2m_1 m_2 (m_2^2 - m_1^2)}. \quad (6.33)$$

In a trapped-ion context the condition (6.32) may be imposed by adjusting the distance of the traps for fixed k_L and k_R . Besides the line of maximum rectification, fig. 6.2 also shows two lines where rectification is zero. At these lines forward and backward fluxes cross. Solving $R = 0$ with a Taylor series around $(\gamma_L, \gamma_R) = (0, 0)$ gives, up to second order in friction coefficients, the two approximate solutions

$$\begin{aligned} k_R = k_L & \left[\frac{m_2}{m_1} \pm \frac{1}{2k} \sqrt{\frac{m_2 \gamma_L \gamma_R^3}{m_1^3}} \right] \\ & + k \left[\frac{m_2}{m_1} \left(1 \pm \frac{2m_1 m_2 \gamma_R + (m_1^2 + m_2^2) \gamma_L}{2\sqrt{m_1 m_2^3 \gamma_L \gamma_R}} \right) - 1 \right] \\ & \pm \frac{1}{2} \sqrt{\frac{m_2 \gamma_L \gamma_R^3}{m_1^3}} + \gamma_R \frac{(m_1^2 + m_2^2) \gamma_L + m_1 m_2 \gamma_R}{2m_1^2 (m_2 - m_1)}. \end{aligned} \quad (6.34)$$

The term $\pm \frac{1}{2k} \sqrt{m_2 \gamma_L \gamma_R^3 / m_1^3}$ in eq. (6.34) makes the slopes of the two zero-rectification lines different from each other and also from the maximum-rectification

line. However, this difference is hardly noticeable for weak dissipation as in fig. 6.2.

Interestingly, along the maximum line (6.32) the rectification no longer depends on the spring constants of the model, see eqs. (6.20) and (6.31),

$$R = \begin{cases} 1 - \frac{a+g}{1+ag} & \text{if } a > 1, g > 1 \text{ or } a < 1, g < 1 \\ 1 - \frac{1+ag}{a+g} & \text{if } a > 1, g < 1 \text{ or } a < 1, g > 1, \end{cases} \quad (6.35)$$

it only depends on the mass and friction coefficient ratios a and g

$$a = m_2/m_1, \quad g = \gamma_R/\gamma_L. \quad (6.36)$$

Besides a high value of R , it is desirable to have a significant current J_{max} [57]. Using again eq. (6.32) in the expression for the currents (6.20), the maximum current $J_{max} = \max(|J|, |\tilde{J}|)$ is

$$J_{max} = \begin{cases} \frac{k_B g \gamma_L k^2 |T_L - T_R|}{(a+g)(g\gamma_L^2(k_L+k)+k^2m_1)} & \text{if } \begin{cases} a > 1, g > 1 \\ \text{or } a < 1, g < 1 \end{cases} \\ \frac{k_B g \gamma_L k^2 |T_L - T_R|}{(1+ag)(g\gamma_L^2(k_L+k)+k^2m_1)} & \text{if } \begin{cases} a > 1, g < 1 \\ \text{or } a < 1, g > 1 \end{cases} \end{cases} \quad (6.37)$$

Now let us analyze how the parameters a and g affect the maximum current J_{max} in (6.37). To do this, I divide the ag plane in four quadrants by the axes $a = 1$ and $g = 1$ (in those axes $R = 0$). In eq. (6.37) the parameter a appears only in the denominator, thus for a higher a , a smaller current is found. The quadrants with $a < 1$ will be better for achieving large currents. g appears both in the numerator and denominator so there is no obvious advantageous quadrant for this parameter.

Equation (6.35) is symmetric upon the transformations $a \leftrightarrow 1/a$ and $g \leftrightarrow 1/g$. Using a logarithmic scale for a and g , the resulting R map is symmetric with respect to the $a = 1$ and $g = 1$ axes. I can thus limit to analyze the quadrant $a > 1, g > 1$.

Figure 6.3(a) shows the rectification given by eq. (6.35) in terms of a and g . If one follows the direction of the gradient vector of R , $\vec{\nabla} R \equiv (\partial_a R, \partial_g R)$, which is indicated in fig. 6.3 by the black arrows, it becomes clear that the fastest way of increasing R is following the diagonal dotted line $a = g$. Therefore I decided

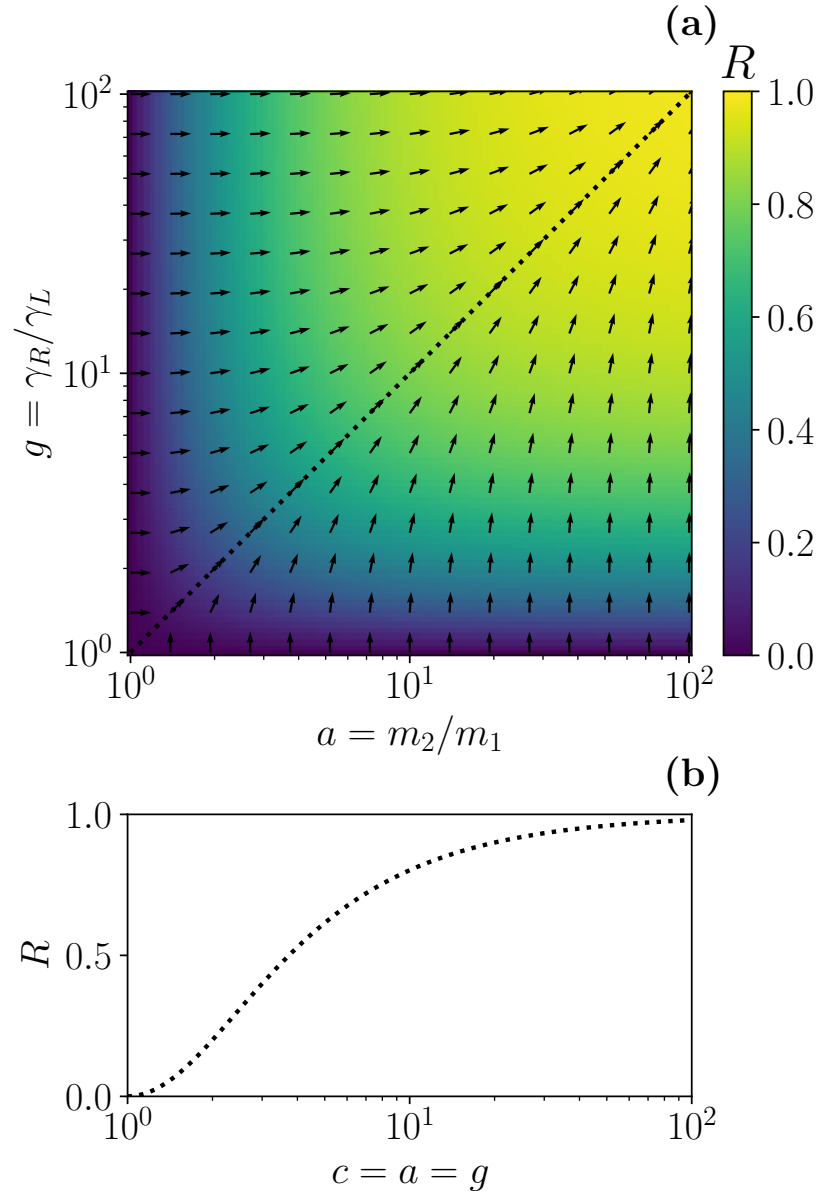


FIGURE 6.3: (a) Rectification factor, R , given by eq. (6.35) as a function of the mass and friction ratios a and g . (b) Rectification factor along the diagonal dotted line $a = g$ in (a).

to vary a and g following a common value $c = a = g$. The effect of varying the common value c may be seen in fig. 6.3(b), which shows the rectification. As can be seen in fig. 6.3(b) the rectification increases when the mass and friction ratios increase (R tends to one for large c).

6.5.2 Spectral match/mismatch approach to rectification

If there is a good match between the phonon spectra of the ions (i.e., their peaks overlap in a broad range of frequencies) for a certain baths configuration, and mismatch when the baths exchange, the system will present heat rectification [25, 26]. I have studied the phonon spectra of the model for several sets of parameters exhibiting no rectification or strong rectification. The spectra are calculated through the spectral density matrix. For a real-valued stochastic process $\vec{x}(t)$, its spectral density matrix is defined as [123]

$$\mathbb{S}_{\vec{x}}(\omega) \equiv \left\langle \vec{X}(\omega) \vec{X}^T(-\omega) \right\rangle, \quad (6.38)$$

with $\vec{X}(\omega)$ being the Fourier transform of $\vec{x}(t)$ (I use the convention of factors of 1 and $1/(2\pi)$ for the transform and the inverse transform). A justification of the use of the spectral density matrix to understand heat transport arises from the Wiener-Khinchin theorem [123], which says that the correlation matrix of a stationary stochastic process in the steady state is the inverse Fourier transform of its spectral density matrix $\langle \vec{r}(t) \vec{r}^T(t + \tau) \rangle = \mathcal{F}^{-1}[\mathbb{S}_{\vec{r}}(\omega)](\tau)$. Thus the covariance matrix in the steady state is

$$\mathbb{C}^{s.s.} = \frac{1}{2\pi} \int_{-\infty}^{\infty} d\omega \mathbb{S}_{\vec{r}}(\omega). \quad (6.39)$$

Equation (6.39) directly connects the spectral density matrix to the steady-state temperature since $T_1^{s.s.} = m_1 C_{3,3}^{s.s.}/k_B$ and $T_2^{s.s.} = m_2 C_{4,4}^{s.s.}/k_B$, and, therefore, to the heat currents, see eqs.(6.9) and (6.19).

The Fourier transform of the vector process $\vec{r}(t)$ describing the evolution of the system, see eq. (6.5), is $\vec{R}(\omega) = (i\omega - \mathbb{A})^{-1} \mathbb{L} \vec{\Xi}(\omega)$ with $\vec{\Xi}(\omega)$ being the Fourier transform of the white noise $\vec{\xi}(t)$. Notice that $\vec{\Xi}(\omega)$ is not square-integrable, however its spectral density is $\mathbb{S}_{\vec{\xi}}(\omega) = 2\mathbb{D}$ [123], which is flat as expected for a white noise. Therefore, the spectral density matrix of the system is

$$\mathbb{S}_{\vec{r}}(\omega) = 2(\mathbb{A} - i\omega)^{-1} \mathbb{L} \mathbb{D} \mathbb{L}^T (\mathbb{A} + i\omega)^{-T}. \quad (6.40)$$

The imaginary part of the eigenvalues of the dynamical matrix \mathbb{A} correspond to the peaks in the spectrum whereas the real part dictates their width. Equation (6.40) gives after direct computation

$$\mathbb{S}_{\vec{r}}(\omega) = 2k_B \frac{\gamma_L T_L \mathbb{S}_L(i\omega) + \gamma_R T_R \mathbb{S}_R(i\omega)}{(m_1 m_2)^2 P_{\mathbb{A}}(i\omega) P_{\mathbb{A}}(-i\omega)}, \quad (6.41)$$

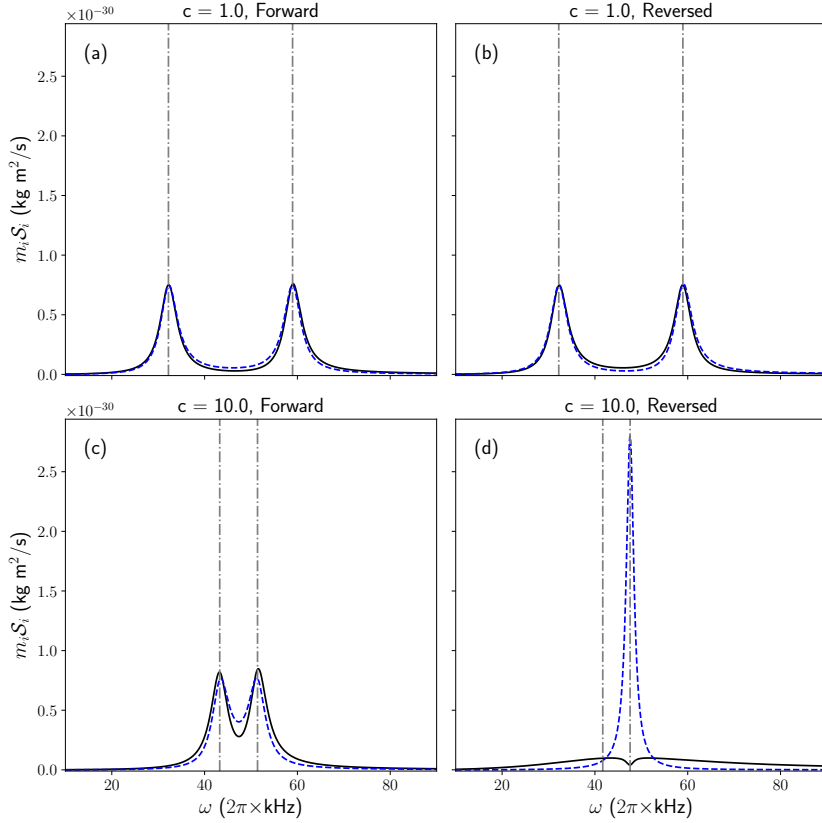


FIGURE 6.4: Spectral densities of the velocities of the ions (r_3 and r_4) corresponding to $T_L = \tilde{T}_R = 2$ mK, $T_R = \tilde{T}_L = 1$ mK, and two values of c in fig. 6.3(b): (a), (b) for $c = 1$ and (c), (d) for $c = 10$. Solid, black lines are for the left ion spectral density $\mathcal{S}_1(\omega)$ and dashed, blue lines for the right ion spectral density $\mathcal{S}_2(\omega)$. Dot-dashed, vertical lines mark the frequencies of the normal modes of the system. The spectra are multiplied by their corresponding masses so that the areas are proportional to the steady-state temperatures, see eq. (6.39). (a) and (b) correspond to $R = 0$: the overlap between the phonon bands is the same in forward and reversed configurations. (c) and (d) correspond to $R \approx 0.8$: in the forward configuration (c) the phonons match better than in the reversed configuration (d).

where $P_{\mathbb{A}}(\lambda)$ is the characteristic polynomial of the dynamical matrix \mathbb{A} and $\mathbb{S}_L(\omega)$, $\mathbb{S}_R(\omega)$ are the matrix polynomials in the angular frequency ω whose coefficients are defined in Appendix D. I show the spectral densities for the velocities, $\mathcal{S}_1 \equiv \mathbb{S}_{3,3}(\omega) = \langle R_3(\omega)R_3(-\omega) \rangle$ for the left ion, and $\mathcal{S}_2 \equiv \mathbb{S}_{4,4}(\omega) = \langle R_4(\omega)R_4(-\omega) \rangle$ for the right ion, since they are the elements related to the calculation of the heat

current using eq. (6.39),

$$\begin{aligned}\mathcal{S}_1(\omega) &= 2k_B \frac{\gamma_R k^2 T_R \omega^2 + \gamma_L T_L [\omega^4 (\gamma_R^2 - 2km_2 - 2k_R m_2) + \omega^2(k + k_R)^2 + m_2^2 \omega^6]}{(m_1 m_2)^2 P_{\mathbb{A}}(i\omega) P_{\mathbb{A}}(-i\omega)}, \\ \mathcal{S}_2(\omega) &= 2k_B \frac{\gamma_L k^2 T_L \omega^2 + \gamma_R T_R [\omega^4 (\gamma_L^2 - 2km_1 - 2k_L m_1) + \omega^2(k + k_L)^2 + m_1^2 \omega^6]}{(m_1 m_2)^2 P_{\mathbb{A}}(i\omega) P_{\mathbb{A}}(-i\omega)}.\end{aligned}\quad (6.42)$$

Figure 6.4 depicts a series of plots of the spectra given by eq. (6.42), corresponding to two points in fig. 6.3(b). (The calculation for the reverse bias is done with the substitutions in Table 6.1.) For $c = 1$ (fig. 6.4(a) and (b)) there is no rectification, since the spectra match in the forward (a) and reversed (b) configurations. However, for $c = 10$ (fig. 6.4(c) and (d), $R \approx 0.8$) the picture is very different: there is a good match between the spectra in the forward configuration but not for the reversed configuration. It is interesting to analyze how the system changes from $c = 1$ to $c = 10$ (see fig. 6.5) using the dissipative normal modes of the system, which may be found by diagonalizing the dynamical matrix \mathbb{A} , eq. (6.6). The frequencies of the peaks in fig. 6.4 are given by the imaginary part of the eigenvalues $\lambda_{\mathbb{A}} = \lambda_r + i\lambda_i$ of \mathbb{A} . Likewise, the width depends on the real part of the eigenvalues. For the forward configuration, the normal frequencies (position of the peaks) come closer to each other as c is increased, while the widths remain practically constant. To understand why the real part remains practically constant, recall that I have chosen to work with spring constants that satisfy eq. (6.32) and making the mass and friction coefficient ratios equal to c , *i.e.*, $c \equiv m_2/m_1 = \gamma_R/\gamma_L$. The (dissipative) terms in \mathbb{A} responsible for the real parts in the eigenvalues are, for the forward configuration, γ_L/m_1 and $\gamma_R/m_2 = (c\gamma_L)/(cm_1) = \gamma_L/m_1$, which are constant for every value of c . On the contrary, in the reverse bias configuration the dissipative terms in the dynamical matrix are $\tilde{\gamma}_L/m_1 = \gamma_R/m_1 = c\gamma_L/m_1$ and $\tilde{\gamma}_R/m_2 = \gamma_L/(cm_1)$, with opposite behavior with respect to c . The real parts of the eigenvalues also behave quite differently for reverse bias, one of them gets closer to the imaginary axis for $c = 10$, see fig. 6.4 (d), where this mode concerns mostly the right ion, the only one excited at the peak frequency, while the other eigenvalue moves far from the imaginary axis so a peak is not noticeable at the imaginary value (left dotted-dashed line) any more.

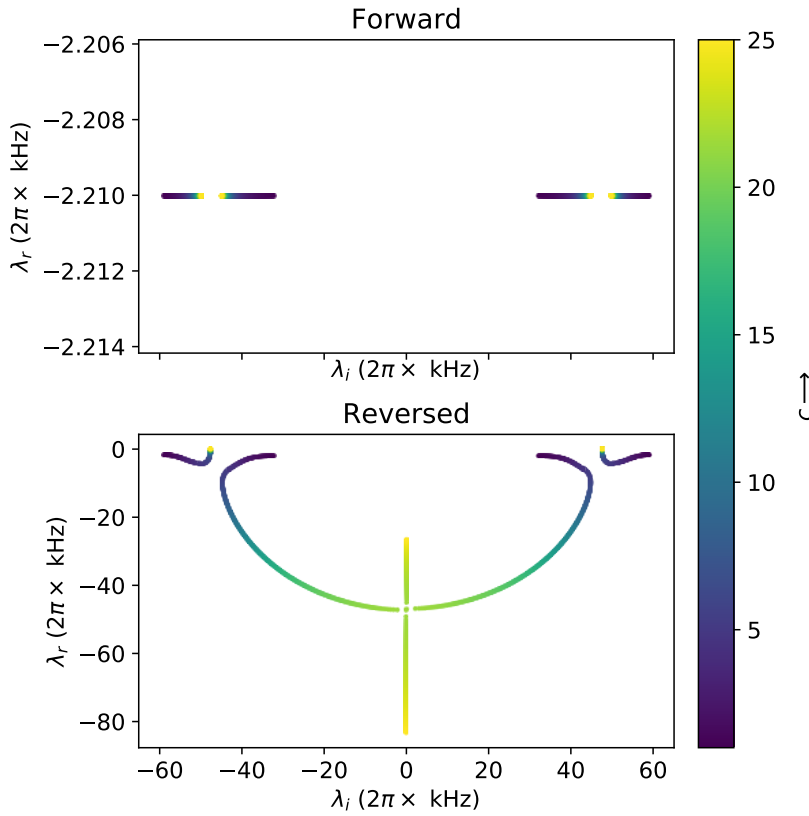


FIGURE 6.5: The evolution of the dissipative normal modes of the system as the asymmetry parameter c increases is shown in this plot. λ_r , λ_i stand for the real and imaginary parts of the eigenvalues of the dynamical matrix \mathbb{A} .

6.6 Discussion

I have studied heat rectification in a model composed of two coupled harmonic oscillators connected to Langevin baths, which could be realized with trapped ions and optical molasses. This simple model allows analytical treatment but still has enough complexity to examine different ingredients that can produce rectification. The results reported in this chapter demonstrate in a simple but realistic model that harmonic systems can rectify heat current if they have features which depend on the temperature [55]. I implement this notion of temperature-dependent features by defining the baths exchange operation as an exchange of both temperatures and coupling parameters of the baths to the system. The temperature dependence of the bath-system coupling occurs naturally in laser-cooled trapped ion setups.

I have also studied the phonon spectra of the system, aided by a normal mode

analysis, comparing the match/mismatch of the phonon bands, to reach the conclusion that the band match/mismatch description for heat rectification is also valid for systems which are purely harmonic, as long as there are temperature-dependent features.

Conclusions

“Don’t adventures ever have an end? I suppose not. Someone else always has to carry on the story.”

J. R. R. Tolkien

The Fellowship of the Ring

In this Thesis I have presented the most relevant results of the research I have conducted during my PhD, which embraces the study of asymmetric scattering and heat transport. The general goal of my research was to design devices that allow asymmetric transport and that are realistic enough, so they can be implemented experimentally. In this chapter I will summarize the main results of this Thesis and present the conclusions.

Conclusions to part I

- **Asymmetric scattering by non-Hermitian potentials**
 - Six types of devices with asymmetric scattering are possible when imposing 0 or 1 for the values of the scattering probabilities.
 - Hermitian Hamiltonians do not allow for any asymmetry in transmission and reflection probabilities, therefore in order to design asymmetric devices non-Hermitian Hamiltonians are needed. Besides, non-local potentials are needed for asymmetric scattering.
 - There are 8 symmetries that generate all the possible transformations of the potential matrix elements, which consist in complex conjugation, coordinate inversion, the identity and transposition. The eight symmetries arise from the commutation or pseudohermiticity of the potential with an element of the Klein’s 4-group $\mathbb{K}_4 = \{1, \Pi, \Theta, \Pi\theta\}$. The symmetries impose selection rules for the scattering amplitudes that conditions the design of some of the devices.
 - The conventional definition of a symmetry in terms of commutation with a unitary/antiunitary operator A is extended with the concept of

A -pseudohermiticity for non-Hermitian Hamiltonians. Both commutation and A -pseudohermiticity must be considered on the same footing.

- Some example potentials are given for the different asymmetric devices, in particular a local PT-potential that works as a transparent 1-way reflector in a broad domain of incident momenta.
- **S -matrix pole symmetries for non-Hermitian scattering Hamiltonians**
 - The symmetries of a non-Hermitian Hamiltonian, understood as commutation or A -pseudohermiticity, can be rewritten as the invariance of H with respect to the action of a unitary or antiunitary superoperator, $H = \mathcal{L}(H)$. Following this approach with the 8 symmetries described in chapter 1, a group structure is unveiled: the 8 symmetries form the elementary abelian group E8.
 - In refs. [22, 70, 71] it was shown that A -pseudohermiticity (with A linear and Hermitian) or commutativity with an antilinear Hermitian operator were necessary and sufficient conditions for a discrete Hamiltonian to have conjugate pairs of discrete eigenenergies. I show that this result can be extended to scattering Hamiltonians. Scattering Hamiltonians that satisfy the same conditions, have the poles of their S -matrix forming conjugate pairs in the complex energy plane.
 - I provided examples of the distribution of poles using separable potentials. The two examples correspond to the non-trivial symmetries: time-reversal and parity-pseudohermiticity.
- **Quantum-optical implementation of non-Hermitian potentials for asymmetric scattering**
 - I propose a quantum-optical implementation of non-local and non-Hermitian potentials with asymmetric scattering amplitudes. Since they are non-local and also non-PT symmetrical they allow asymmetric transmission.
 - The non-Hermitian potentials are effective interactions for the ground state of a two-level atom impinging on a laser field. They are found using Feshbach projection technique.

- I present examples of a \mathcal{T}/\mathcal{A} device (One-way T-filter), a \mathcal{R}/\mathcal{A} device (One-way R-filter) and a partial \mathcal{TR}/\mathcal{A} device (One-way mirror).

Conclusions to part II

- **Local rectification of heat flux**

- I have presented a design for a thermal rectifier based on a localized impurity in a chain of atoms. The on-site potential and interatomic interactions are modeled with harmonic and Morse potentials, respectively.
- As opposed to other models, the chain is homogeneous and the only structural asymmetry is the impurity.
- The numerical results show normal heat conduction without the impurity and rectification when it is present.
- Rectification also occurs when the Morse interaction is substituted by a harmonic one, although it is somewhat weaker.

- **Asymmetric heat transport in ion crystals**

- I introduced a model of a chain of ions trapped in individual microtraps and in contact at both ends with thermal baths mediated by optical molasses.
- Numerical results show that there is rectification when the microtrap frequencies are graded along the chain.
- In this model I explore some of the mechanisms that have been proposed in the literature to improve rectification, namely long range interactions and graded structures.
- This model could be implemented in a trapped-ion platform, which is interesting because is one of the most controllable quantum technologies platform. Besides, this work connects two different scientific communities: ion trappers and researchers in thermal rectification.

- **Heat rectification with a minimal model of two harmonic oscillators**
 - I study thermal rectification in an analytically treatable model composed of two coupled harmonic oscillators connected to Langevin Baths.
 - The results demonstrate that thermal rectification is also possible in harmonic systems if there are temperature-dependent features. In this case, the temperature dependence is in the coupling of the oscillators to the baths. This temperature dependence arises naturally in Doppler-cooled trapped-ion setups.
 - The phonon band match-mismatch description that was proposed for non-harmonic systems also applies to this harmonic model.

Appendices

Appendix A

Properties of separable potentials

A.1 Transition operator

For a separable potential $V = V_0 |\phi\rangle\langle\chi|$, the transition operator becomes

$$T_{op} = \alpha |\phi\rangle\langle\chi|, \quad (\text{A.1})$$

where $\alpha = V_0 + V_0^2 \langle\chi| G(E) |\phi\rangle$. Then using the Lippmann-Schwinger equation we get that

$$\begin{aligned} T_{op}(E) &= V + VG_0(E)T_{op}(E) \\ &= [V_0 + \alpha V_0 \langle\chi| G_0(E) |\phi\rangle] |\phi\rangle\langle\chi|, \end{aligned} \quad (\text{A.2})$$

where $G_0(E) = (E - H_0)^{-1}$ is the Green's operator for free motion. Solving for α now gives

$$\alpha = \frac{V_0}{1 - V_0 \langle\chi| G_0(E) |\phi\rangle} = \frac{V_0}{1 - V_0 Q_0(E)}. \quad (\text{A.3})$$

A.2 S-matrix eigenvalues

The eigenvalues for the S-matrix are given by eq. (2.9) in terms of the reflection and transmission amplitudes. For a separable potential, using eq. (1.9), we can

simplify the transmission and reflection coefficients as

$$\begin{aligned}
 T^l &= 1 - \frac{2\pi im}{p} \alpha \phi(p) \chi^*(p), \\
 T^r &= 1 - \frac{2\pi im}{p} \alpha \phi(-p) \chi^*(-p), \\
 R^l &= -\frac{2\pi im}{p} \alpha \phi(-p) \chi^*(p), \\
 R^r &= -\frac{2\pi im}{p} \alpha \phi(p) \chi^*(-p).
 \end{aligned} \tag{A.4}$$

If we now define

$$\Gamma = \frac{2\pi im}{p} \alpha [\phi(p) \chi^*(p) + \phi(-p) \chi^*(-p)], \tag{A.5}$$

we can write the eigenvalues as simply

$$S_j = 1 - \frac{\Gamma - (-1)^j \Gamma}{2}. \tag{A.6}$$

Note that $S_2 = 1$ for all p . Clearly the following relation must also always hold for the reflection and transmission amplitudes,

$$T^l + T^r - T^l T^r + R^l R^r = 1. \tag{A.7}$$

Appendix B

Numerical calculation of transmission and reflection coefficients

Here we will discuss how to numerically solve the stationary Schrödinger equation for the two-level system by the invariant imbedding method [142, 143].

Let the potential $\mathcal{V}(x)$ be non-zero in the region $-d < x < d$. We introduce the following dimensionless variables: $\bar{k} = (2mE)^{1/2}2d/\hbar$, $\bar{x} = x/(2d) + 1/2$, $\bar{\Omega}(\bar{x}) = (4md^2/\hbar)\Omega(x)$ and $\bar{\Gamma} = (4md^2/\hbar)(\gamma - 2i\Delta)$. The non-Hermitian dimensionless Hamiltonian for the system takes the form

$$\bar{\mathcal{H}} = \bar{\mathcal{H}}_0 + \bar{\mathcal{V}}(\bar{x}), \quad (\text{B.1})$$

$$\bar{\mathcal{H}}_0 = -\frac{\partial^2}{\partial \bar{x}^2} + \begin{pmatrix} 0 & 0 \\ 0 & -i\bar{\Gamma} \end{pmatrix}, \quad (\text{B.2})$$

$$\bar{\mathcal{V}}(\bar{x}) = \begin{pmatrix} 0 & \bar{\Omega}(\bar{x}) \\ \bar{\Omega}(\bar{x})^* & 0 \end{pmatrix}. \quad (\text{B.3})$$

To set the matrices we use as in the main text the convention for internal states $|1\rangle = \begin{pmatrix} 1 \\ 0 \end{pmatrix}$ and $|2\rangle = \begin{pmatrix} 0 \\ 1 \end{pmatrix}$. To simplify the notation, we will from now on drop the bars above variables and operators for the remaining part of this section A. The

corresponding stationary Schrödinger equation is now

$$\begin{aligned} k^2 \psi^{(1)}(x) &= -\frac{\partial^2}{\partial x^2} \psi^{(1)}(x) + \Omega(x) \psi^{(2)}(x), \\ k^2 \psi^{(2)}(x) &= -\frac{\partial^2}{\partial x^2} \psi^{(2)}(x) + \Omega(x)^* \psi_1(x) - i\Gamma \psi^{(2)}(x). \end{aligned}$$

Let us denote as $|\Psi_\alpha(x)\rangle$ the wave vector for the atom impinging in internal level α , $\alpha = 1, 2$. This vector has ground and excited state components, generically $\langle \beta | \psi_\alpha(x) \rangle$, $\beta = 1, 2$, which are still functions of x . We can define the matrices $F(x)$ and $\tilde{F}(x)$ as

$$F_{\beta,\alpha}(x) = \langle \beta | \psi_\alpha(x) \rangle, \quad \tilde{F}_{\beta,\alpha}(x) = \langle \beta | \tilde{\psi}_\alpha(x) \rangle, \quad (\text{B.4})$$

so the stationary Schrödinger equation can be rewritten as

$$\begin{aligned} [k^2 - \mathcal{H}_0 - \mathcal{V}(x)] F(x) &= 0, \\ [k^2 - \mathcal{H}_0 - \mathcal{V}(x)] \tilde{F}(x) &= 0. \end{aligned} \quad (\text{B.5})$$

B.1 Free motion, $\mathcal{V} = 0$

When $\mathcal{V}(x) = 0$ we get

$$\begin{aligned} [k^2 - \mathcal{H}_0] |\psi_\alpha(x)\rangle &= 0, \\ [k^2 - \mathcal{H}_0] |\tilde{\psi}_\alpha(x)\rangle &= 0, \end{aligned} \quad (\text{B.6})$$

for $\alpha = 1, 2$. We can write down the solutions for particles “coming” from the left $|\psi_\alpha(x)\rangle$ in internal state $|\alpha\rangle$ as

$$|\psi_1(x)\rangle = \begin{pmatrix} \frac{1}{\sqrt{k}} e^{ikx} \\ 0 \end{pmatrix}, \quad |\psi_2(x)\rangle = \begin{pmatrix} 0 \\ \frac{1}{\sqrt[4]{k^2+i\Gamma}} e^{i\sqrt{k^2+i\Gamma}x} \end{pmatrix},$$

where we assume the branch $\text{Im } \sqrt{k^2 + i\Gamma} \geq 0$. $|\psi_2(x)\rangle$ is a regular traveling wave only for real $\sqrt{k^2 + i\Gamma}$. If the square root has an imaginary part, $|\psi_2(x)\rangle$ decays from left to right. The solutions for incidence from the right $|\tilde{\psi}_\alpha(x)\rangle$ in internal

state $|\alpha\rangle$ are similarly

$$|\tilde{\psi}_1(x)\rangle = \begin{pmatrix} \frac{1}{\sqrt{k}}e^{-ikx} \\ 0 \end{pmatrix}, |\tilde{\psi}_2(x)\rangle = \begin{pmatrix} 0 \\ \frac{1}{\sqrt[4]{k^2+i\Gamma}}e^{-i\sqrt{k^2+i\Gamma}x} \end{pmatrix}.$$

The normalization is chosen in such a way that the dimensionless probability current is constant (and equal) for all solutions with real $\sqrt{k^2 + i\Gamma}$.

The solutions are given by $F(x) = h_+(x)$ and $\tilde{F}(x) = h_-(x)$, where

$$h_{\pm}(x) = \begin{pmatrix} \frac{1}{\sqrt{k}}e^{\pm ikx} & 0 \\ 0 & \frac{1}{\sqrt[4]{k^2+i\Gamma}}e^{\pm i\sqrt{k^2+i\Gamma}x} \end{pmatrix}. \quad (\text{B.7})$$

The Wronskian is $W(h_+, h_-)(x) = 2i$ so that these are linearly independent solutions.

B.2 General case

To solve the general case, we construct the Green's function defined by

$$(k^2 - \mathcal{H}_0)G_0(x, x') = \delta(x - x')\mathbf{1}. \quad (\text{B.8})$$

It is given by

$$\begin{aligned} G_0(x, x') &= W^{-1} \begin{cases} h_+(x)h_-(x') & x > x', \\ h_+(x')h_-(x) & x' > x, \end{cases} \\ &= -\frac{i}{2} \begin{pmatrix} \frac{1}{k}e^{ik|x-x'|} & 0 \\ 0 & \frac{e^{i\sqrt{k^2+i\Gamma}|x-x'|}}{\sqrt{k^2+i\Gamma}} \end{pmatrix}. \end{aligned} \quad (\text{B.9})$$

The Green's function allows us to solve for $F(x)$ and $\tilde{F}(x)$ in integral form,

$$\begin{aligned} F(x) &= h_+(x) + \int_{-\infty}^{\infty} dx' G_0(x, x') \mathcal{V}(x') F(x'), \\ \tilde{F}(x) &= h_-(x) + \int_{-\infty}^{\infty} dx' G_0(x, x') \mathcal{V}(x') \tilde{F}(x'). \end{aligned} \quad (\text{B.10})$$

B.3 Asymptotic form of the solutions

From eq. (B.10) we find the following asymptotic forms of $F(x)$ and $\tilde{F}(x)$:

$$\begin{aligned} F_\eta(x) &= \begin{cases} h_+(x) + h_-(x)R & x < 0 \\ h_+(x)T & x > 1 \end{cases}, \\ \tilde{F}_\eta(x) &= \begin{cases} h_-(x)\tilde{T} & x < 0 \\ h_-(x) + h_+(x)\tilde{R} & x > 1 \end{cases}, \end{aligned} \quad (\text{B.11})$$

where the R and T matrices for incidence from the left are given by

$$\begin{aligned} R &= W^{-1} \int_0^1 dx' h_+(x') \mathcal{V}(x') F(x'), \\ T &= \mathbf{1} + W^{-1} \int_0^1 dx' h_-(x') \mathcal{V}(x') F(x'), \end{aligned} \quad (\text{B.12})$$

whereas, for right incidence,

$$\begin{aligned} \tilde{R} &= W^{-1} \int_0^\eta dx' h_-(x') \mathcal{V}(x') \tilde{F}_\eta(x'), \\ \tilde{T} &= \mathbf{1} + W^{-1} \int_0^\eta dx' h_+(x') \mathcal{V}(x') \tilde{F}_\eta(x'). \end{aligned} \quad (\text{B.13})$$

In particular, for left incidence in the ground-state, we get if $x < 0$,

$$|\psi_1(x)\rangle = \begin{pmatrix} \frac{1}{\sqrt{k}} e^{ikx} \\ 0 \end{pmatrix} + \begin{pmatrix} R_{1,1} \frac{1}{\sqrt{k}} e^{-ikx} \\ R_{2,1} \frac{1}{\sqrt[4]{k^2+i\Gamma}} e^{-i\sqrt{k^2+i\Gamma}x} \end{pmatrix}, \quad (\text{B.14})$$

and, if $x > 1$,

$$|\psi_1(x)\rangle = \begin{pmatrix} T_{1,1} \frac{1}{\sqrt{k}} e^{ikx} \\ T_{2,1} \frac{1}{\sqrt[4]{k^2+i\Gamma}} e^{i\sqrt{k^2+i\Gamma}x} \end{pmatrix}. \quad (\text{B.15})$$

When $\sqrt{k^2 + i\Gamma}$ is real, the elements of T and R in Eqs. (B.14) and (B.15) are transmission and reflection amplitudes for waves traveling away from the interaction region. However when $\text{Im}\sqrt{k^2 + i\Gamma} > 0$ the waves for the excited state 2 are evanescent. In scattering theory parlance the channel is “closed”, so the $T_{2,1}$ and $R_{2,1}$ are just proportionality factors rather than proper transmission and reflection amplitudes for travelling waves. By continuity however, it is customary to keep the same notation and even terminology for closed or open channels.

In a similar way, for right incidence in the ground state and $x > 1$,

$$|\tilde{\psi}_1(x)\rangle = \begin{pmatrix} \frac{1}{\sqrt{k}}e^{-ikx} \\ 0 \end{pmatrix} + \begin{pmatrix} \tilde{R}_{1,1}\frac{1}{\sqrt{k}}e^{ikx} \\ \tilde{R}_{2,1}\frac{1}{\sqrt[4]{k^2+i\Gamma}}e^{i\sqrt{k^2+i\Gamma}x} \end{pmatrix}, \quad (\text{B.16})$$

whereas, for $x < 0$,

$$|\tilde{\psi}_1(x)\rangle = \begin{pmatrix} \tilde{T}_{1,1}\frac{1}{\sqrt{k}}e^{-ikx} \\ \tilde{T}_{2,1}\frac{1}{\sqrt[4]{k^2+i\Gamma}}e^{-i\sqrt{k^2+i\Gamma}x} \end{pmatrix}. \quad (\text{B.17})$$

Note that alternative definitions of the amplitudes may be found in many works, without momentum prefactors.

The amplitudes relevant for the main text are $T^l = T_{1,1}$, $T^r = \tilde{T}_{1,1}$, $R^l = R_{1,1}$, and $R^r = \tilde{R}_{1,1}$. The following subsection explains how to compute them.

B.4 Differential equations for R and T matrices

To solve for R and T we will use cut-off versions of the potential,

$$\mathcal{V}_\eta(x) = \begin{cases} \mathcal{V}(x) & 0 \leq x \leq \eta, \\ 0 & \text{Otherwise} \end{cases}, \quad (\text{B.18})$$

where $0 \leq \eta \leq 1$, and corresponding matrices

$$\begin{aligned} R_\eta &= W^{-1} \int_0^\eta dx' h_+(x') \mathcal{V}(x') F_\eta(x'), \\ T_\eta &= \mathbf{1} + W^{-1} \int_0^\eta dx' h_-(x') \mathcal{V}(x') F_\eta(x'), \\ \tilde{R}_\eta &= W^{-1} \int_0^\eta dx' h_-(x') \mathcal{V}(x') \tilde{F}_\eta(x'), \\ \tilde{T}_\eta &= \mathbf{1} + W^{-1} \int_0^\eta dx' h_+(x') \mathcal{V}(x') \tilde{F}_\eta(x'). \end{aligned} \quad (\text{B.19})$$

Taking the derivative of these matrices with respect to η , we find a set of four coupled differential equations,

$$\frac{dR_\eta}{d\eta} = W^{-1}\tilde{T}_\eta h_+(\eta)\mathcal{V}(\eta)h_+(\eta)T_\eta, \quad (\text{B.20})$$

$$\frac{dT_\eta}{d\eta} = W^{-1}\left[h_-(\eta) + \tilde{R}_\eta h_+(\eta)\right]\mathcal{V}(\eta)h_+(\eta)T_\eta, \quad (\text{B.21})$$

$$\frac{d\tilde{R}_\eta}{d\eta} = W^{-1}\left[h_-(\eta) + \tilde{R}_\eta h_+(\eta)\right]\mathcal{V}(\eta)\left[h_-(\eta) + h_+(\eta)\tilde{R}_\eta\right], \quad (\text{B.22})$$

$$\frac{d\tilde{T}_\eta}{d\eta} = W^{-1}\tilde{T}_\eta h_+(\eta)\mathcal{V}(\eta)\left[h_-(\eta) + h_+(\eta)\tilde{R}_\eta\right]. \quad (\text{B.23})$$

The initial conditions are $R_0 = \tilde{R}_0 = 0$ and $T_0 = \tilde{T}_0 = \mathbf{1}$.

B.5 Improving numerical efficiency

The equations (B.22) and (B.23) involve only matrices for incidence from the right, they do not couple to any left-incidence matrix, whereas the equations for left incidence amplitudes involve couplings with amplitudes for right incidence. This asymmetry is due to the way we do the potential slicing. The asymmetry is not “fundamental” but we can use it for our advantage to simplify calculations. We can solve equations (B.22) and (B.23) to get amplitudes for right incidence. To get amplitudes for left incidence we use a mirror image of the potential and solve also these two equations. Thus it is enough to find an efficient numerical method to solve equations (B.22) and (B.23). In principle, one can now solve these differential equations from $\eta = 0$ to 1 to get all reflection and transmission amplitudes using the boundary conditions $\tilde{R}_0 = 0$ and $\tilde{T}_0 = \mathbf{1}$. However due to the exponential nature of the free-space solutions $h_{\pm}(x)$ especially if $\text{Im}\sqrt{k^2 + i\Gamma} > 0$, this is not very efficient numerically.

To avoid this problem we make new definitions,

$$\begin{aligned} \hat{S}_\eta &= \mathbf{1} + h_+(\eta)\tilde{R}_\eta h_-^{-1}(\eta), \\ \hat{T}_\eta &= h_+(0)\tilde{T}_\eta h_-^{-1}(\eta), \\ \hat{\mathcal{V}}(\eta) &= W^{-1}h_+^2(0)\mathcal{V}(\eta), \\ \hat{Q} &= ih_+^{-2}(0). \end{aligned} \quad (\text{B.24})$$

Rewriting the equations (B.22) and (B.23) in terms of these new variables we get

$$\begin{aligned}\frac{d\hat{S}_\eta}{d\eta} &= -2\hat{Q} + \hat{Q}\hat{S}_\eta + \hat{S}_\eta [\hat{Q} + \hat{\mathcal{V}}(\eta)\hat{S}_\eta], \\ \frac{d\hat{T}_\eta}{d\eta} &= \hat{T}_\eta [\hat{Q} + \hat{\mathcal{V}}(\eta)\hat{S}_\eta],\end{aligned}\quad (\text{B.25})$$

with initial conditions $\hat{T}_0 = \hat{S}_0 = \mathbf{1}$.

Let us consider solely incidence in the ground state. For right incidence in the ground state, the reflection coefficients and transmission coefficient are

$$\begin{aligned}\tilde{R}_{1,1} &= e^{-2ik} [(\hat{S}_{\eta=1})_{1,1} - 1], \\ \tilde{R}_{2,1} &= \frac{\sqrt[4]{k^2 + i\Gamma}}{\sqrt{k}} e^{-ik - i\sqrt{k^2 + i\Gamma}} (\hat{S}_{\eta=1})_{2,1}, \\ \tilde{T}_{1,1} &= e^{-ik} (\hat{T}_{\eta=1})_{1,1}, \\ \tilde{T}_{2,1} &= \frac{\sqrt[4]{k^2 + i\Gamma}}{\sqrt{k}} e^{-ik} (\hat{T}_{\eta=1})_{2,1}.\end{aligned}\quad (\text{B.26})$$

B.6 Bounds from unitarity

The S -matrix

$$S = \begin{pmatrix} T_{11} & T_{12} & \tilde{R}_{11} & \tilde{R}_{12} \\ T_{21} & T_{22} & \tilde{R}_{21} & \tilde{R}_{22} \\ R_{11} & R_{12} & \tilde{T}_{11} & \tilde{T}_{12} \\ R_{21} & R_{22} & \tilde{T}_{21} & \tilde{T}_{22} \end{pmatrix} \quad (\text{B.27})$$

is unitary for Hermitian Hamiltonians, in particular when $\gamma = 0$. Unitarity implies relations among the matrix elements and in particular

$$1 \geq |R_{11}|^2 + |T_{11}|^2, \quad (\text{B.28})$$

$$1 \geq |\tilde{R}_{11}|^2 + |\tilde{T}_{11}|^2, \quad (\text{B.29})$$

$$1 \geq |\tilde{R}_{11}|^2 + |T_{11}|^2, \quad (\text{B.30})$$

$$1 \geq |R_{11}|^2 + |\tilde{T}_{11}|^2. \quad (\text{B.31})$$

While the first two equations (B.28) and (B.29) are rather obvious because of probability conservation, the last two equations (B.30) and (B.31) are less so, and set physical limits to the possible asymmetric devices that can be constructed in the ground state subspace.

Appendix C

Full set of steady-state equations for the components of $\mathbb{C}^{S.S}$

Here is the full set of equations for the covariance matrix elements in the steady state. We use the shorthand notation $\langle \dots \rangle = \langle \dots \rangle^{s.s}$, i.e., all averages are in the steady state.

$$\begin{aligned}
& \frac{2k \langle p_2 q_1 \rangle}{m_1 m_2} + \frac{2\gamma_L \langle p_1^2 \rangle}{m_1^3} = \frac{2D_L}{m_1^2}, \\
& -\frac{2k \langle p_2 q_1 \rangle}{m_2^2} + \frac{2\gamma_R \langle p_2^2 \rangle}{m_2^3} = \frac{2D_R}{m_2^2}, \\
& -\frac{(k_L + k) \langle q_1 q_2 \rangle}{m_1} + \frac{k \langle q_2^2 \rangle}{m_1} + \frac{\gamma_L \langle p_2 q_1 \rangle}{m_1 m_2} + \frac{\langle p_1 p_2 \rangle}{m_1 m_2} = 0, \\
& \frac{(k_L + k) \langle p_2 q_1 \rangle}{m_1 m_2} - \frac{(k_R + k) \langle p_2 q_1 \rangle}{m_2^2} + \frac{\gamma_L \langle p_1 p_2 \rangle}{m_1^2 m_2} + \frac{\gamma_R \langle p_1 p_2 \rangle}{m_1 m_2^2} = 0, \\
& -\frac{(k_L + k) \langle q_1^2 \rangle}{m_1} + \frac{k \langle q_1 q_2 \rangle}{m_1} + \frac{\langle p_1^2 \rangle}{m_1^2} = 0, \\
& -\frac{(k_R + k) \langle q_2^2 \rangle}{m_2} + \frac{k \langle q_1 q_2 \rangle}{m_2} + \frac{\langle p_2^2 \rangle}{m_2^2} = 0, \\
& -\frac{(k_R + k) \langle q_1 q_2 \rangle}{m_2} + \frac{k \langle q_1^2 \rangle}{m_2} - \frac{\gamma_R \langle p_2 q_1 \rangle}{m_2^2} + \frac{\langle p_1 p_2 \rangle}{m_1 m_2} = 0.
\end{aligned}$$

Appendix D

Complete expressions for the Spectral Density Matrix

In section 6.5 we used the characteristic polynomial $P_{\mathbb{A}}(\lambda)$ of the dynamical matrix \mathbb{A} for the calculation of the spectral density matrix. $P_{\mathbb{A}}(\lambda)$ is defined as

$$\begin{aligned}
 P_{\mathbb{A}}(\lambda) &\equiv \det(\mathbb{A} - \lambda) \\
 &= \lambda^4 \\
 &+ \lambda^3 \left(\frac{\gamma_L}{m_1} + \frac{\gamma_R}{m_2} \right) \\
 &+ \lambda^2 \frac{(\gamma_L \gamma_R + m_2(k + k_L) + m_1(k + k_R))}{m_1 m_2} \\
 &+ \lambda \frac{(\gamma_R(k + k_L) + \gamma_L(k + k_R))}{m_1 m_2} \\
 &+ \frac{k(k_L + k_R) + k_L k_R}{m_1 m_2}.
 \end{aligned} \tag{D.1}$$

We also used the polynomials $\mathbb{S}_L(\lambda) = \sum_{n=0}^6 \lambda^n \mathbb{S}_{L,n}$ and $\mathbb{S}_R(\lambda) = \sum_{n=0}^6 \lambda^n \mathbb{S}_{R,n}$. There are 14 different polynomial coefficients, which are 4×4 matrices. This is the full list of coefficients,

$$\mathbb{S}_{L,0} = \begin{pmatrix} (k + k_R)^2 & k(k + k_R) & 0 & 0 \\ k(k + k_R) & k^2 & 0 & 0 \\ 0 & 0 & 0 & 0 \\ 0 & 0 & 0 & 0 \end{pmatrix},$$

$$\begin{aligned}
\mathbb{S}_{R,0} &= \begin{pmatrix} k^2 & k(k+k_L) & 0 & 0 \\ k(k+k_L) & (k+k_L)^2 & 0 & 0 \\ 0 & 0 & 0 & 0 \\ 0 & 0 & 0 & 0 \end{pmatrix}, \\
\mathbb{S}_{L,1} &= \begin{pmatrix} 0 & k\gamma_R & -(k+k_R)^2 & -k(k+k_R) \\ -k\gamma_R & 0 & -k(k+k_R) & -k^2 \\ (k+k_R)^2 & k(k+k_R) & 0 & 0 \\ k(k+k_R) & k^2 & 0 & 0 \end{pmatrix}, \\
\mathbb{S}_{R,1} &= \begin{pmatrix} 0 & -k\gamma_L & -k^2 & -k(k+k_L) \\ k\gamma_L & 0 & -k(k+k_L) & -(k+k_L)^2 \\ k^2 & k(k+k_L) & 0 & 0 \\ k(k+k_L) & (k+k_L)^2 & 0 & 0 \end{pmatrix}, \\
\mathbb{S}_{L,2} &= \begin{pmatrix} 2(k+k_R)m_2 - \gamma_R^2 & km_2 & 0 & -k\gamma_R \\ km_2 & 0 & k\gamma_R & 0 \\ 0 & k\gamma_R & -(k+k_R)^2 & -k(k+k_R) \\ -k\gamma_R & 0 & -k(k+k_R) & -k^2 \end{pmatrix}, \\
\mathbb{S}_{R,2} &= \begin{pmatrix} 0 & km_1 & 0 & k\gamma_L \\ km_1 & 2(k+k_L)m_1 - \gamma_L^2 & -k\gamma_L & 0 \\ 0 & -k\gamma_L & -k^2 & -k(k+k_L) \\ k\gamma_L & 0 & -k(k+k_L) & -(k+k_L)^2 \end{pmatrix}, \\
\mathbb{S}_{L,3} &= \begin{pmatrix} 0 & 0 & \gamma_R^2 - 2(k+k_R)m_2 & -km_2 \\ 0 & 0 & -km_2 & 0 \\ 2(k+k_R)m_2 - \gamma_R^2 & km_2 & 0 & -k\gamma_R \\ km_2 & 0 & k\gamma_R & 0 \end{pmatrix}, \\
\mathbb{S}_{R,3} &= \begin{pmatrix} 0 & 0 & 0 & -km_1 \\ 0 & 0 & -km_1 & \gamma_L^2 - 2(k+k_L)m_1 \\ 0 & km_1 & 0 & k\gamma_L \\ km_1 & 2(k+k_L)m_1 - \gamma_L^2 & -k\gamma_L & 0 \end{pmatrix}, \\
\mathbb{S}_{L,4} &= \begin{pmatrix} m_2^2 & 0 & 0 & 0 \\ 0 & 0 & 0 & 0 \\ 0 & 0 & \gamma_R^2 - 2(k+k_R)m_2 & -km_2 \\ 0 & 0 & -km_2 & 0 \end{pmatrix},
\end{aligned}$$

$$\begin{aligned}
\$R,4 &= \begin{pmatrix} 0 & 0 & 0 & 0 \\ 0 & m_1^2 & 0 & 0 \\ 0 & 0 & 0 & -km_1 \\ 0 & 0 & -km_1 & \gamma_L^2 - 2(k + k_L)m_1 \end{pmatrix}, \\
\$L,5 &= \begin{pmatrix} 0 & 0 & -m_2^2 & 0 \\ 0 & 0 & 0 & 0 \\ m_2^2 & 0 & 0 & 0 \\ 0 & 0 & 0 & 0 \end{pmatrix}, \\
\$R,5 &= \begin{pmatrix} 0 & 0 & 0 & 0 \\ 0 & 0 & 0 & -m_1^2 \\ 0 & 0 & 0 & 0 \\ 0 & m_1^2 & 0 & 0 \end{pmatrix}, \\
\$L,6 &= \begin{pmatrix} 0 & 0 & 0 & 0 \\ 0 & 0 & 0 & 0 \\ 0 & 0 & -m_2^2 & 0 \\ 0 & 0 & 0 & 0 \end{pmatrix}, \\
\$R,6 &= \begin{pmatrix} 0 & 0 & 0 & 0 \\ 0 & 0 & 0 & 0 \\ 0 & 0 & 0 & 0 \\ 0 & 0 & 0 & -m_1^2 \end{pmatrix}. \tag{D.2}
\end{aligned}$$

Bibliography

- [1] B. Saleh and M. Teich, *Fundamentals of photonics*, ch. 6, pp. 233–234. Wiley, 1991.
- [2] E. Yariv and P. Yeh, *Optical waves in crystals: propagation and control of laser radiation*, ch. 4, p. 103. Wiley, 1984.
- [3] J. Muga, J. Palao, B. Navarro, and I. Egusquiza, “Complex absorbing potentials”, [Physics Reports 395, 357 - 426 \(2004\)](#).
- [4] A. Mostafazadeh, *Scattering Theory and PT-Symmetry*, pp. 75–121. Springer, 2018.
- [5] H. Feshbach, “Unified theory of nuclear reactions”, [Annals of Physics 5, 357 - 390 \(1958\)](#).
- [6] A. Ruschhaupt and J. G. Muga, “Atom diode: A laser device for a unidirectional transmission of ground-state atoms”, [Phys. Rev. A 70, 061604 \(2004\)](#).
- [7] A. Ruschhaupt, F. Delgado, and J. G. Muga, “Physical realization of -symmetric potential scattering in a planar slab waveguide”, [Journal of Physics A: Mathematical and General 38, L171–L176 \(2005\)](#).
- [8] S. Longhi, “Parity-time symmetry meets photonics: A new twist in non-Hermitian optics”, [EPL \(Europhysics Letters\) 120, 64001 \(2017\)](#).
- [9] V. V. Konotop, J. Yang, and D. A. Zezyulin, “Nonlinear waves in \mathcal{PT} -symmetric systems”, [Rev. Mod. Phys. 88, 035002 \(2016\)](#).
- [10] S. Nixon and J. Yang, “All-real spectra in optical systems with arbitrary gain-and-loss distributions”, [Phys. Rev. A 93, 031802 \(2016\)](#).

- [11] S. Nixon and J. Yang, “*Nonlinear light behaviors near phase transition in non-parity-time-symmetric complex waveguides*”, *Opt. Lett.* **41**, 2747–2750 (2016).
- [12] P. Chen and Y. D. Chong, “*Pseudo-Hermitian Hamiltonians generating waveguide mode evolution*”, *Phys. Rev. A* **95**, 062113 (2017).
- [13] A. Ruschhaupt, T. Dowdall, M. A. Simón, and J. G. Muga, “*Asymmetric scattering by non-Hermitian potentials*”, *EPL (Europhysics Letters)* **120**, 20001 (2017).
- [14] M. A. Simón, A. Buendía, and J. G. Muga, “*Symmetries and Invariants for Non-Hermitian Hamiltonians*”, *Mathematics* **6**, 111 (2018).
- [15] M. A. Simón, A. Buendía, A. Kiely, A. Mostafazadeh, and J. G. Muga, “*S-matrix pole symmetries for non-Hermitian scattering Hamiltonians*”, *Phys. Rev. A* **99**, 052110 (2019).
- [16] A. Alaña, S. Martínez-Garaot, M. A. Simón, and J. G. Muga, “*Symmetries of ($N \times N$) non-Hermitian Hamiltonian matrices*”, *Journal of Physics A: Mathematical and Theoretical* **53**, 135304 (2020).
- [17] D. Bernard and A. LeClair, *A Classification of Non-Hermitian Random Matrices*, pp. 207–214. Springer Netherlands, Dordrecht, 2002.
- [18] K. Kawabata, K. Shiozaki, M. Ueda, and M. Sato, “*Symmetry and Topology in Non-Hermitian Physics*”, *Phys. Rev. X* **9**, 041015 (2019).
- [19] C. M. Bender and S. Boettcher, “*Real Spectra in Non-Hermitian Hamiltonians Having PT Symmetry*”, *Phys. Rev. Lett.* **80**, 5243–5246 (1998).
- [20] M. Znojil, *Non-self-adjoint operators in quantum physics: ideas, people, and trends*, ch. 1, pp. 7–58. Wiley, 2015.
- [21] S. Longhi, “*A unidirectionally invisible \mathcal{PT} -symmetric complex crystal with arbitrary thickness*”, *Journal of Physics A: Mathematical and Theoretical* **47**, 485302 (2014).
- [22] A. Mostafazadeh, “*Pseudo-Hermiticity versus PT symmetry: The necessary condition for the reality of the spectrum of a non-Hermitian Hamiltonian*”, *Journal of Mathematical Physics* **43**, 205-214 (2002).

- [23] N. Li, J. Ren, L. Wang, G. Zhang, P. Hänggi, and B. Li, “*Colloquium: Phononics: Manipulating heat flow with electronic analogs and beyond*”, *Rev. Mod. Phys.* **84**, 1045–1066 (2012).
- [24] C. Starr, “*The Copper Oxide Rectifier*”, *Physics* **7**, 15-19 (1936).
- [25] M. Terraneo, M. Peyrard, and G. Casati, “*Controlling the Energy Flow in Nonlinear Lattices: A Model for a Thermal Rectifier*”, *Phys. Rev. Lett.* **88**, 094302 (2002).
- [26] B. Li, L. Wang, and G. Casati, “*Thermal Diode: Rectification of Heat Flux*”, *Phys. Rev. Lett.* **93**, 184301 (2004).
- [27] N. Roberts and D. Walker, “*A review of thermal rectification observations and models in solid materials*”, *International Journal of Thermal Sciences* **50**, 648 - 662 (2011).
- [28] Z.-Q. Ye and B.-Y. Cao, “*Thermal rectification at the bimaterial nanocontact interface*”, *Nanoscale* **9**, 11480-11487 (2017).
- [29] L. Wang and B. Li, “*Thermal Memory: A Storage of Phononic Information*”, *Phys. Rev. Lett.* **101**, 267203 (2008).
- [30] L. Wang and B. Li, “*Thermal Logic Gates: Computation with Phonons*”, *Phys. Rev. Lett.* **99**, 177208 (2007).
- [31] B. Li, L. Wang, and G. Casati, “*Negative differential thermal resistance and thermal transistor*”, *Applied Physics Letters* **88**, 143501 (2006).
- [32] K. Joulain, J. Drevillon, Y. Ezzahri, and J. Ordonez-Miranda, “*Quantum Thermal Transistor*”, *Phys. Rev. Lett.* **116**, 200601 (2016).
- [33] C. W. Chang, D. Okawa, A. Majumdar, and A. Zettl, “*Solid-State Thermal Rectifier*”, *Science* **314**, 1121–1124 (2006).
- [34] W. Kobayashi, Y. Teraoka, and I. Terasaki, “*An oxide thermal rectifier*”, *Applied Physics Letters* **95**, 171905 (2009).
- [35] D. M. Leitner, “*Thermal Boundary Conductance and Thermal Rectification in Molecules*”, *The Journal of Physical Chemistry B* **117**, 12820-12828 (2013).

- [36] M. Elzouka and S. Ndao, “*High Temperature Near-Field NanoThermoMechanical Rectification*”, *Scientific Reports* **7**, 44901 (2017).
- [37] N. Li, P. Hänggi, and B. Li, “*Ratcheting heat flux against a thermal bias*”, *EPL (Europhysics Letters)* **84**, 40009 (2008).
- [38] B. Hu, L. Yang, and Y. Zhang, “*Asymmetric Heat Conduction in Nonlinear Lattices*”, *Phys. Rev. Lett.* **97**, 124302 (2006).
- [39] J. Wang, E. Pereira, and G. Casati, “*Thermal rectification in graded materials*”, *Phys. Rev. E* **86**, 010101 (2012).
- [40] S. Chen, E. Pereira, and G. Casati, “*Ingredients for an efficient thermal diode*”, *EPL (Europhysics Letters)* **111**, 30004 (2015).
- [41] M. Romero-Bastida, J. O. Miranda-Peña, and J. M. López, “*Thermal rectification in mass-graded next-nearest-neighbor Fermi-Pasta-Ulam lattices*”, *Phys. Rev. E* **95**, 032146 (2017).
- [42] N. Yang, N. Li, L. Wang, and B. Li, “*Thermal rectification and negative differential thermal resistance in lattices with mass gradient*”, *Phys. Rev. B* **76**, 020301 (2007).
- [43] M. Romero-Bastida and J. M. Arizmendi-Carvajal, “*Structural influences on thermal rectification of one-dimensional mass-graded lattices*”, *Journal of Physics A: Mathematical and Theoretical* **46**, 115006 (2013).
- [44] R. Dettori, C. Melis, R. Rurali, and L. Colombo, “*Thermal rectification in silicon by a graded distribution of defects*”, *Journal of Applied Physics* **119**, 215102 (2016).
- [45] E. Pereira, “*Graded anharmonic crystals as genuine thermal diodes: Analytical description of rectification and negative differential thermal resistance*”, *Phys. Rev. E* **82**, 040101 (2010).
- [46] E. Pereira, “*Sufficient conditions for thermal rectification in general graded materials*”, *Phys. Rev. E* **83**, 031106 (2011).
- [47] R. R. Ávila and E. Pereira, “*Thermal rectification features: a study starting from local assumptions*”, *Journal of Physics A: Mathematical and Theoretical* **46**, 055002 (2013).

- [48] D. Bagchi, “*Thermal transport in the Fermi-Pasta-Ulam model with long-range interactions*”, *Phys. Rev. E* **95**, 032102 (2017).
- [49] E. Pereira and R. R. Ávila, “*Increasing thermal rectification: Effects of long-range interactions*”, *Phys. Rev. E* **88**, 032139 (2013).
- [50] N. Zeng and J.-S. Wang, “*Mechanisms causing thermal rectification: The influence of phonon frequency, asymmetry, and nonlinear interactions*”, *Phys. Rev. B* **78**, 024305 (2008).
- [51] G. Katz and R. Kosloff, “*Quantum Thermodynamics in Strong Coupling: Heat Transport and Refrigeration*”, *Entropy* **18**, (2016).
- [52] G. Benenti, G. Casati, C. Mejía-Monasterio, and M. Peyrard, *From Thermal Rectifiers to Thermoelectric Devices*, pp. 365–407. Springer International Publishing, 2016.
- [53] D. Segal and A. Nitzan, “*Spin-Boson Thermal Rectifier*”, *Phys. Rev. Lett.* **94**, 034301 (2005).
- [54] D. Segal and A. Nitzan, “*Heat rectification in molecular junctions*”, *The Journal of Chemical Physics* **122**, 194704 (2005).
- [55] E. Pereira, “*Requisite ingredients for thermal rectification*”, *Phys. Rev. E* **96**, 012114 (2017).
- [56] E. Pereira, “*Thermal rectification in classical and quantum systems: Searching for efficient thermal diodes*”, *EPL (Europhysics Letters)* **126**, 14001 (2019).
- [57] M. A. Simón, S. Martínez-Garaot, M. Pons, and J. G. Muga, “*Asymmetric heat transport in ion crystals*”, *Phys. Rev. E* **100**, 032109 (2019).
- [58] J. Taylor, *Scattering Theory: Quantum Theory on Nonrelativistic Collisions*. Wiley, 1972.
- [59] E. P. Wigner, *Group theory and its application to the quantum mechanics of atomic spectra*. Pure Appl. Phys. Academic Press, New York, NY, 1959.
- [60] A. Mostafazadeh, “*Pseudo-Hermitian Representation of Quantum Mechanics*”, *International Journal of Geometric Methods in Modern Physics* **07**, 1191 (2010).

- [61] Z. Lin, H. Ramezani, T. Eichelkraut, T. Kottos, H. Cao, and D. N. Christodoulides, “*Unidirectional Invisibility Induced by \mathcal{PT} -Symmetric Periodic Structures*”, *Phys. Rev. Lett.* **106**, 213901 (2011).
- [62] X. Yin and X. Zhang, “*Unidirectional light propagation at exceptional points*”, *Nature Materials* **12**, 175–177 (2013).
- [63] Y. Huang, C. Min, and G. Veronis, “*Broadband near total light absorption in non- PT -symmetric waveguide-cavity systems*”, *Opt. Express* **24**, 22219–22231 (2016).
- [64] J. P. Palao, J. G. Muga, and R. Sala, “*Composite Absorbing Potentials*”, *Phys. Rev. Lett.* **80**, 5469–5472 (1998).
- [65] S. Brouard, D. Macias, and J. G. Muga, “*Perfect absorbers for stationary and wavepacket scattering*”, *Journal of Physics A: Mathematical and General* **27**, L439–L445 (1994).
- [66] J. Palao and J. Muga, “*A simple construction procedure of absorbing potentials*”, *Chemical Physics Letters* **292**, 1 - 6 (1998).
- [67] R. Snieder, “*The role of the Born approximation in nonlinear inversion*”, *Inverse Problems* **6**, 247–266 (1990).
- [68] A. Mostafazadeh, “*Transfer matrices as nonunitary S matrices, multimode unidirectional invisibility, and perturbative inverse scattering*”, *Phys. Rev. A* **89**, 012709 (2014).
- [69] S. A. R. Horsley, M. Artoni, and G. C. La Rocca, “*Spatial Kramers–Kronig relations and the reflection of waves*”, *Nature Photonics* **9**, 436–439 (2015).
- [70] A. Mostafazadeh, “*Pseudo-Hermiticity versus PT -symmetry. II. A complete characterization of non-Hermitian Hamiltonians with a real spectrum*”, *Journal of Mathematical Physics* **43**, 2814-2816 (2002).
- [71] A. Mostafazadeh, “*Pseudo-Hermiticity versus PT -symmetry III: Equivalence of pseudo-Hermiticity and the presence of antilinear symmetries*”, *Journal of Mathematical Physics* **43**, 3944-3951 (2002).
- [72] H. Rose, *A course on finite groups*. Springer, 2009.

- [73] Y. V. Popov, A. Galstyan, B. Piraux, P. F. O'Mahony, F. Mota-Furtado, P. Decleva, and O. Chuluunbaatar, *Separable Potentials Model for Atoms and Molecules in Strong Ultrashort Laser Pulses*, pp. 221–242. Springer International Publishing, Cham, 2019.
- [74] J. G. Muga and R. F. Snider, “*Scattering by a separable potential in one dimension*”, *Canadian Journal of Physics* **68**, 403-410 (1990), <https://doi.org/10.1139/p90-064>.
- [75] J. Muga, G. Wei, and R. Snider, “*Survival Probability for the Yamaguchi Potential*”, *Annals of Physics* **252**, 336 - 356 (1996).
- [76] J. G. Muga, G. W. Wei, and R. F. Snider, “*Short-time behaviour of the quantum survival probability*”, *Europhysics Letters (EPL)* **35**, 247–252 (1996).
- [77] J. G. Muga and J. P. Palao, “*Solvable model for quantum wavepacket scattering in one dimension*”, *Journal of Physics A: Mathematical and General* **31**, 9519–9534 (1998).
- [78] J. G. Muga and J. P. Palao, “*Negative time delays in one dimensional absorptive collisions*”, *Annalen der Physik* **7**, 671–678 (1998).
- [79] L. Hlophe and C. Elster, “*Separable representation of multichannel nucleon-nucleus optical potentials*”, *Phys. Rev. C* **95**, 054617 (2017).
- [80] A. Ruschhaupt, J. A. Damborenea, B. Navarro, J. G. Muga, and G. C. Hegerfeldt, “*Exact and approximate complex potentials for modelling time observables*”, *Europhysics Letters (EPL)* **67**, 1–7 (2004).
- [81] A. Ruschhaupt, J. G. Muga, and G. C. Hegerfeldt, *Detector Models for the Quantum Time of Arrival*, pp. 65–96. Springer Berlin Heidelberg, Berlin, Heidelberg, 2009.
- [82] G. C. Hegerfeldt and D. G. Sondermann, “*Conditional Hamiltonian and reset operator in the quantum jump approach*”, *Quantum and Semiclassical Optics: Journal of the European Optical Society Part B* **8**, 121–132 (1996).
- [83] J. A. Damborenea, I. L. Egusquiza, G. C. Hegerfeldt, and J. G. Muga, “*Measurement-based approach to quantum arrival times*”, *Phys. Rev. A* **66**, 052104 (2002).

- [84] B. Navarro, I. L. Egusquiza, J. G. Muga, and G. C. Hegerfeldt, “*Suppression of Rabi oscillations for moving atoms*”, *Phys. Rev. A* **67**, 063819 (2003).
- [85] M. K. Oberthaler, R. Affalterer, S. Bernet, J. Schmiedmayer, and A. Zeilinger, “*Atom Waves in Crystals of Light*”, *Phys. Rev. Lett.* **77**, 4980–4983 (1996).
- [86] E. W. Streed, J. Mun, M. Boyd, G. K. Campbell, P. Medley, W. Ketterle, and D. E. Pritchard, “*Continuous and Pulsed Quantum Zeno Effect*”, *Phys. Rev. Lett.* **97**, 260402 (2006).
- [87] J. Zhang, J. H. Shim, I. Niemeyer, T. Taniguchi, T. Teraji, H. Abe, S. Onoda, T. Yamamoto, T. Ohshima, J. Isoya, and D. Suter, “*Experimental Implementation of Assisted Quantum Adiabatic Passage in a Single Spin*”, *Phys. Rev. Lett.* **110**, 240501 (2013).
- [88] H. Feshbach, “*A unified theory of nuclear reactions. II*”, *Annals of Physics* **19**, 287 - 313 (1962).
- [89] R. D. Levine, *Quantum mechanics of molecular rate processes*. Clarendon Press, Oxford, 1969.
- [90] D. Chudesnikov and V. Yakovlev, “*Bragg scattering on complex potential and formation of super-narrow momentum distributions of atoms in light fields*”, *Laser Physics* **1**, 110–119 (1991).
- [91] A. Ruschhaupt and J. G. Muga, “*Adiabatic interpretation of a two-level atom diode, a laser device for unidirectional transmission of ground-state atoms*”, *Phys. Rev. A* **73**, 013608 (2006).
- [92] A. Ruschhaupt, J. G. Muga, and M. G. Raizen, “*Improvement by laser quenching of an ‘atom diode’: a one-way barrier for ultra-cold atoms*”, *Journal of Physics B: Atomic, Molecular and Optical Physics* **39**, L133–L138 (2006).
- [93] A. Ruschhaupt and J. G. Muga, “*Three-dimensional effects in atom diodes: Atom-optical devices for one-way motion*”, *Phys. Rev. A* **76**, 013619 (2007).
- [94] N. Khaneja, T. Reiss, C. Kehlet, T. Schulte-Herbrüggen, and S. J. Glaser, “*Optimal control of coupled spin dynamics: design of NMR pulse sequences*

- by gradient ascent algorithms”, Journal of Magnetic Resonance* **172**, 296 - 305 (2005).
- [95] N. Wu, A. Nanduri, and H. Rabitz, “Optimal suppression of defect generation during a passage across a quantum critical point”, *Phys. Rev. B* **91**, 041115 (2015).
- [96] M. Zeyen, *Focused Raman Beam Addressing for a Trapped-Ion Quantum Processor (Master Thesis)*. PhD thesis, 2016.
- [97] G. J. Martyna, M. L. Klein, and M. Tuckerman, “Nose–Hoover chains: The canonical ensemble via continuous dynamics”, *The Journal of Chemical Physics* **97**, 2635-2643 (1992).
- [98] G. Casati, J. Ford, F. Vivaldi, and W. M. Visscher, “One-Dimensional Classical Many-Body System Having a Normal Thermal Conductivity”, *Phys. Rev. Lett.* **52**, 1861–1864 (1984).
- [99] B. Hu, B. Li, and H. Zhao, “Heat conduction in one-dimensional chains”, *Phys. Rev. E* **57**, 2992–2995 (1998).
- [100] S. Lepri, R. Livi, and A. Politi, “Heat Conduction in Chains of Nonlinear Oscillators”, *Phys. Rev. Lett.* **78**, 1896–1899 (1997).
- [101] S. Lepri, R. Livi, and A. Politi, “Thermal conduction in classical low-dimensional lattices”, *Physics Reports* **377**, 1 - 80 (2003).
- [102] P. A. Skordos and W. H. Zurek, “Maxwell’s demon, rectifiers, and the second law: Computer simulation of Smoluchowski’s trapdoor”, *American Journal of Physics* **60**, 876-882 (1992).
- [103] I. Bloch, “Ultracold quantum gases in optical lattices”, *Nature Physics* **1**, 23–30 (2005).
- [104] W. S. Bakr, J. I. Gillen, A. Peng, S. Fölling, and M. Greiner, “A quantum gas microscope for detecting single atoms in a Hubbard-regime optical lattice”, *Nature* **462**, 74–77 (2009).
- [105] C. Gollub, P. V. D. Hoff, M. Kowalewski, U. Troppmann, and R. D. Vivie-Riedle, *Vibrational Energy Transfer Through Molecular Chains: An Approach Toward Scalable Information Processing*, ch. 13, pp. 371–402. John Wiley & Sons, Inc., 2014.

- [106] N. Freitas, E. A. Martinez, and J. P. Paz, “*Heat transport through ion crystals*”, *Physica Scripta* **91**, 013007 (2015).
- [107] A. Ruiz, D. Alonso, M. B. Plenio, and A. del Campo, “*Tuning heat transport in trapped-ion chains across a structural phase transition*”, *Phys. Rev. B* **89**, 214305 (2014).
- [108] A. Ruiz-García, J. J. Fernández, and D. Alonso, “*Delocalization and heat transport in multidimensional trapped ion systems*”, *Phys. Rev. E* **99**, 062105 (2019).
- [109] T. Pruttivarasin, M. Ramm, I. Talukdar, A. Kreuter, and H. Häffner, “*Trapped ions in optical lattices for probing oscillator chain models*”, *New Journal of Physics* **13**, 075012 (2011).
- [110] M. Ramm, T. Pruttivarasin, and H. Häffner, “*Energy transport in trapped ion chains*”, *New Journal of Physics* **16**, 063062 (2014).
- [111] J. I. Cirac and P. Zoller, “*A scalable quantum computer with ions in an array of microtraps*”, *Nature* **404**, 579–581 (2000).
- [112] F. N. Krauth, J. Alonso, and J. P. Home, “*Optimal electrode geometries for 2-dimensional ion arrays with bi-layer ion traps*”, *Journal of Physics B: Atomic, Molecular and Optical Physics* **48**, 015001 (2014).
- [113] R. Schmied, J. H. Wesenberg, and D. Leibfried, “*Optimal Surface-Electrode Trap Lattices for Quantum Simulation with Trapped Ions*”, *Phys. Rev. Lett.* **102**, 233002 (2009).
- [114] A. Dhar, “*Heat transport in low-dimensional systems*”, *Advances in Physics* **57**, 457-537 (2008).
- [115] R. Toral and P. Colet, *Stochastic numerical methods: an introduction for students and scientists*. John Wiley & Sons, 2014.
- [116] C. Cohen-Tannoudji, “*Atomic motion in laser light*”, in *Fundamental systems in quantum optics*, J. Dalibard, J. M. Raimond, and J. Zinn-Justin, eds. Elsevier, 1992.
- [117] H. J. Metcalf and P. van der Straten, “*Laser cooling and trapping of atoms*”, *J. Opt. Soc. Am. B* **20**, 887–908 (2003).

- [118] L. Chee Kong, “*Study of Classical and Quantum Open Systems*”, [arXiv:1008.0491](https://arxiv.org/abs/1008.0491).
- [119] E. A. Novikov, “*Functionals and the random-force method in turbulence theory*”, Soviet Journal of Experimental and Theoretical Physics **20**, 1290-1294 (1965).
- [120] P.-W. Ma and S. L. Dudarev, “*Langevin spin dynamics*”, Phys. Rev. B **83**, 134418 (2011).
- [121] G. D. Chiara, G. Landi, A. Hewgill, B. Reid, A. Ferraro, A. J. Roncaglia, and M. Antezza, “*Reconciliation of quantum local master equations with thermodynamics*”, New Journal of Physics **20**, 113024 (2018).
- [122] A. Levy and R. Kosloff, “*The local approach to quantum transport may violate the second law of thermodynamics*”, EPL (Europhysics Letters) **107**, 20004 (2014).
- [123] S. Särkkä and A. Solin, *Applied Stochastic Differential Equations*. Institute of Mathematical Statistics Textbooks. Cambridge University Press, 2019.
- [124] Z. Rieder, J. L. Lebowitz, and E. Lieb, “*Properties of a Harmonic Crystal in a Stationary Nonequilibrium State*”, Journal of Mathematical Physics **8**, 1073-1078 (1967).
- [125] A. Casher and J. L. Lebowitz, “*Heat Flow in Regular and Disordered Harmonic Chains*”, Journal of Mathematical Physics **12**, 1701-1711 (1971).
- [126] D. F. V. James, “*Quantum dynamics of cold trapped ions with application to quantum computation*”, Applied Physics B **66**, 181–190 (1998).
- [127] J. Bezanson, S. Karpinski, V. B. Shah, and A. Edelman, “*Julia: A Fast Dynamic Language for Technical Computing*”, [arXiv:1209.5145](https://arxiv.org/abs/1209.5145).
- [128] J. Bezanson, A. Edelman, S. Karpinski, and V. Shah, “*Julia: A Fresh Approach to Numerical Computing*”, SIAM Review **59**, 65-98 (2017).
- [129] C. Rackauckas and Q. Nie, “*Adaptive methods for stochastic differential equations via natural embeddings and rejection sampling with memory*”, Discrete and Continuous Dynamical Systems Series B **22**, 2731-2761 (2017).

- [130] F. M. Leupold, *Bang-bang Control of a Trapped-Ion Oscillator*. PhD thesis, ETH Zurich, 2015.
- [131] H.-Y. Lo, *Creation of Squeezed Schrödinger's Cat States in a Mixed-Species Ion Trap*. PhD thesis, ETH Zurich, 2015.
- [132] T. Zhang and T. Luo, “Giant Thermal Rectification from Polyethylene Nanofiber Thermal Diodes”, *Small* **11**, 4657–4665 (2015).
- [133] M. Enderlein, T. Huber, C. Schneider, and T. Schaetz, “Single Ions Trapped in a One-Dimensional Optical Lattice”, *Phys. Rev. Lett.* **109**, 233004 (2012).
- [134] A. Bermudez, M. Bruderer, and M. B. Plenio, “Controlling and Measuring Quantum Transport of Heat in Trapped-Ion Crystals”, *Phys. Rev. Lett.* **111**, 040601 (2013).
- [135] C. Schneider, M. Enderlein, T. Huber, and T. Schaetz, “Optical trapping of an ion”, *Nature Photonics* **4**, 772–775 (2010).
- [136] A. Riera-Campeny, M. Mehboudi, M. Pons, and A. Sanpera, “Dynamically induced heat rectification in quantum systems”, *Phys. Rev. E* **99**, 032126 (2019).
- [137] H. Ma and Z. Tian, “Significantly High Thermal Rectification in an Asymmetric Polymer Molecule Driven by Diffusive versus Ballistic Transport”, *Nano Letters* **18**, 43–48 (2018).
- [138] K. M. Reid, H. D. Pandey, and D. M. Leitner, “Elastic and Inelastic Contributions to Thermal Transport between Chemical Groups and Thermal Rectification in Molecules”, *The Journal of Physical Chemistry C* **123**, 6256–6264 (2019).
- [139] D. Leibfried, R. Blatt, C. Monroe, and D. Wineland, “Quantum dynamics of single trapped ions”, *Rev. Mod. Phys.* **75**, 281–324 (2003).
- [140] S. Chu, L. Hollberg, J. E. Bjorkholm, A. Cable, and A. Ashkin, “Three-dimensional viscous confinement and cooling of atoms by resonance radiation pressure”, *Phys. Rev. Lett.* **55**, 48–51 (1985).
- [141] H. Metcalf and P. Van der Straten, *Laser Cooling and Trapping*. Graduate texts in contemporary physics. Springer-Verlag, New York, 1999.

- [142] S. Singer, K. F. Freed, and Y. B. Band, “*Invariant imbedding solution of driven (inhomogeneous) and homogeneous Schrödinger equations*”, [The Journal of Chemical Physics](#) **77**, 1942-1950 (1982).
- [143] Y. B. Band and I. Tuvi, “*Quantum rearrangement scattering calculations using the invariant imbedding method*”, [The Journal of Chemical Physics](#) **100**, 8869-8876 (1994).